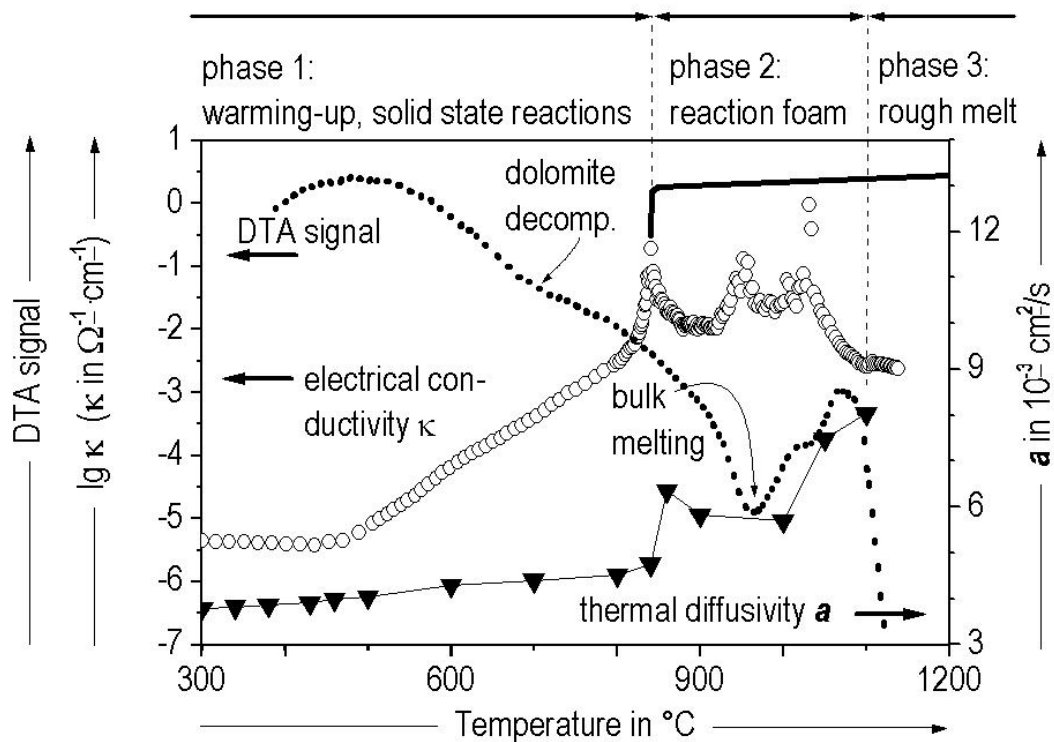


## Development of Methods for the Characterization of Melting Batches



# **Development of Methods for the Characterization of Melting Batches**

von der Fakultät für Georessourcen und Materialtechnik  
der Rheinisch-Westfälischen Technischen Hochschule Aachen

zur Erlangung des akademischen Grades eines

Doktors der Ingenieurwissenschaften

genehmigte Dissertation

vorgelegt von **M.Sc.**

**Nang Sam Kham**

aus Taunggyi, Shan State, Myanmar

**Berichter:** Univ.-Prof. Dr. rer. nat. Reinhard Conradt  
Univ.-Prof. Dr.-Ing. Joachim Deubener

Tag der mündlichen Prüfung: 12. Juli 2005

Diese Dissertation ist auf den Internetseiten der Hochschulbibliothek online verfügbar

# Acknowledgement

I would like to take this opportunity to thank everyone who took some of their precious time to help my dissertation become a reality. I am very grateful for their help, time, and patience.

Many heartfelt thanks to Prof. Conradt as my appreciated advisor, who guided me all along the way, from my Masters of Science in Thailand to this dissertation, the culmination of my scholastic career. He kept me focused, always willing to share his vast knowledge, and gently introduced me to the German culture. The long scholastic road to this point would have been much rougher without his advise, guidance, and presence.

I am also indebted and grateful to Prof. Deubener from TU Clausthal, Germany, who showed genuine interest in my work and took over the duty as 2<sup>nd</sup> reviewer of my thesis.

I would like to thank Herrn Lennartz for his ever-willingness to help with all the electrical problems, and to Herrn Wilsmann for so much technical support. Further thanks go to Mr. D. Gathen (computer support), J. Krzoska (thermal difussivity), T. Hoefler (heating microscope, DTA, TGA, and DSC), Dr. C. Schmalzried (XRD), J. Shin (drop calorimeter) and the *Werkstatt* team. I am grateful to all staff at GHI for their generosity and prompt support which made the tough researching process significantly easier.

My gratitude goes to Mrs. Marianne Conradt, the Bartholomé family, Ajarn Klein, Ulf Dahlmann, Marion Kalde, Josefine Lennartz, and Michaela Steffens for their love and encouragement. Special thanks to Esther, Sebastian, J. Voravit, Ai, Thai students (GATS), and friends I made in Aachen for their encouragement as well as support through these years in Germany.

To my dear husband and daughter: I can not really express in words, how much you have encouraged me over the years. Because of your constant support, this dream has become today a reality. I am eternally grateful, Pisit, for your gentle support of times, and Monie, thank you for being the light of my life and always giving me a smile whenever I needed it the most.

I would also like to acknowledge the Deutsche Forschungsgemeinschaft (DFG) for financial support within the DFG project "Stoff-und Wärmeumsatz in Rohstoffgemengen beim Glasschmelzprozess" (DFG no. CO 249/2-1, final report 2002)

Finally, I wish to express my gratitude to my parents Sai Kenneth Hsam and Nang Ngwe Pwint, my sisters and brother Nang Kham mo, Sai Naw Main, Nang Sam Hom, and nephew Sai Khun Muang for their encouragement through all these years.

## Abstract

Glass batch melting has been studied by many researchers on various scales and under various conditions but no comprehensive understanding has been reached. In view of this situation, a major part of this work was devoted to the improvement of five new experimental methods suitable for the investigation of batch melting. These are: conductometry, thermal diffusivity, heating microscopy, batch free time (BFT) and weight loss measurement. Firstly, as for the development of conductometry, three meaningful ways to present batch reactions in terms of "DTA", "voltage drop", and "electrical conductivity" were concluded. It was also possible to determine the duration of stages characterized by foaming. Secondly, for thermal diffusivity, an optimized output signals at a frequency of 50 Hz with time interval of 150 s was applied. It showed good measurement results. As a conclusion, the grain-to-grain contact in model calculations should be taken into account by a dimensionless shape factor of 2.5 to 3.5. Local conductometry combined with temperature measurement allowed to measure simultaneously the electrical conductivity and the local temperature in a melting batch. The measurement of the local thermal diffusivity was performed by an evaluation of the runtime of a periodically generated heat pulse. Thirdly, for the heating microscope, a new way to present the effect of gas release from glass batches prior to refining was developed. It was found that minor batch additions have a large influence. Fourthly, the BFT results show that the reaction behavior of container flint and green glass batches was more sluggish than that of crystal glass batches. By observation through a silica tube furnace, the beginning of batch reactions with cullets at the surface deep into the glass melt were observed. After 2 minutes foam was formed and decreased within 10 minutes. Finally, weight loss determination for samples up to 200 g was developed. It was found that the mass loss of soda ash detected in a vertical tube furnace started at a lower temperature and was completed at a higher temperature than suggested by the results measured by thermogravimetric analysis (TGA). These new characterization methods not only open concepts for the presentation and interpretation of batch reactions, but also close the experimental gap between conventional lab scale characterization and the behavior actually observed in industrial production.

## Kurzfassung

Das Schmelzen von Glasgemengen wurde von vielen Wissenschaftlern auf unterschiedlichen Größenskalen und bei verschiedenen Bedingungen untersucht, aber kein allgemeines Verständnis wurde erzielt. Aufgrund dieser Situation wurde ein Großteil dieser Arbeit der Weiterentwicklung von fünf neuen experimentellen Methoden gewidmet, die für die Untersuchung des Schmelzens von Glasgemengen geeignet sind. Diese sind Konduktometrie, Messungen der Temperaturleitfähigkeit, Beobachtungen im Erhitzungsmikroskopie, Bestimmung der mit "Rauhmelzzeit" übersetzten *batch free time* (BFT) und des Massenverlustes. Zuerst wurden sinnvolle Wege abgeleitet, um Gemengereaktionen durch differentielle *in situ* thermische Analyse (DTA), Spannungsabfall und elektrische Leitfähigkeit darzustellen. Dabei war es ebenfalls möglich, die Dauer der durch Schaumbildung gekennzeichneten Stadien zu bestimmen. Zweitens wurde für die Bestimmung der thermischen Leitfähigkeit ein optimiertes Signal mit einer Frequenz von 50Hz in Zeitabständen von 150 s angelegt. Diese Methode ergab gute Messergebnisse. Es zeigte sich, dass der Korn-zu-Korn Kontakt bei Modellrechnungen durch einen dimensionslosen Formfaktor von 2,5 bis 3,5 für Glasgemenge berücksichtigt werden sollte. Lokale Konduktometrie kombiniert mit Temperaturmessungen erlaubten es, gleichzeitig die elektrische Leitfähigkeit und die lokale Temperatur in einer Gemengesmelze zu bestimmen. Drittens wurde für das Erhitzungsmikroskop eine neue Möglichkeit entwickelt, den Effekt der Gasfreisetzung aus einem Glasgemenge vor der Läuterung darzustellen. Dabei wurde gezeigt, daß die Zugabe von Nebenbestandteilen des Gemenges einen wesentlichen Einfluss hat. Viertens zeigen die Ergebnisse für die BFT-Untersuchungen, daß das Reaktionsverhalten von weißem und grünem Glas träger ist als das von Kristallglas. Durch Beobachtung durch eine Kieselküvette wurde der Beginn der Gemengereaktion mit Scherben an der Oberfläche bis tief in die Glassmelze beobachtet. Nach zwei Minuten wurde Schaum gebildet, der nach 10 Minuten abnahm. Schließlich wurde eine Massenverlustbestimmung für Proben bis zu 200 g entwickelt. Es wurde gefunden, daß der Massenverlust von Soda in einem vertikalen Rohrofen bei kleinerer Temperatur beginnt und bei einer höheren Temperatur endet, als durch TGA gemessen. Die neuen Charakterisierungsmethoden eröffnen nicht nur neue Wege, den Vorgang der Gemengesmelze darzustellen und zu interpretieren, sondern schließen auch eine experimentelle Lücke zwischen konventionellen Charakterisierungsmethoden und dem in der industriellen Produktion beobachteten Verhalten.

# Contents

	Page
<b>1. Introduction .....</b>	<b>1</b>
1.1. Motivation, objective, and scope .....	1
1.2. Literature survey.....	2
<b>2. Theory .....</b>	<b>5</b>
2.1. Process engineering of glass melting .....	5
2.1.1. Quality control cycles.....	5
2.1.2. Mass flow characteristics.....	7
2.1.3. Heat balance and heat flow .....	9
2.2. Thermo-chemistry of primary melt formation .....	12
2.2.1. Direct melting (physical melting).....	13
2.2.2. Sulfate reduction.....	15
2.2.3. Reactive carbonate melting .....	15
2.2.4. Reactive silicate melting .....	17
2.2.5. Thermochemical data .....	26
2.3. Macro-kinetics of batch melting .....	31
2.4. Micro-kinetics and electrical conductivity.....	33
2.4.1. Primary melt formation and electrical conductivity.....	34
2.4.2. Further generation of liquid phases .....	36
2.4.3. Effect of minor additions .....	38
<b>3. Experiments .....</b>	<b>41</b>
3.1. Preparation of materials; investigated systems .....	41
3.1.1. Characterization of raw materials .....	41
3.1.2. Preparation of grain size fractions .....	42
3.1.3. Glass batch compositions.....	42
3.1.4. Investigated systems .....	42
3.1.5. Preparation of melting crucibles .....	45
3.2. Methods of investigation.....	46
3.2.1. Conductometry .....	47
3.2.2. Thermal diffusivity.....	51
3.2.3. Heating microscopy .....	53
3.2.4. Batch free time (BFT) experiments.....	55
3.2.5. Mass loss measurements (50 g scale) .....	59
<b>4. Results and discussion .....</b>	<b>61</b>
4.1. Conductometry .....	61
4.1.1. Accuracy of the measurement.....	61
4.1.2. Detection of foam formation period.....	64

4.1.3. Evaluation and presentation of results.....	64
4.1.4. One-component test.....	66
4.1.5. Tests on binary mixtures .....	66
4.1.6. Tests on ternary mixtures .....	75
4.1.7. Test on multi-component mixtures.....	78
4.2. Thermal diffusivity .....	85
4.2.1. Calculation of the thermal diffusivity .....	85
4.2.2. Evaluation immediate results.....	86
4.2.3. Accuracy of the measurement.....	88
4.2.4. Example of the measurement.....	88
4.3. Heating microscopy.....	90
4.3.1. Conventional use.....	90
4.3.2. Extended use of heating microscope tests.....	93
4.4. Batch free time (BFT) experiments.....	99
4.4.1. Tests at GHI .....	99
4.4.2. Tests at SCHOTT Co. ....	104
4.5. Mass loss measurements (50 g scale).....	106
4.5.1. System calibration.....	106
4.5.2. Measurement of 50 g glass batches.....	109
<b>5. Conclusions .....</b>	<b>111</b>
5.1. Conductometry .....	112
5.2. Thermal diffusivity .....	116
5.3. Heating microscope.....	117
5.4. Batch free time (BFT) .....	119
5.5. Mass loss .....	120
5.6. Summary .....	121
<b>6. References .....</b>	<b>122</b>

## Lists of symbols and abbreviations

### Greek symbols

$\eta$	= viscosity [dPa·s]
$\sigma$	= surface tension [N/m]
$\lambda^*$	= heat conductivity [J/(s·m·K)]
$\rho$	= bulk density [g/m <sup>3</sup> ]
$\rho'$	= electrical resistivity [ $\Omega$ ·cm]
$\lambda$	= wavelength [nm]
$\kappa$	= electrical conductivity [ $\Omega$ ·cm] <sup>-1</sup>

### Latin symbols

$A$	= contact area between batch heap and glass melt [m <sup>2</sup> ]
$a$	= thermal diffusivity [cm <sup>2</sup> /s]
$batch_{middle}$	= height of the batch at the middle of the crucible [cm]
$c_p$	= specific heat capacity [J/(g·K)]
$C_{cell}$	= cell constant of the conductometry sensor
$d$	= distance [cm]
$D$	= diffusion coefficient [cm <sup>2</sup> /s]
$H_r$	= specific enthalpy of reaction [kJ/kg]
$H_{ex}$	= exploited heat [kWh/t], chemical heat demand of the batch-to-batch conversion at 298 K
$H_{in}, H_{chem}$	= specific heat demand of glass melting [kWh/t]
$H_{sf}$	= heat set free in the furnace [kWh/t]
$H_{fire}$	= heat transferred from the “fire” to furnace body [kWh/t]
$H_{wall}$	= heat loss through the furnace periphery [kWh/t]
$H_{off}$	= heat contained in offgas entering the heat exchange body [kWh/t]
$H_{wx}$	= heat lost through the heat exchanger periphery [kWh/t]



$H_{re}$	= heat recovered by the heat exchanger [kWh/t]
$H_{phys}$	= physical heat stored in the glass melt [kWh/t]
$H_{gas}$	= heat content of the release \batch gases [kWh/t]
$H_R$	= heat of reaction [kJ/mol SiO <sub>2</sub> ]
$J_Q$	= heat flow into the batch heap [kJ/(m <sup>2</sup> ·s)]
$L$	= immersion depth [cm]
$m$	= mass of the batch heap [kg]
$\Delta m$	= mass loss [g]
$q_{ht}$	= input heat flow [kW/m <sup>2</sup> ]
$q_{ex}$	= exploited heat flow [kW/m <sup>2</sup> ]
$R$	= electrical resistance [ $\Omega$ ]
$r^*$	= distance between sensor and thermocouple [cm]
$r$	= pull rate of glass melt [t/(cm <sup>2</sup> ·h)]
$s$	= height of the batch heap [m]
$T_{eq}$	= equilibrium temperature [°C]
$T_0$	= room temperature [K]
$T_R$	= reaction temperature [K]
$t$	= time [s]
$T$	= temperature [K, °C]
$T_1$	= temperature level: start of visible gas release [°C]
$T_2$	= temperature level: round edge point [°C]
$T_3$	= temperature level: half sphere point [°C]
$t_1$	= time (related to BFT) of start of reaction [s]
$t_2$	= time (related to BFT) of still visible solid islands [s]
$t_3$	= time (related to BFT) when the solid islands disappear [s]
$U$	= voltage [V]

### Abbreviations

AC	= alternating current
BFT	= batch free time
DTA	= differential thermal analysis
DTG	= differential thermogravimetry

DSC	= differential scanning calorimetry
DC	= direct current
GHI	= Institute for Mineral Engineering ( <u>G</u> esteins <u>h</u> üttenkunde- <u>I</u> nstitut)
PID	= proportional integral and differential controller characteristics
QW	= Quarzwerke Frechen
TGA	= thermal gravimetry analysis

## List of Figures

	Page
Figure 1	Quality control cycles for a mass glass production line..... 7
Figure 2	Process steps during glass melting in a tank furnace ..... 8
Figure 3	Volume flow pattern in a container glass tank furnace..... 9
Figure 4	Simplified heat balance of a glass melting aggregate..... 10
Figure 5	Balance of heat flows $q$ in a glass tank furnace ..... 12
Figure 6	Specific energy demand plotted versus the pull rate ..... 12
Figure 7	Liquidus curves of the binary systems of $\text{Na}_2\text{CO}_3$ with $\text{Na}_2\text{S}$ , $\text{Na}_2\text{SO}_4$ , $\text{CaCO}_3$ , $\text{NaNO}_3$ , or $\text{NaCl}$ ..... 14
Figure 8	Liquidus curve and melt viscosities in the binary system $\text{Na}_2\text{O-SiO}_2$ ..... 19
Figure 9	Liquidus curve and location of compounds in the binary system $\text{Na}_2\text{O-SiO}_2$ , sodia-rich part..... 19
Figure 10	Ternary system $\text{Na}_2\text{O-CaO-SiO}_2$ , technologically relevant range ..... 21
Figure 11	Ternary system $\text{Na}_2\text{O-CaO-SiO}_2$ , boundary of the crystallization field of sodium disilicate ..... 22
Figure 12	a. Ternary phase diagram $\text{Na}_2\text{O-CaO-SiO}_2$ , rectangular projection ..... 23 b. Ternary phase diagram $\text{Na}_2\text{O-Al}_2\text{O}_3\text{-SiO}_2$ , triangular projection..... 24
Figure 13	Ternary system $\text{Na}_2\text{O-MgO-SiO}_2$ ..... 25
Figure 14	Ternary system $\text{Na}_2\text{O-MgO-SiO}_2$ , boundary of the crystallization field of sodium disilicate ..... 26
Figure 15	Diffusion-temperature plot for $\text{KCl}$ ..... 35
Figure 16	Ternary phase diagram of $\text{Na}_2\text{O-CaO-SiO}_2$ ..... 36
Figure 17	Electrical conductivities $\log \kappa$ and thermal diffusivities..... 37
Figure 18	$\text{NaCl-Na}_2\text{CO}_3$ phase diagram ..... 39
Figure 19	Rate of mass change against temperature for quartz-sodium carbonate mixture ..... 40
Figure 20	Sketch of crucibles..... 45
Figure 21	Sketch of the small study furnace ..... 47
Figure 22	Sketch of the temperature-resistivity sensor (a) and of the electrical circuit (b) used to measure the voltage drop across the batch..... 49
Figure 23	Sketch of the double cylinder sensor (made of Pt) ..... 49
Figure 24	Modified electrical circuit with $U_0 = 3\text{V AC}$ , $R_1 = 1\text{ M}\Omega$ , $R_{2a} = 10\text{ k}\Omega$ , $R_{2b} = 100 - 1000\ \Omega$ ..... 50

Figure 25	Sketch of the sensor for thermal diffusivity measurement.....	52
Figure 26	Thermal diffusivity sensor, modified version .....	53
Figure 27	Sketch of the heating microscope .....	54
Figure 28	Three characteristic temperatures $T_1$ : start of visible gas release; $T_2$ : round edge point; $T_3$ : half sphere point .....	54
Figure 29	Design of the batch free time experiment at GHI a), and at SCHOTT Co. b) .....	56
Figure 30	Design of the gas mass loss determination furnace .....	59
Figure 31	Sketch of macro thermo balance furnace designed and tested at GHI.....	60
Figure 32	Crystal water peaks of soda ash tested at Chulalongkorn and GHI.....	62
Figure 33	Melting peak of soda ash at $855 \pm 5$ °C .....	63
Figure 34	Plot of DTA signal vs. temperature showing quartz inversion at 573 °C from silica sand.....	63
Figure 35	Plot of soda-sand reaction showing first melt formation.....	64
Figure 36	Illustration of the voltage drop $U_x$ as a function of T.....	65
Figure 37	Illustration of three characteristic signals .....	66
Figure 38	Plot of electrical conductivity and temperature of silica sand, limestone, dolomite, and phonolite .....	67
Figure 39	Plot of DTA and electrical conductivity signals with temperature of soda-sand .....	68
Figure 40	Variation of soda contents in the mixture of soda-sand .....	69
Figure 41	Illustration of soda-sand mixtures; grain size fractions of sand varied.....	71
Figure 42	DTA plots of mixtures soda-sand; grain size fractions of sand varied.....	72
Figure 43	Plot of DTA and electrical conductivity signals of mixed soda-limestone....	73
Figure 44	Plot of DTA and electrical conductivity of mixed soda-dolomite .....	74
Figure 45	Plot of DTA and electrical conductivity of mixed soda-phonolite.....	75
Figure 46	Illustration of a) electrical conductivity plot with temperature, and b) plot of DTA signals with temperature .....	76
Figure 47	Investigation of soda-lime-sand system showing DTA signals and electrical conductivity .....	77
Figure 48	Investigation of multi-component systems showing electrical conductivity and DTA signals.....	78
Figure 49	Investigation of multi-component batches showing the electrical conductivity signal for container flint, container green, and amber glass batches.....	79

Figure 50	Influence of atmospheres on melting reactions of glass 74-10-16 .....	80
Figure 51 a	Voltage drop across a lead glass batch during heating at 10 K/min .....	83
Figure 51 b	Electrical conductivity $\kappa$ in a lead glass batch heated up at 10 K/min, presented as a function of time .....	84
Figure 51 c	Electrical conductivity $\kappa$ in a lead glass batch heated up at 10 K/min, presented as a function of temperature .....	84
Figure 52	Superimposition of heat pulses registered at a distance $r$ from the heating source .....	86
Figure 53	Plot of temperature difference between sensor and batch vs. overall batch temperature .....	87
Figure 54	Plot of time vs. temperature difference between sensor and batch .....	87
Figure 55	Illustration of the tests from silica sand indicating quartz inversion .....	88
Figure 56	Plot of thermal conductivity with batch temperature of different grain sizes of sand .....	89
Figure 57	Illustration of (T1) start of visible bubbling, (T2) softening point, and (T3) half sphere point .....	91
Figure 58	Investigation of soda lime silicate glass with 1 wt. % additives showing the effect on melting behavior .....	92
Figure 59	Investigation of soda lime silicate glass with 1 wt. % additives showing the progress of gas release .....	93
Figure 60	Residual sand grains and remaining bubbles in the melt .....	94
Figure 61	Investigation by heating microscope under a flow of CO <sub>2</sub> (10 l/h) of a) soda-sand, b) soda-lime, c) soda-dolomite, d) soda-phonolite, e) soda-amber cullet, f) soda-container green cullet, and g) soda-container flint cullet .....	96
Figure 62	Investigation of the results from figure 61, plot of T1 and of the “complete melting” temperature .....	97
Figure 63	Phase diagram of Na <sub>2</sub> O-Na <sub>2</sub> CO <sub>3</sub> .....	98
Figure 64	Investigation of soda ash and phonolite in a flow of gases at 10 l/h .....	98
Figure 65	Progress of glass batch melting observed in a batch free time observation furnace at GHI at times t1, t2, and t3 .....	100
Figure 66	Residual crystalline phases in glass S4 after a) 10 min, b) 20 min, c) 50 min, and d) 80 min .....	101
Figure 67	Photographs of all batches melted at 1400 °C for 30 min, a) top view and b) vertical sections .....	102
Figure 68	Illustration of region with high crystalline phase content .....	103
Figure 69	Sequence of a soda lime silicate glass batch charged on top of a cullet melt at 1550 °C .....	105

---

Figure 70	Mass loss calibration by limestone and dolomite showing a perfect match with theoretical mass loss .....	107
Figure 71	Mass loss of limestone, a comparison between TGA and the vertical tube furnace 200 g balance .....	108
Figure 72	Mass loss of dolomite, a comparison between TGA and the vertical tube furnace 200 g balance .....	108
Figure 73	Mass loss of soda sand batch (S3) measured from 50 g batch compared to mass loss detected from TGA .....	109
Figure 74	Mass loss of container flint batch (S2, sample size 50 g) compared to mass loss detected from TGA .....	110
Figure 75	Plot of electrical conductivity and thermal diffusivity of white glass.....	115

## List of Tables

	Page
Table 1	Viscosities and surface tensions of selected melts..... 14
Table 2	Heat of reaction $H_R$ of silicate formation ..... 18
Table 3	Enthalpies and Gibbs free energies of selected carbonate and silicate compounds ..... 28
Table 4	Chemical analysis of raw materials used in the study ..... 41
Table 5	Particle size fractions of sand..... 42
Table 6	Composition of batches in g/100 g glass ..... 43
Table 7	Overview over the small-scale tests on thermal diffusivity..... 43
Table 8	Overview over the small-scale tests on electrical conductivity ..... 44
Table 9	Composition of clay crucibles ..... 45
Table 10	Composition of the batches used for studying BFT ..... 58
Table 11	Nominal oxide composition of glasses S1 to S5 after table 10 in wt. %..... 58
Table 12	Conductivity standard solutions, KCl in D.I. water ..... 82
Table 13	Resistivity measurement with pure crystal glass cullet melt, double cylinder sensor under isothermal conditions ..... 82
Table 14	Thermal conductivity $\alpha$ of sand at different grain sizes ..... 89
Table 15	Thermal conductivity $\alpha$ of different glass types ..... 90
Table 16	Bubble quantities and sizes determined by light microscope ..... 95
Table 17	Height of remaining rough melt layers ( $h_{\text{left}}$ , $h_{\text{middle}}$ , and $h_{\text{right}}$ ) and remaining batch layers above cullet melt ( $\text{batch}_{\text{middle}}$ ) in cm ..... 104

# Chapter 1

## Introduction

### 1.1 Motivation, objective, and scope

Glass batch melting has been studied by many researchers on various scales, and under various conditions, in an attempt to understand, optimize and control the melting process. The interest in a deeper understanding of the batch melting process is high. Although many details of this process have been investigated, no comprehensive understanding has been reached, and predictive modeling is still based on unproven assumptions. Since batch melting is the first step of the glass melting process, it controls the overall rate of the melting process. So, the knowledge of the batch melting process is very important in order to optimize, and enhance the pull rate in glass production. Earlier work was mainly focused on the thermochemistry and kinetics of the chemical reactions involved in batch melting. In mixtures containing soda ash, limestone, dolomite and sand as major components, the reaction progress was measured on small samples in terms of CO<sub>2</sub> liberation and electrical conductivity. The occurrence of primary melt was found to be the key event significantly accelerating the entire process. One of the variables which has been found to have a large effect on batch melting is the particle size of the batch components. Batch melting has been studied extensively on a small scale by DTA, XRD, etc. The main purpose of DTA measurement is to identify reactions taking place in a batch or sub-system of a batch, e.g., under variation of the heating rate. Until then, an investigation of thermal behavior of



batch blankets was still limited to this well-known differential thermal analysis method, which cannot handle samples over 5 g. This is very important if related to the industrial scale, because, the reactions taking place on a large scale are controlled by boundary conditions significantly different from the microscopic scale. For example: Heat conductivity within the sample has always a big influence in DTA experiments, while the impact of heat conductivity is still unclear on the large scale. The problem is that none of the methods involved in small scale experimentation can be transferred to experiments on a large scale (>10 kg). Transferable methods are needed by which batch melting can be monitored on a large scale in a reliable way. The methods to be used in this thesis are 1) the determination of local electrical conductivity, 2) direct measurement of the local thermal diffusivity, 3) the so-called batch free time (BFT, when the batch disappears under the melt level by more than 99 % wt.), 4) heating microscope, 5) and mass loss from large samples up to 200 g.

It is the objective of this thesis to apply those newly established methods to batches typical of industrial mass glasses, and to one- two- and three-component sub-systems of such batches, in order to identify and quantify the key steps of batch melting. In doing this, the effects of heating rate, particle size, cullet addition and melt accelerants will be investigated. The methods will be supplemented by conventional DTA, TGA, and DSC.

## 1.2 Literature survey

Batch melting has been a target of research for many decades. The first stage of the melting process for soda-lime-silicate glasses is a series of solid-state reactions which includes a release of gases. These reactions are followed by formation of the first liquid phase in the batch. It is at this time that reaction rate significantly speed up. Batch melting is terminated when a so-called rough melt has formed. This is basically an established melt still containing residual quartz grains. Differential thermal analysis (DTA) and thermogravimetric analysis (TGA) have been the primary analytical methods

for determining the reactions between the components during the early stage [1]. Much of the research has been done on various binary mixtures.

Wilburn and Thomassan [2], observed that varying the silica particle size distribution in soda ash-silica batch resulted in a shift to higher temperatures with the finer particle size, regarding both the temperature of mass loss and CO<sub>2</sub> release. Their DTA work indicated that the intensity of the endothermic and exothermic peaks varied with particle size in the soda ash-silica system. The intensity of other peaks decreased as the particle size distribution of the silica was decreased.

Kroeger and coworkers alone published an extended series of papers [3; 4, pt. II to VIII; 5] on the different influences governing the reaction rates in mixtures containing soda ash, limestone, and quartz as major components. The reaction progress was measured on small samples in terms of CO<sub>2</sub> liberation and electrical conductivity. The occurrence of primary melt was found to be the key event significantly accelerating the entire process. Speyer et al. [6-8] performed thermal analysis of reactions, including the effects of particle size, on the fusion of soda-lime-silicate glass batches containing melting accelerants. They used DTA, DTGA, and XRD interactively. Their work indicated that the NaCl was found to be among the most effective melting accelerants due to the formation of a NaCl-Na<sub>2</sub>CO<sub>3</sub> eutectic liquid phase at approx. 636 °C, which effectively attacked the silica and lime relics. CO<sub>2</sub> gas release terminated 80 K earlier with 1 wt. % NaCl additions, when compared to the base glass batch. Many results related to batch melting are also found in Speyer's book on thermal analysis [9]. Other methods used for studying the glass batch melting process include hot stage microscope and X-ray diffraction. The hot-stage microscope was used to observe physical changes which occur in a glass melt as the temperature was increased. Heating microscopic studies [10-11] revealed interesting details on the events among individual grains. Riedel [12] observed the interesting detail that soda preferentially attacks the quartz grains in low heating rate tests, while it preferentially attacks the limestone in high heating rate test. Conroy et al. [13] and Manring et al. [14] indicated that the melting process was a three-stage process when studied under a microscope. The first stage of the melting process includes the solid-state reaction which occur at less than 840 °C. The

second stage is the formation of the first liquid phase around the residual grains. The final stage is the dissolution of the silica grains into the melt. A series of five earlier papers [15, pt I to IV] were focused on the phase transformations which occur in binary and ternary systems containing silica in the temperature range of 900 to 1400 °C; the method applied was X-ray diffraction. A number of recent studies pick up the aspect of phase formation during batch melting [16]. Further studies are found in [17-18].

Most of the existing models on the chemistry of batch melting focus on heat transfer and flow in glass tanks. A model formulated by Hrma [19] simplifies the melting process such that for a given composition, a single temperature is the only variable. The result of this model is the prediction of time to batch free liquid. Work by Conradt et al. [20] focuses on the local temperature distribution and primary melt formation in a melting batch heap. The occurrence of primary melt was identified by a sudden increase of electrical conductivity.

All of the above studies focus on the thermochemistry and chemical kinetics, and some of them on micro-kinetics (grain size effects etc.) of batch melting. None of the above studies except [20] comprise the reality of a finitely extended batch heap. A pragmatic approach to this reality is found, e.g., in [21-32]. The authors visually determined the so-called floating batch-free time, i.e., the time required for a batch charged onto a cullet melt to disappear to 98 % beneath a molten surface. In these experiments, the mass of batch charged per surface area was a key parameter. A model designed to predict the batch-free time had been developed before [33]. An alternative approach to realistic dimensions is found in papers dealing with mathematical and physical modeling of melting batch heaps, e.g., [34-38]. The recent investigations present large amounts of empirical observations. They also reveal the fact that even the knowledge on fundamental phase diagrams is very limited. For example, no phase diagrams of dolomite-soda ash, and only an incomplete version of  $\text{Na}_2\text{O-MgO-SiO}_2$  are available [39].

## Chapter 2.

### Theory

Glass batch melting has to be studied and understood on at least four levels, or scales. These are:

- the atomic scale which is the scale of the chemical reactions, their thermodynamics and molecular kinetics, and of the structure (hence, the identity) of solid phases involved,
- the scale of micro-kinetics which is the scale of small particles, involving particles-to-particle contact, grain size, and packing effects,
- the scale of macro-kinetics which is the scale of macroscopic distribution of properties in the batch heap; the field of local temperature or CO<sub>2</sub> partial pressure, or the local occurrence of primary melt are typical examples, and
- the scale of the industrial process. This scale comprises the overall balance of heat and mass flows.

## 2.1 Process engineering of glass melting

### 2.1.1 Quality control cycles

The conventional industrial glass melting process is a continuous process running 24 h per day. It starts from a set of raw materials and leads to a mass product. The output may be a continuous product (like in flat or fiber glass production) or a sequence of single items (like in bottle or tableware production). The glass melting process is a sequential process comprising the following steps:

- batch preparation
- melting
- forming
- value adding/ decoration.

The ultimate target of the process is the efficient production of a product with acceptable quality, where the term “efficient” refers to the use of financial, raw material, energy, human, and environmental resources. Figure 1 illustrates some typical features of the process in terms of quality control cycles. It is essential to realize that a direct influence on the properties of the produced material, i.e., active quality control, can be exerted at the interface between raw materials acquisition and batch input only. Therefore, it is most important to employ a powerful service for raw materials analysis, batch calculation, adjustment, optimization etc. at this every point of the process. After this, the options to influence the quality of the material, or to correct mistakes, are restricted to a few indirect measures. Whatever goes wrong at the critical interface, will have to travel down the entire production line. Only at the end of the line, at the interface between forming and value adding / decorating there is another option to exert an effective, however this time passive, quality control (by the decision to accept or reject the product). The typical throughput time for a volume element of batch is 1 to 2 days, depending on the overall size of the production unit.

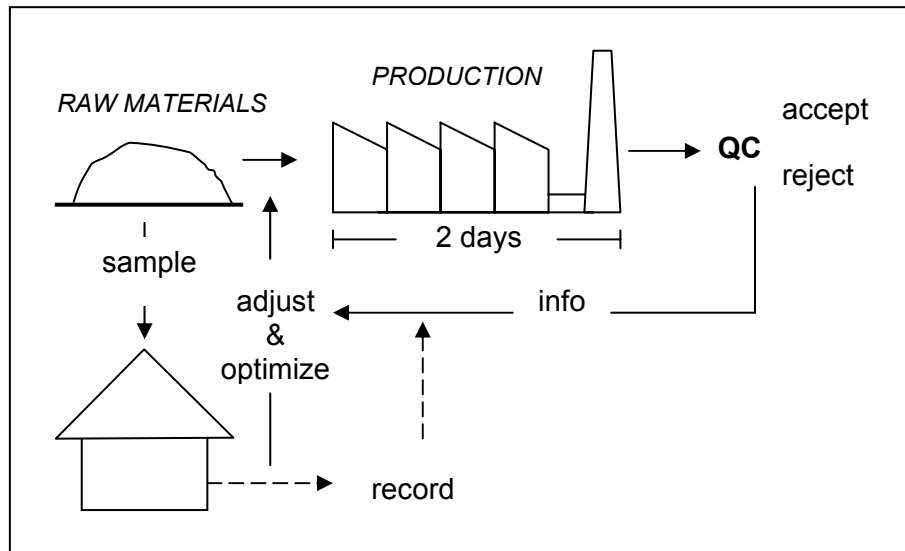


Fig. 1. Quality control cycles for a mass glass production line

### 2.1.2 Mass flow characteristics

The conventional glass melting unit is a glass tank furnace. From the point of view of chemical engineering, this is a continuously operated batch reactor with overall mass flow characteristics combining both plug flow and perfect mixer behavior. The heat demand of glass melting  $H_{ex}$  is constituted by a chemical term (due to the mostly endothermic melting reactions) and by the physical heat stored in the glass melt at pull temperature as

$$H_{ex} = (1-y_c) \cdot H_{chem} + \Delta H_T(\text{glass}), \quad (2.1)$$

where  $H_{ex}$  is the exploited heat,  $y_c$  is the fraction of cullet in t/t produced glass,  $H_{chem}$  is the specific heat demand of chemical glass batch reactions, and  $\Delta H_T(\text{glass})$  is the physical heat stored in the glass melt at pull temperature. The flow chart in figure 2 shows the different steps of glass melting in term of heat and mass balance determined from soda lime mass glasses by Conradt [40].

The heat content of 392 kWh with respect to room temperature is lost in the consecutive steps of manufacturing.

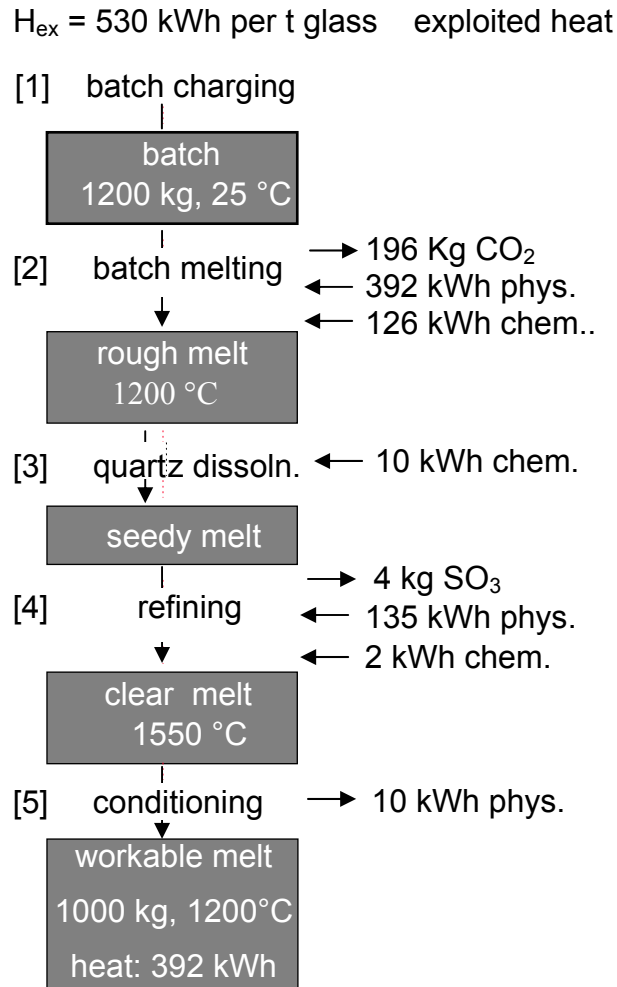


Fig. 2. Process steps during glass melting in a tank furnace; heat and mass balance are given for each step; the theoretical heat demand is 530 kWh per t of glass: phys.= physical, chem.= chemical [40]

As indicated already by the overall mass flow characteristics, these steps are not passed in a strictly sequential way. Rather a volume element may travel back and forth several times between the individual process steps. Figure 3 illustrates the typical volume flow pattern in a glass tank for a well-guided melting process. The first step is batch melting. It has a distinct plug flow characteristics (a “first in-first out” characteristics for each volume element involved), while the consecutive steps of quartz dissolution and refining take place in regimes with a pronounced mixer characteristics. Both regimes are kept essentially separate by the action of two vortices with opposite sense of rotation and a very strong upward flow in the center part of the tank. Formation and stability of the vortices is mainly due to thermal convection within the glass bath. Local velocities in the central upward flow

reach 10 mm/s. For comparison: the overall throughput velocity reaches 0.1 to 0.15 mm/s. The flow in the surface zone of the glass bath is oppositely directed to the main motion of the floating batch material. It thus restricts batch melting to the zone above the first vortex.

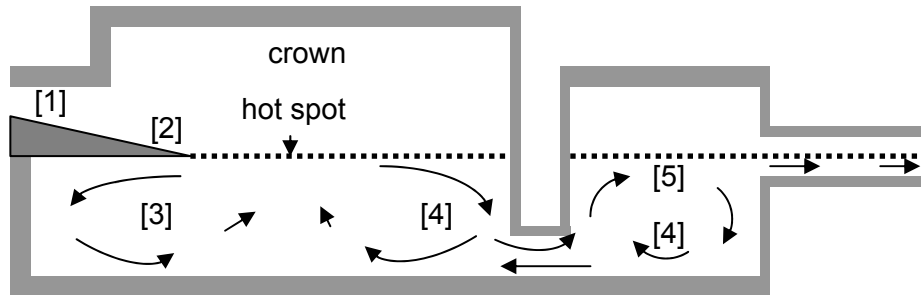


Fig. 3. Volume flow pattern in a container glass tank furnace; numbers refer to the process steps 1 to 5 in figure 2

### 2.1.3 Heat balance and heat flow [41-42]

With respect to heat transfer, the glass tank furnace is an open hearth furnace. The major portion of heat is generated by combustion of fossil fuel in the volume above the melt (combustion space). The predominant heat transfer mechanism is radiation from the flame and the refractory wall of the upper structure into the melt. The amount of heat not taken up by the refractory of the upper structure leaves the furnace as hot offgas and is partially recycled into the process by standard technologies (regeneration or recuperation). Figure 4 shows an energy flow chart for such a process.  $H_{in}$  is the specific heat demand of glass melting (kWh/t). This is the amount which has to be paid for.  $H_{ex}$  is the so-called exploited heat, i.e., the theoretical heat demand of glass melting. The meaning of the other quantities is explained in the figure legend. For a given batch,  $H_{ex}$  can be calculated with good accuracy [43-44]. For a soda-lime mass glass,  $H_{ex} \approx 500$  kWh/t. A new, well operated furnace reaches  $H_{in} \approx 1200$  kWh/t, which is equivalent to an overall efficiency of heat exploitation of  $H_{ex}/H_{in} \approx 42\%$ . The most effective furnaces which nowadays used are medium size U flame furnaces. With the use of recycled cullet, specific heats of well below 900 kWh/t are reached, equivalent to an efficiency of 55%. A comparison with the flow chart in figure 2



shows that the major part of  $H_{ex}$  is transferred to the cold raw materials during the batch melting step. This fact underlines the out-standing role of this step for the entire process.

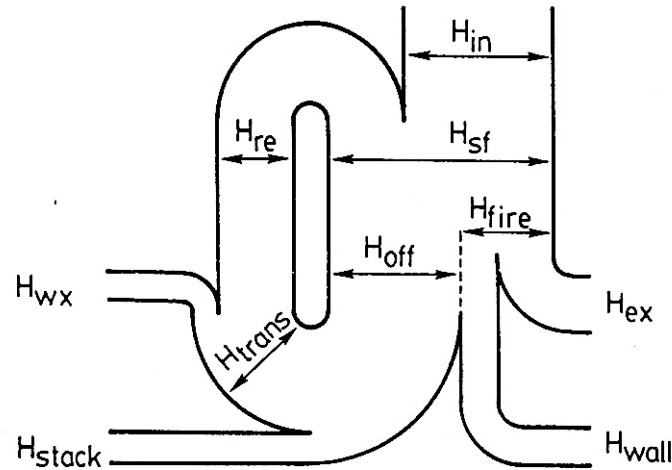


Fig. 4. Simplified heat balance of a glass melting aggregate [40];

- $H_{in}$ : heat input by fuel and electricity;
- $H_{sf}$ : heat set free in the furnace;
- $H_{fire}$ : heat transferred from the “fire” (fuel and electricity) to the furnace body (refractory and melt);
- $H_{ex}$ : exploited heat, i.e., heat of glass melting;
- $H_{wall}$ : heat lost through the furnace periphery;
- $H_{off}$ : heat contained in the offgas entering the heat exchanger body;
- $H_{wx}$ : heat lost through the heat exchanger periphery;
- $H_{re}$ : heat recovered by the heat exchanger

A simple heat flow model is shown in figure 5. It illustrates the competition between the heat flow  $q_{ht}$  (kW/m<sup>2</sup>) of internal heat transfer and the heat flow  $q_{ex}$  imposed externally by the pull of glass melt  $r$  from the furnace;  $r$  in t/(m<sup>2</sup>·h); all quantities are referred to 1 t of produced glass and 1 m<sup>2</sup> of hearth area. Heat and heat flow balance are linked by the simple relation

$$q_{ex} \approx H_{ex} \cdot r + \text{const.} \quad (2.2)$$

Hence the amount of pulled glass must be balanced very carefully against the internal heat flow. A well-guided process is operated at  $q_{ht} \approx q_{ex}$  (which is only possible for furnaces exceeding a certain minimum size). Under this condition, the specific heat demand  $H_{in}$  assumes a minimum (see figure 6). For  $q_{ex} \ll q_{ht}$ , the specific heat demand dramatically increases with  $r^{-1}$  while glass quality remains good. For  $q_{ex} > q_{ht}$ , the heat demand slightly increases with  $r^{1/4}$  while glass quality decreases. Heat transfer is most effective across a clear melt surface and least effective across areas still covered with unmolten batch. So, a high batch melting rate accelerates the entire process by increasing  $q_{ht}$ .

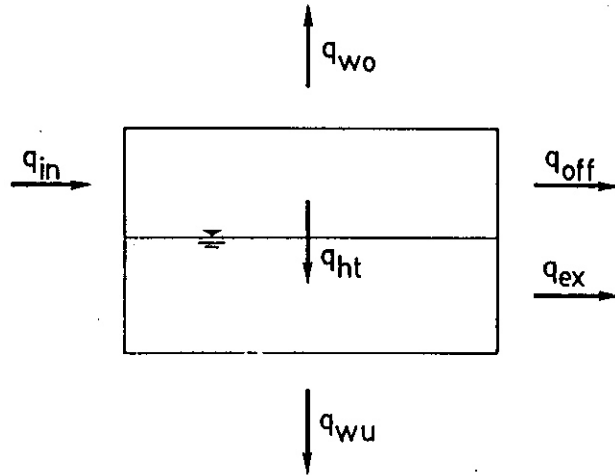


Fig. 5. Balance of heat flows  $q$  in a glass tank furnace [40]; in : input; wo: wall loss through the upper structure; wu: wall loss through the basin walls; off: offgas loss; ht: heat transfer into the glass bath; ex: heat loss due to the glass pull

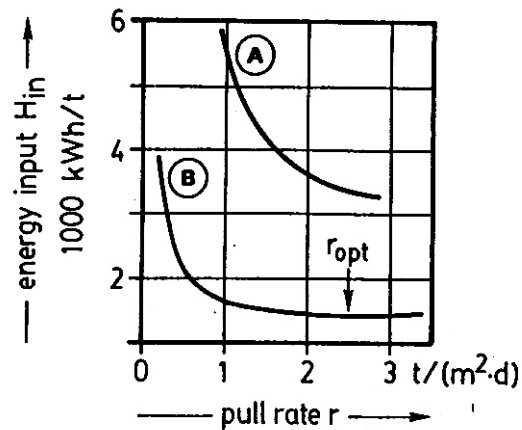


Fig. 6. Specific energy demand plotted versus the pull rate; tank A: small insulation glass fiber tank; tank B: average container glass tank [40]

## 2.2 Thermo-chemistry of primary melt formation

Solid state reactions are an essential part of batch melting; yet the predominant influence on the reaction rate is exerted by the first substantial amount of liquid phase generated in the system. The properties of this primary melt, i.e., the temperature of its occurrence, its viscosity, interfacial tension,

and affinity towards residual solids determine the further course of batch melting.

### 2.2.1 Direct melting (physical melting)

The most straight-forward way of primary liquid phase formation is direct (physical) melting. For typical mass glass batches, this refers to  $\text{Na}_2\text{CO}_3$  ( $T_{\text{liq}} = 858 \text{ }^\circ\text{C}$ ),  $\text{Na}_2\text{SO}_4$  ( $T_{\text{liq}} = 884 \text{ }^\circ\text{C}$ ),  $\text{NaNO}_3$  ( $T_{\text{liq}} = 310 \text{ }^\circ\text{C}$ ) and  $\text{NaCl}$  ( $T_{\text{liq}} = 800 \text{ }^\circ\text{C}$ ). The phase diagram in figure 7 shows the effect of mutual mixing with soda ash. The eutectic with  $\text{NaNO}_3$  ( $306 \text{ }^\circ\text{C}$ ) is located at 2.8 mol %  $\text{Na}_2\text{CO}_3$ ; hence mutual mixing with soda ash does not enhance melting very much. By contrast, the eutectic with  $\text{NaCl}$  brings about a significant effect.

The melts have low viscosities typical of completely dissociated ionic melts. In table 1, viscosity and surface tension values are compiled for different melts containing  $\text{Na}^+$  as the cation. In contrast to the silicate melts, the completely dissociated salt melts (carbonates, sulfates, nitrates, chlorides) have viscosity similar to liquid water, allowing them to rapidly fill the voids in the batch. The viscosity value even of the most basic orthosilicate melt is higher by two to three orders of magnitude.

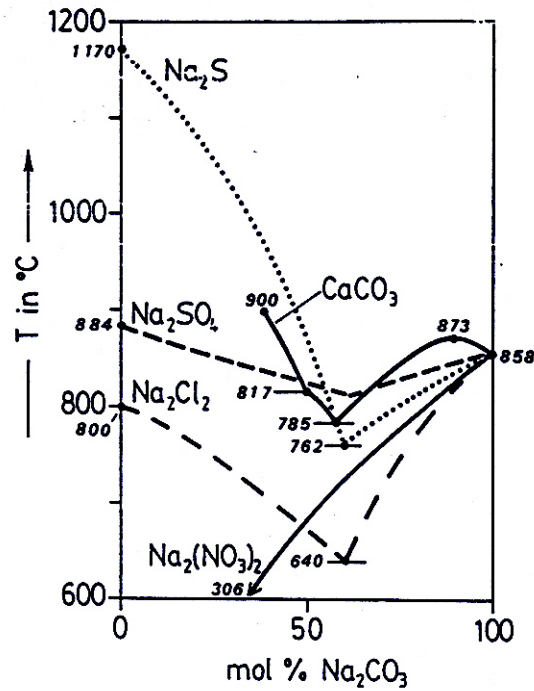


Fig. 7. Liquidus curves of the binary systems of Na<sub>2</sub>CO<sub>3</sub> with Na<sub>2</sub>S, Na<sub>2</sub>SO<sub>4</sub>, CaCO<sub>3</sub>, NaNO<sub>3</sub>, or NaCl; after [45]

Table 1. Viscosities and surface tensions of selected melts containing the cation Na<sup>+</sup>; after [46-48]

melts	T (°C)	log η (dPa.s)	η (dPa.s)	σ (N/m)	σ/η (cm/s)
Na <sub>2</sub> CO <sub>3</sub>	900	-1.52	0.030	0.210	7000
Na <sub>2</sub> SO <sub>4</sub> *)	900	-1.66	0.022	0.264	12100
NaNO <sub>3</sub>	490	-1.81	0.016	0.111	7100
NaCl	900	-2.00	0.010	0.107	10700
Na <sub>2</sub> Si <sub>2</sub> O <sub>5</sub>	1100	2.52	332.1	0.267	0.2
Na <sub>2</sub> SiO <sub>3</sub>	1100	1.54	34.4	0.236	2.3
Na <sub>4</sub> SiO <sub>4</sub>	1100	1.08	11.9	0.204	6.8

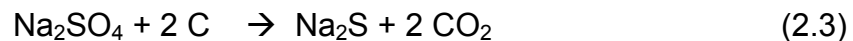
\*) η interpolated by sizes of [CO<sub>3</sub>]<sup>2-</sup> and [SO<sub>4</sub>]<sup>2-</sup>

The quotient  $\sigma/\eta$  of surface tension and viscosity is a direct measure for the velocity by which a melt enters a capillary, hence, for the velocity by which a primary melt penetrates the voids of a batch heap. This agrees well with the empirical observation that  $\text{Na}_2\text{SO}_4$  strongly enhances the wettability of the sand grains.

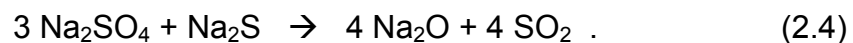
An important case of direct melting is the melting of cullet. It does not occur at a distinct temperature and does not involve a melting enthalpy, but rather proceeds as a sub-liquidus softening. Viscosity levels of  $\log \eta < 5$  are typically not found below 900 °C. So, molten cullet form highly viscous melts during batch melting.

### 2.2.2 Sulfate reduction

Sulfate reduction distinctly occurs under reducing conditions yielding  $\text{Na}_2\text{S}$  (beside other sodium sulfur compounds) as an intermediate product,

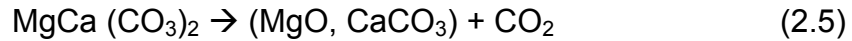


as seen from figure 7,  $\text{Na}_2\text{S}$  forms a low-temperature eutectic with  $\text{Na}_2\text{CO}_3$  at 762 °C thus acting as a melting accelerator. The temperature is among the lowest liquidus temperatures possibly established in mass glass batches. In a later stage of the melting process, at temperatures above 1300 °C,  $\text{Na}_2\text{S}$  is partially consumed by the reaction



### 2.2.3 Reactive carbonate melting

In a primary reaction stage, carbonates typically present in mass glass batches are soda ash, limestone, and dolomite. Upon heating-up, limestone decomposes to  $\text{CaO}$  and  $\text{CO}_2$  at 900 °C and 800 °C in atmospheres with 1 bar and 0.2 bar  $\text{CO}_2$  partial pressure, respectively. Dolomite decomposes in two steps. The first step is completed at 680 to 750 °C, depending on the kind of dolomite,



The second one is identical to the limestone decomposition [49].



The decomposition of dolomite and limestone are the source of the largest endothermic contributions to  $H_{\text{chem}}$ .

None of the above reactions generates primary melt. However,  $\text{Na}_2\text{CO}_3$  and  $\text{CaCO}_3$  form a low-temperature eutectic at  $785^\circ\text{C}$  located between the reaction point of  $\text{Na}_2\text{Ca}(\text{CO}_3)_2$  (“double salt”) at  $817^\circ\text{C}$  and pure  $\text{Na}_2\text{CO}_3$ . The corresponding soda lime melt has a low viscosity typical of ionic melts.

After that the carbonate route towards ternary silicates is taking place. The direct reaction between  $\text{SiO}_2$  and  $\text{CaCO}_3$  is of little significance for the overall reaction rate [4, pt.II]. However, with a soda lime melt already present, a reaction of the type takes place:

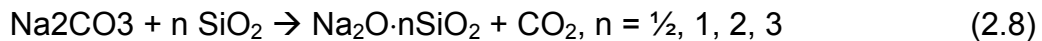


This approach towards the ternary silicate melts shall be termed “carbonate route”. It accounts, under certain boundary conditions, for a sudden and substantial increase of the overall reaction rate in a melting batch at  $785^\circ\text{C}$  [4, pt III]; this coincides with the eutectic  $\text{Na}_2\text{Ca}(\text{CO}_3)_2 - \text{Na}_2\text{CO}_3$ . A typical feature of the carbonate route is the low viscosity of the educts melt.

## 2.2.4 Reactive silicate melting

### a) Sodium silicate formation

Yet another type of primary reactions is possible. These are the reactions between soda ash and quartz. They typically occur as solid state reactions already and proceed according to the pattern [50]



Thermodynamic stability of the silicates increases along with  $n$ . The case  $n = 3$  is reported in [50], however not documented in well-established phase diagrams [45]. Phase diagrams usually present the case  $n = 3/8$  instead, corresponding to an incongruently melting compound  $3\text{Na}_2\text{O} \cdot 8\text{SiO}_2$ . In contrast to its apparent simplicity, the silicate route confronts the investigator with many unsolved questions.

An investigation of the thermodynamic equilibria of sodium silicate formation reveals a surprising fact. The Gibbs free energies of reaction turn negative for temperature above 300 °C. In other word, sodium silicate formation is thermodynamically favored at very low temperatures already. The reactions are endothermic, involving a heat turnover of 40 to 80 kJ per mol of consumed  $\text{SiO}_2$  (quartz). For comparison, the evaporation of 1 mol of water requires 41 kJ. The data are compiled in table 2. Heat supply during batch melting is very unlikely to become a rate limiting factor of these reactions. So the fact that sodium silicates are not formed as early as expected from thermodynamics, is due to some severe kinetic constraints, among which are atomic mobility of the  $\text{Na}^+$  and grain-to-grain contact. Therefore, the rate of sodium silicate formation is expected to gain momentum only when the constraints are lifted. The most likely mechanism to lift the constraints is primary melt formation.



Table 2. Heat of reaction  $H_R$  of silicate formation from quartz, soda ash, and limestone;  $T_{eq}$  = equilibrium temperature, i.e., the temperature at which the Gibbs free energy of reaction becomes zero; calculated from data by [51]

reaction products	$T_{eq}$ In °C	$H_R$ in kJ per mol $SiO_2$	$H_R$ in kJ per mol $Na_2CO_3$	$H_R$ in kJ per mol $SiO_2$	$H_R$ in kJ per mol $Na_2CO_3$
		for $T = T_{eq}$		for $T = 858\text{ °C}$	
$2Na_2O \cdot SiO_2$	703	237	119	163	82
$Na_2O \cdot SiO_2$	287	81	81	33	33
$Na_2O \cdot 2SiO_2$	256	42	84	42	84
$2Na_2O \cdot CaO \cdot 3SiO_2$	281	82	123	43	65
$Na_2O \cdot 2CaO \cdot 3SiO_2$	175	70	210	43	129
$2Na_2O \cdot SiO_2$	703	237	119	163	82

The eutectic  $NS_2$ -S at 799 °C in figure 8 may attract our attention first. Yet, the viscosity of this eutectic melt ( $\approx 10^5$  dPa.s) is high, hence  $Na^+$  mobility is low. In fact, an increase of batch melting rates at 800 °C has not been observed. Hrma [18] suggests the formation of orthosilicate  $N_2S$  as the primary step. The eutectic N- $N_2S$  at 800 °C (figure 9) would indeed generate a melt with low viscosity. However, the location of the equilibrium (table 2), and the relatively high temperatures which separate the compound  $N_2S$  from the metasilicate NS cast some doubt on the assumption that this reaction has a key role in batch melting. Based on thermodynamic and kinetic data, we conclude that the formation of the meta- and disilicate ( $n = 1, 2$ ) predominates. This is clearly reflected by the fact that the reaction rate in soda ash + sand mixtures displays a sudden increase at approx. 840 °C [5] corresponding to the NS- $NS_2$  eutectic. Primary melt is not recognizable below this temperature, but clearly appears below the physical melting of soda ash at 858 °C.

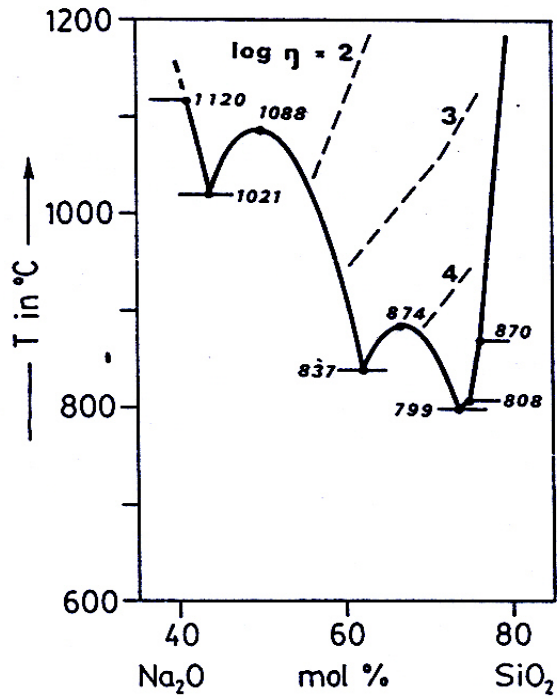


Fig. 8. Liquidus curve and melt viscosities in the binary system Na<sub>2</sub>O-SiO<sub>2</sub>; re-designed after [45] and [52]

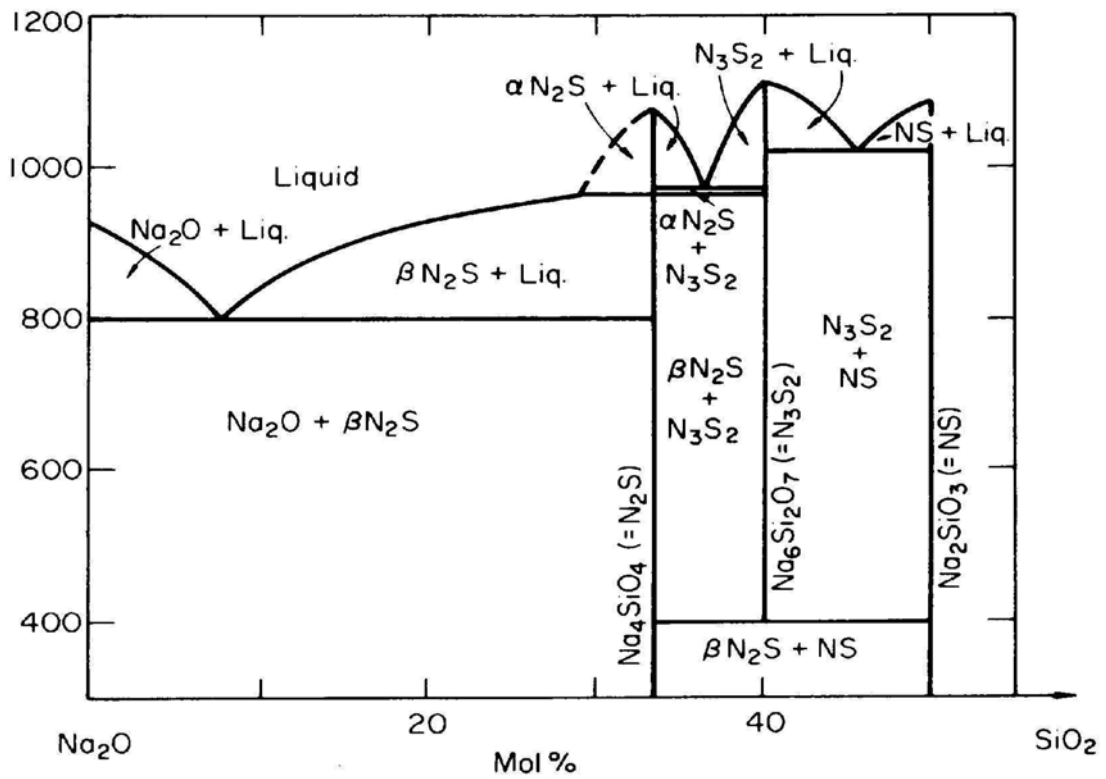


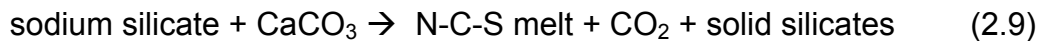
Fig. 9. Liquidus curve and location of compounds in the binary system Na<sub>2</sub>O-SiO<sub>2</sub>, sodia-rich part [45]

**b) The silicate route towards ternary silicates**

The further course of batch reactions following the formation of sodium silicates depends on the nature of the other batch components, e.g. dolomite or limestone. Batches containing limestone as the predominant alkaline earth carrier shall be termed as “limestonic batches”, batches using dolomite as “dolomitic batches”.

**c) The silicate route in limestonic batches**

In a batch predominantly using limestone, the system  $\text{Na}_2\text{O-CaO-SiO}_2$  governs the course of reaction. Figure 10 gives an overview over the technically relevant range of this system. Figure 11 displays the boundary of the crystallization field of sodium disilicate. The silicate route starts at the eutectic NS-NS<sub>2</sub> and follows this boundary. The general type of reaction is generated ternary silicates melt.



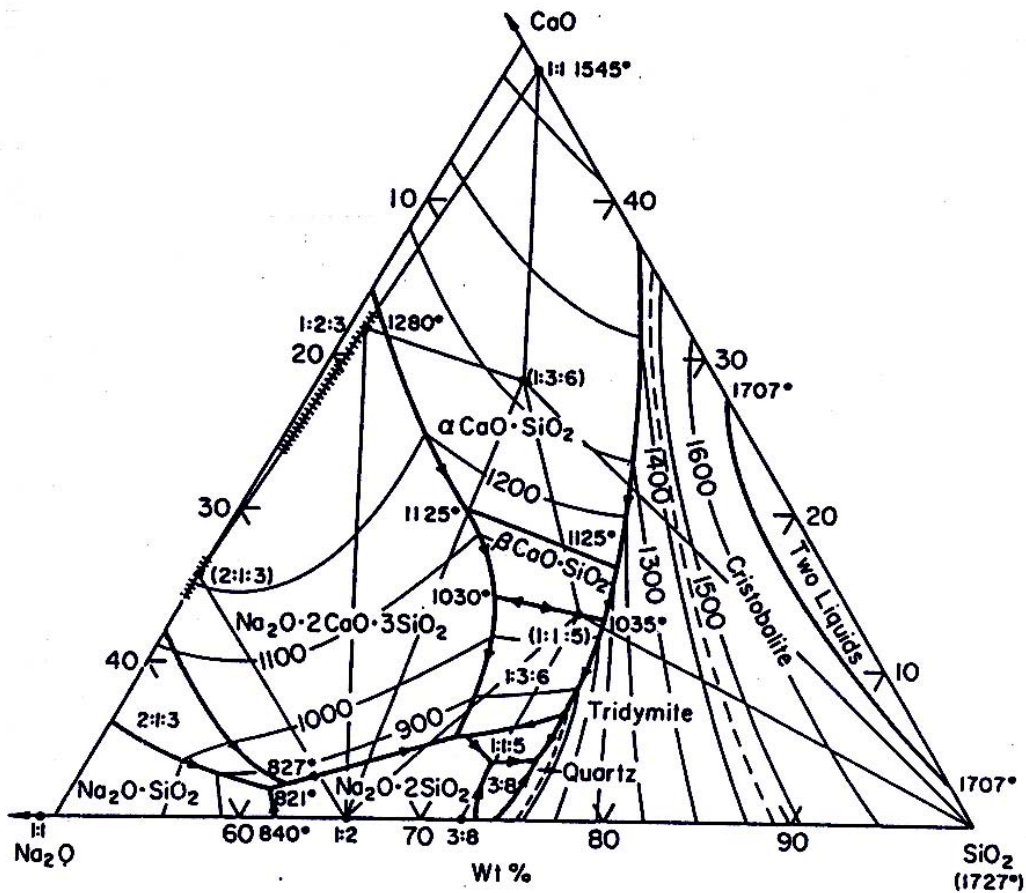


Fig. 10. Ternary system  $\text{Na}_2\text{O}-\text{CaO}-\text{SiO}_2$ , technologically relevant range [45]

According to figure 11, the dissolution of  $\text{CaCO}_3$  by the binary  $\text{NS}-\text{NS}_2$  melt immediately lowers the temperature of primary melt formation from 837 to 821 °C. The access to the still lower metastable ternary eutectic M at 760 °C (representing the constitutional phase triangle  $\text{NS}_2-\text{NC}_3\text{S}_6-\text{S}$  valid for most industrial mass glasses), however, is restricted by the binary cut  $\text{NS}_2-\text{NC}_2\text{S}_3$  at 870 °C. So, for the silicate route, primary melt is expected to occur between 837 and 821 °C, depending on the velocity of limestone dissolution.

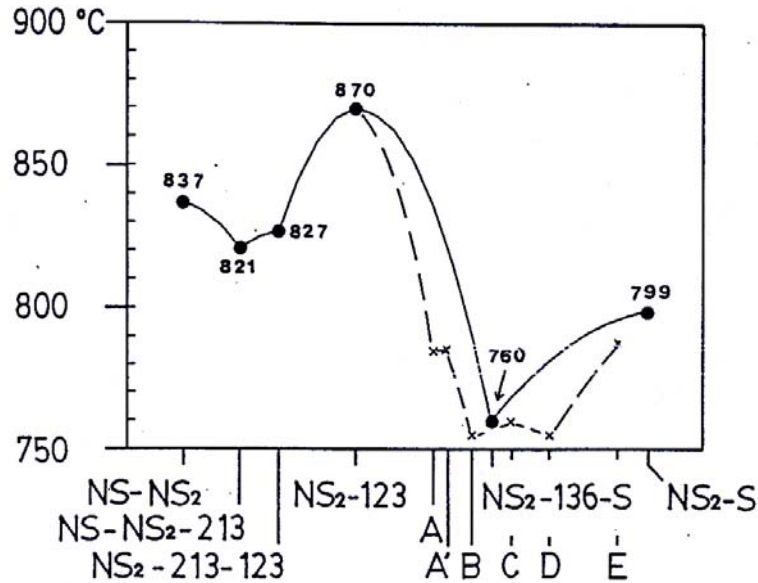


Fig. 11. Ternary system  $\text{Na}_2\text{O-CaO-SiO}_2$ , boundary of the crystallization field of sodium disilicate; solid line: path to metastable eutectic at  $760^\circ\text{C}$ ; dashed line: equilibrium conditions; invariant points along the dotted line: A:  $\text{NS}_2\text{-213-115}$ ; A':  $\text{NS}_2\text{-136-115}$ ; B :  $\text{NS}_2\text{-115-38}$ ; C:  $38\text{-115}$ ; D:  $38\text{-115-S}$ ; E:  $38\text{-S}$

The metastable eutectic at  $760^\circ\text{C}$ , denoted by M, can be accessed by the carbonate route only. The immediate vicinity of point M is presented in figure 12. This revised version of the N-C-S phase diagram, although it may cast some doubt on an earlier interpretation of the exact reaction mechanism [4, pt. III], predicts liquidus temperatures at approx.  $760^\circ\text{C}$ . This goes together well with the sudden and substantial increase of the overall reaction rate observed at this temperature under certain boundary conditions [4, pt. III]. This observation shows that the silicate and the carbonate route always compete with each other during batch melting. The rate of formation of double salt  $\text{Na}_2\text{Ca}(\text{CO}_3)_2$  versus the rate of dissolution of limestone in sodium silicate melt determine the ultimate course of batch melting.

A typical feature of the silicate route is the involvement of comparatively viscous melts during all its stages. The viscosities of the binary sodium silicate melts assume  $\log \eta = 3$  to 4 (see figure 9). Using data by [46], the viscosities of the ternary N-C-S melts at respective liquidus temperatures are estimated to assume  $\log \eta \approx 5$  to 6,  $\eta$  in dPas. The viscosity line represented in figure 12 a refers to a temperature level of  $900^\circ\text{C}$ . A variant of

the silicate route occurs in the presence of feldspar (figure 12 b). Albite, for example, forms a binary eutectic in the sub-system NS<sub>2</sub>-NAS<sub>6</sub> (767 °C,  $\log \eta \approx 5.5$ ) and a ternary one in the sub-system NS<sub>2</sub>-NAS<sub>6</sub>-S (740 °C,  $\log \eta \approx 6.5$ ). It is, however, not clear how the presence of feldspar influences the formation of N-C-S melts.

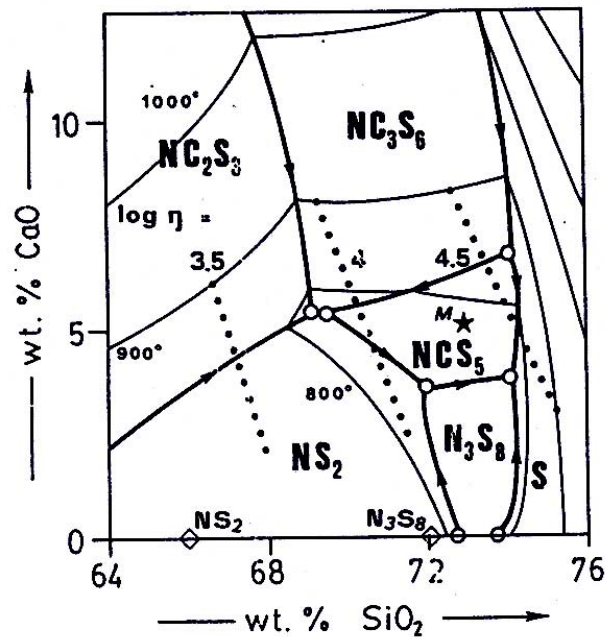


Fig. 12 a. Ternary phase diagram Na<sub>2</sub>O-CaO-SiO<sub>2</sub>; re-designed after [45]; melt viscosities ( $\eta$  in dPa·s, estimated after [46]) refer to  $T = 900$  °C; the temperatures of the invariant points (in anti-clockwise order, starting with NC<sub>3</sub>S<sub>6</sub>-NC<sub>2</sub>S<sub>3</sub>-NS<sub>2</sub>) are 785,  $\leq 785$ ,  $\approx 760$ , 799, 808,  $\leq 760$ , 827 °C; M is the metastable eutectic NC<sub>3</sub>S<sub>6</sub>-NS<sub>2</sub>-S at  $\approx 760$  °C

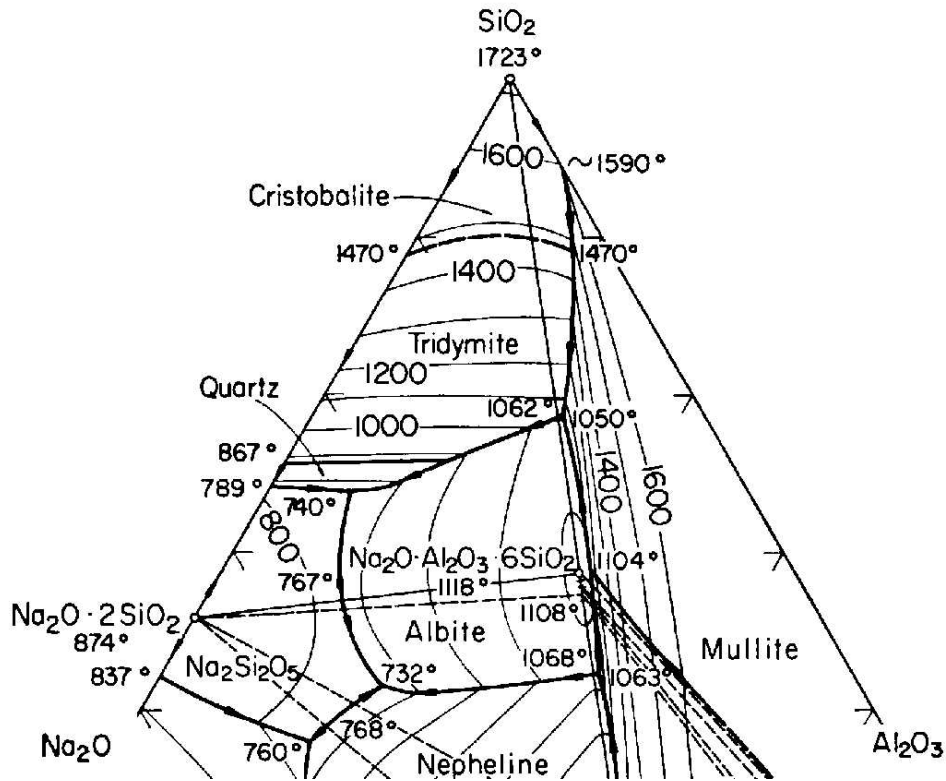


Fig. 12 b. Ternary phase diagram  $\text{Na}_2\text{O}-\text{Al}_2\text{O}_3-\text{SiO}_2$ ; after [45]

#### **d) The silicate route in dolomitic batches**

In a batch predominantly using dolomite, the system  $\text{Na}_2\text{O}-\text{MgO}-\text{SiO}_2$  overrules, at least to a certain extent, the patterns of N-C-S formation. This can be seen from figures 13 and 14. Figure 13 gives an overview of the ternary system  $\text{Na}_2\text{O}-\text{MgO}-\text{SiO}_2$  with its most complicated phase relationship, while figure 14 presents the phase boundary of the crystallization field of sodium disilicate.

$\text{Na}_2\text{O}-\text{MgO}-\text{SiO}_2$

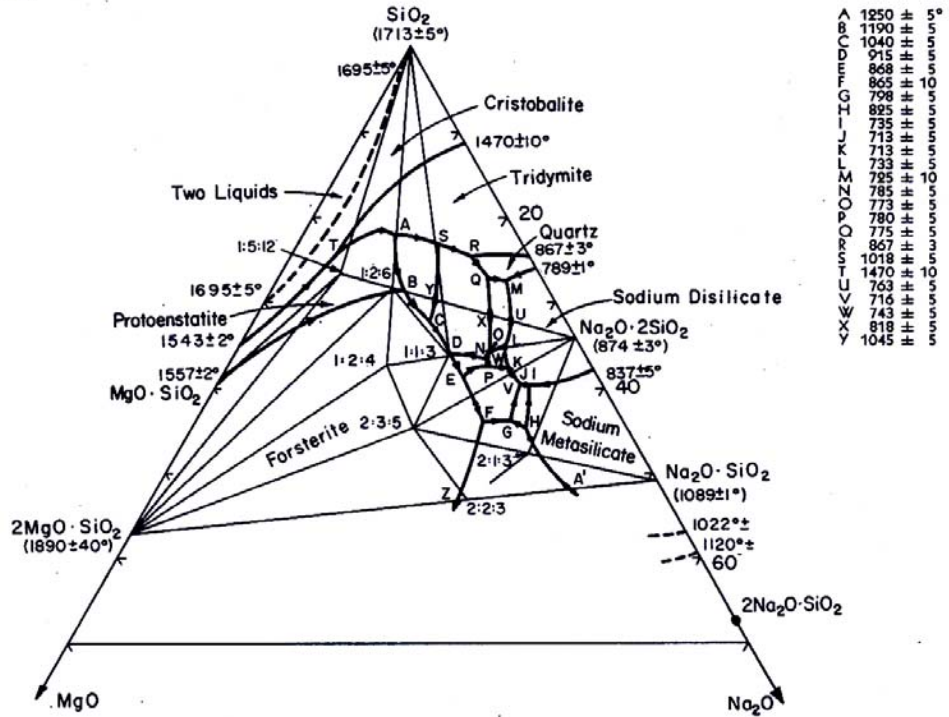


Fig. 13. Ternary system  $\text{Na}_2\text{O}-\text{MgO}-\text{SiO}_2$  [45]

Let us assume that the silicate route starts at the eutectic NS-NS<sub>2</sub> and follows this boundary. It is most interesting to note that the dissolution of MgO in the NS-NS<sub>2</sub> melt immediately lowers the temperature of primary melt formation by more than 100 K, i.e., from 873 to 713 °C, which is the lowest temperature met along the boundary. It is possibly also the lowest temperature of primary melt formation encountered in a mass glass batch. After all, based on this discussion, the melting behavior of limestonic and dolomitic batches is expected to differ considerably.



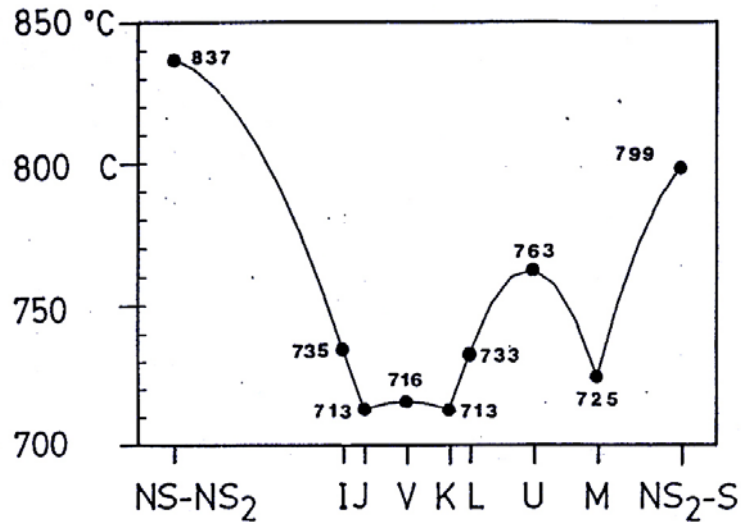


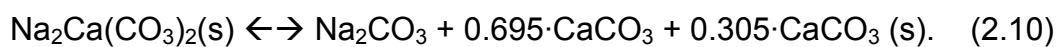
Fig. 14. Ternary system  $\text{Na}_2\text{O-MgO-SiO}_2$ , boundary of the crystallization field of sodium disilicate

## 2.2.5 Thermochemical data

Thermochemical data are compiled for the most important phases involved in batch melting. This is done as a preparation of a fully quantitative treatment of batch melting in future work. Data are mostly taken from [51]; for the ternary silicates, [50] is used as the main source. A difficulty arises from the fact that no tabulated data exist for the double salt  $\text{Na}_2\text{Ca}(\text{CO}_3)_2$ . However, by a tedious evaluation and compilation of information hidden in earlier papers [53, 54], the following data for solid  $\text{Na}_2\text{Ca}(\text{CO}_3)_2$  are derived:

$$\begin{aligned} H^{298} &= -2399.10 \text{ kJ/mol} \\ S^{298} &= 185.14 \text{ J/ (mol}\cdot\text{K)}, \\ \alpha &= 147.61 \text{ J/ (mol}\cdot\text{K)}, \\ \beta &= 153.26 \cdot 10^{-3} \text{ J/ (mol}\cdot\text{K}^2), \\ C_p &= \alpha \cdot \beta T, \text{ T in K} \end{aligned}$$

Incongruent melting occurs at 817 °C according to



The heat of mixing of the molten phase is given by

$$H^{MIX}(817^{\circ}C) = b_{Na-Ca} \cdot \left[ \frac{0.5 \cdot n_{Na}}{n_{Ca} + 0.5 \cdot n_{Na}} \right]^2 \approx -3.45 \text{ kJ/mol} \quad (2.11)$$

with  $n_{Na} = 2$  and  $n_{Ca} = 0.695$  as the molar amounts of the respective ions in the liquid phase and  $b_{Na-Ca} = 9.92 \text{ kJ}$  as the interaction parameter [53]. The hypothetical liquid state  $\text{CaCO}_3$  in this binary system has a melting point of  $1190^{\circ}\text{C}$ , and a heat of fusion of  $36.8 \text{ kJ/mol}$  [53]. The Gibbs free energy of the molten phase thus amounts to

$$\begin{aligned} G_{melt}(817^{\circ}C) &= \sum n_j \cdot G_j + R \cdot T \cdot \sum n_j \cdot \ln(x_j) + H^{MIX} \\ &= -2322.6 \text{ kJ/mol}, \end{aligned} \quad (2.12)$$

$j = \text{Na}_2\text{CO}_3, \text{CaCO}_3$ . Complete melting is reached at  $885^{\circ}\text{C}$  [51]. The heat of melting with respect to the solid  $\text{Na}_2\text{Ca}(\text{CO}_3)_2$  is derived as  $H^m = 146.4 \text{ kJ/mol}$ ; the heat capacity of the melt (Dulong Petit limit) is  $345.4 \text{ J/(mol}\cdot\text{k)}$ . In the four following tables, enthalpy and Gibbs free energy values of the most important products and educts of batch melting reactions are compiled.

Table 3. Enthalpies and Gibbs free energies (negative values) of selected carbonate and silicate compounds in kJ/mol; carbonates: CO<sub>2</sub> gas, Na<sub>2</sub>CO<sub>3</sub> solid-liquid, rest solid; silicates: SiO<sub>2</sub> quartz, NS<sub>2</sub> solid-liquid, rest solid

Carbonates enthalpies –H(T) in kJ/mol

T in °C	CO <sub>2</sub>	Na <sub>2</sub> CO <sub>3</sub>	CaCO <sub>3</sub>	MgCO <sub>3</sub>	MgCa(CO <sub>2</sub> ) <sub>3</sub>	Na <sub>2</sub> Ca (CO <sub>3</sub> ) <sub>2</sub>
25	393.5	1129.7	1206.9	1095.8	2315.0 <sup>*)</sup>	2399.1
100	390.5	1121.1	1200.3	1089.7	2302.6	2384.2
200	386.2	1106.3	1190.3	1080.4	2284.8	2362.9
300	381.7	1093.5	1179.7	1070.3	2265.6	2340.2
400	376.9	1076.6	1168.6	1059.3	2245.5	2315.8
500	372.0	1059.2	1157.0	1047.7	2224.4	2290.0
600	367.0	1043.6	1145.1	1035.4	2202.4	2262.6
700	361.8	1026.7	1133.0	1022.5	2179.5	2233.7
800	356.6	1008.4	1120.5	1009.0	2155.8	2203.3
900	351.2	959.6	1107.8	994.8	2131.3	2024.6
1000	345.7	940.7	1094.9	980.1	2105.9	1990.0

\*) [55-56]

Carbonates Gibbs free energies –G(T) in kJ/mol

T in °C	CO <sub>2</sub>	Na <sub>2</sub> CO <sub>3</sub>	CaCO <sub>3</sub>	MgCO <sub>3</sub>	MgCa(CO <sub>2</sub> ) <sub>3</sub>	Na <sub>2</sub> Ca (CO <sub>3</sub> ) <sub>2</sub>
25	457.2	1170.0	1234.5	1115.4	2361.3	2454.3
100	473.6	1181.1	1242.2	1121.1	2374.3	2469.9
200	496.4	1198.7	1254.7	1130.6	2395.7	2495.5
300	520.1	1219.2	1269.3	1142.2	2421.0	2525.7
400	544.6	1242.5	1285.9	1155.7	2449.8	2560.1
500	569.9	1268.5	1304.9	1170.8	2481.6	2598.2
600	595.8	1296.5	1323.9	1187.5	2516.3	2639.7
700	622.3	1326.4	1345.0	1205.6	2553.5	2684.5
800	649.3	1358.1	1367.5	1225.1	2593.1	2732.3
900	676.8	1392.6	1391.0	1245.9	2634.9	2784.9
1000	704.8	1430.3	1415.7	1267.9	2678.9	2851.2

Table 3. continued

Silicate enthalpies  $-H(T)$  in kJ/mol

T in °C	SiO <sub>2</sub>	NS <sub>2</sub>	NS	N <sub>2</sub> S	CS	MS	CMS <sub>2</sub>	NC <sub>2</sub> S <sub>3</sub>	N <sub>2</sub> CS <sub>3</sub>	NC <sub>3</sub> S <sub>3</sub>
25	910.9	2473.6	1563.1	2101.2	1635.1	1548.5	3202.3	4883.6	4763.0	8363.8
100	907.3	2460.9	1554.1	2087.1	1628.2	1542.0	3189.4	4860.4	4737.8	8328.0
200	901.8	2441.9	1540.9	2067.7	1618.0	1532.4	3169.5	4826.6	4701.5	8277.1
300	895.7	2421.3	1526.8	2047.6	1607.0	1522.1	3147.7	4791.0	4663.2	8223.5
400	889.2	2399.5	1512.0	2026.7	1595.7	1511.3	3124.5	4754.0	4623.6	8167.7
500	882.2	2376.6	1496.6	2005.1	1583.9	1500.0	3100.4	4716.0	4582.9	8109.7
600	874.2	2352.9	1480.6	1982.7	1572.0	1488.4	3075.4	4677.0	4541.2	8049.8
700	867.4	2328.4	1464.2	1959.6	1559.7	1475.7	3049.7	4637.3	4498.7	7987.9
800	860.5	2297.0	1447.3	1935.8	1547.3	1463.6	3023.6	4596.8	4455.3	7924.2
900	853.5	2233.0	1430.0	1911.2	1534.7	1451.6	2997.1	4555.7	4411.2	7858.6
1000	846.4	2206.8	1412.2	1885.8	1521.9	1437.9	2970.3	4513.8	4366.3	7791.3

Table 3. continued

Silicate Gibbs free energies  $-G(T)$  in kJ/mol

T in °C	SiO <sub>2</sub>	NS <sub>2</sub>	NS	N <sub>2</sub> S	CS	MS	CMS <sub>2</sub>	NC <sub>2</sub> S <sub>3</sub>	N <sub>2</sub> CS <sub>3</sub>	NC <sub>3</sub> S <sub>3</sub>
25	923.3	2522.6	1597.0	2159.6	1659.9	1568.7	3245.0	4966.4	4855.3	8501.5
100	926.8	2536.4	1606.6	2175.9	1666.9	1574.6	3257.2	4989.9	4881.3	8540.3
200	932.7	2558.9	1622.2	2202.1	1678.5	1584.5	3277.7	5028.7	4924.4	8603.3
300	939.8	2585.7	1640.8	2232.4	1692.4	1596.5	3302.7	5074.9	4975.4	8677.5
400	948.0	2616.1	1661.9	2266.4	1708.2	1610.4	3331.7	5127.5	5032.9	8761.3
500	957.3	2649.9	1685.3	2303.5	1725.5	1625.9	3364.1	5185.6	5096.6	8853.6
600	967.5	2686.7	1710.7	2343.5	1744.8	1642.9	3399.8	5248.8	5165.6	8953.5
700	978.5	2726.3	1737.9	2386.1	1765.3	1661.3	3438.4	5316.5	5239.5	9060.4
800	990.3	2768.9	1766.9	2431.1	1787.0	1681.0	3479.6	5388.3	5317.7	9137.8
900	1002.7	2815.0	1797.4	2478.3	1809.9	1701.8	3523.3	5463.9	5400.1	9293.2
1000	1015.7	2865.6	1829.5	2527.7	1833.9	1723.6	3569.3	5543.0	5486.2	9418.2

## 2.3 Macro-kinetics of batch melting

According to a simplified model by Trier [57], the melting of a batch proceeds in five different phases. They are characterized by the following quantities:

$A$	=	contact area between batch heap and glass melt; $m^2$ ;
$c_p$	=	heat capacity of the batch heap; $\text{kJ}/(\text{kg}\cdot\text{K})$ ;
$H_r$	=	specific enthalpy of reaction; $\text{kJ}/\text{kg}$ ;
$J_Q$	=	heat flow into the batch heap; $\text{kW}/m^2$ ;
$M$	=	mass of the batch heap; $\text{kg}$ ;
$\rho$	=	bulk density of the batch heap; $\text{kg}/m^3$ ;
$s$	=	$m/(q\cdot A)$ = height of the batch heap; $m$ ;
$T_0$	=	room temperature; $\text{K}$ ;
$T_R$	=	reaction temperature; $\text{K}$ .

### a) Phase 1: warming-up

During this phase,  $\partial m / \partial t = 0$ . The thickness of the batch heap thus remains constant.  $T < T_R$  all over the batch heap. The heat flow  $J_Q$ , and hence the heating rate  $\partial T / \partial t$  are functions of the position in the batch.

### b) Phase 2: melting onset

In the outermost layers,  $T = T_R$  is reached. The melting rate is non-zero and increases with time:  $\partial m / \partial t > 0$ ,  $\partial^2 m / \partial t^2 > 0$ . The heat flow  $J_Q$ , and hence the heating rate  $\partial T / \partial t$  are still functions of the position in the batch. The portion of the heat flow consumed by melting increases on the account of the portion available to warm up the inner zones of the batch heap. The maximal temperature difference in the batch is  $T_R - T_0$ .

### c) Phase 3: quasi-stationary melting

The portions of the heat flow consumed by melting and available for warming up the inner zones assume a constant ratio. The melting rate

becomes constant:  $\partial m / \partial t > 0$ ,  $\partial^2 m / \partial t^2 = 0$ . A melting front with constant temperature  $T_R$  moves towards the inner zones of the batch heap. The maximal temperature difference in the batch is still  $T_R - T_0$ . During the quasi-stationary phase, the following simple relation holds:

$$\frac{\partial m}{A \cdot \partial t} = \frac{J_Q}{H_R + c_p \cdot (T_R - T_0)} \quad (2.13)$$

#### **d) Phase 4: final acceleration of melting**

The temperature fields originating from the upper and the lower boundary of the batch heap overlap. The minimal temperature in the batch is now significantly higher than  $T_0$ . The heat flow  $J_Q$  decreases accordingly. Nevertheless, an increasing portion of the heat flow becomes available to promote the melting reaction. Melting is accelerated once again:  $\partial m / \partial t > 0$ ,  $\partial^2 m / \partial t^2 > 0$ .

#### **e) Phase 5: end of batch melting**

Eventually, the upper and lower melting fronts meet within the batch heap. The exact position depends on the boundary temperature, i.e., the temperature of the upper and lower heat reservoir, the respective heat transfer coefficients, and the transport of established melt and liberated gases within the batch heap. The time required to reach phase 5 may be identified with the batch-free time used by other authors [22-23].

According to computer simulations on cullet free batch [34], the thermal conductivity of the batch heap has little influence on the overall time demand of batch melting. High thermal conductivity, however, expands phases 1-2 and 4-5 on the account of the quasi-stationary phase 3. The situation changes with cullet in the batch [41].

The above concept contains a number of over-simplifications. Firstly, melt is assumed to drain off “immediately” after its formation. Secondly, melt is assumed to occur at a uniform temperature  $T_R$ . However from the point of

view of chemistry, the meaning of  $T_R$  is not clear. There is experimental evidence that the actual reaction path strongly depends on the local heating rate. The silicate route is found to predominate at moderate to slow heating rates (10 K/min) while the carbonate route takes over at rapid heating (documented for approx. 30 K/s) [12]. So the melting temperature valid for the rapidly heated outer batch zones is expected to differ from the melting temperature valid for the inner zones. Beyond this, the reaction velocities of both the carbonate and silicate route sensitively depend on the local  $\text{CO}_2$  partial pressure [4, pt. IV], rendering reactions slowest in pure  $\text{CO}_2$  atmosphere. For extended batch heaps, the reaction rates thus once again become a function of a local parameter.

Ungan and Viskanta [37] present a more elaborate version of the same ideas. In their model, two temperature levels are introduced, replacing the rather crude concept of a single reaction temperature  $T_R$ . The first temperature refers to the transition between a “dry” granular bulk solid and a bulk solid drenched by a molten phase, the second temperature refers to the transition between the latter stage and a rough melt. As shown later by own experiments, this scenario comes very close to what actually happens in a melting batch.

## 2.4 Micro-kinetics and electrical conductivity

The concept of using the electrical conductivity in the batch heap as an indicator of primary melt formation goes together well with the importance of this event for the batch melting process. As discussed before, the formation of binary and ternary silicates is favored by the thermochemical driving forces at temperatures as low as 300 °C already. Reaction rates, however, remain very low due to the constraints imposed by poor grain-to-grain contact and low  $\text{Na}^+$  ion mobility. Thus, the reaction rates depend on the chemistry and the micro-kinetics in the very same way as the electrical conductivity. Therefore, the electrical conductivity is a quantity well suited, not only to indicate the occurrence of primary melt, but also to get a hold of the reaction rates.



### 2.4.1 Primary melt formation and electrical conductivity

Electrical conductivity is chosen as the local indicator of the first occurrence of liquid phase. This approach has been suggested and tried before [20, 65]. Actually, however, the relation between liquid phase formation and electrical conductivity in a multiphase system is not unambiguous and requires some discussion beforehand. In a continuous one-phase (solid or liquid) electrolyte system, electrical conductivity is directly correlated to ionic mobility (ionic diffusion). As visualized from a simple hopping mechanism, ionic mobility depends on the free space available for the ionic motion (defect concentration, free volume) and on the activation energy of the motion itself. As the Na<sup>+</sup> ion is the predominant charge carrier in commercial batch compositions, the behavior of sodium salts in general is discussed. In the solid state, ionic mobility is limited by the defect concentration. Diffusion coefficients,  $D$ , typically assume values in the range of  $10^{-11}$  to  $10^{-8}$  cm<sup>2</sup>/s. For example, solid NaCl has  $7.5 \cdot 10^{-11}$  cm<sup>2</sup>/s at 550 °C and  $5 \cdot 10^{-9}$  cm<sup>2</sup>/s at 750 °C, the exact values depending on the impurity level. At increasing temperature, yet well below the liquidus temperature, an abrupt increase (cross-over) of the temperature coefficient of  $D$  from impurity to thermally induced defect formation is observed. This cross-over must not be mistaken for liquid phase formation. In the liquid state, values of  $10^{-6}$  cm<sup>2</sup>/s are typical. Since defect (or better: free volume) formation now becomes less important, the temperature coefficient of  $D$  is determined by the ionic motion alone, hence, becomes smaller again. This second cross-over indicates the formation of liquid phase. Figure 15 illustrates the behavior for KCl salt (for lack of a curve for NaCl).

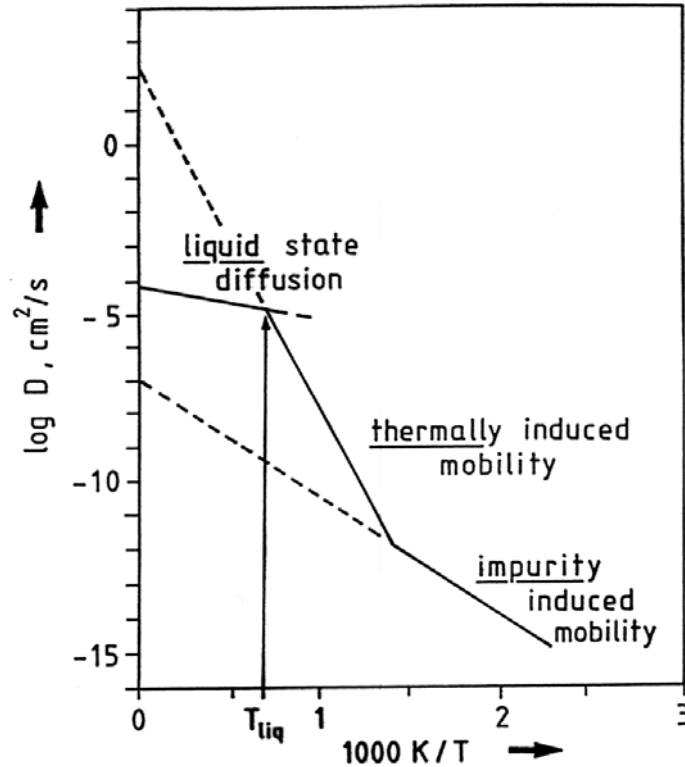


Fig. 15. Diffusion-temperature plot for KCl with  $10^{-5}$  atom fraction divalent cation impurities; data for the solid state from [58], for the liquid state from [48]

In a heterogeneous multiphase system like a batch heap, the situation becomes more complex. In addition to the mentioned mechanisms, electrical conductivity becomes also limited by grain-to-grain contact. Sintering of the solid grains is expected to yield some increase already, which is further enhanced by the local occurrence of isolated portions of liquid phase. The most significant conductivity increase, however, is expected when an interconnected liquid film is established, followed by a slight further increase when the volume fraction of liquid phase grows. The joint effect of ionic mobility and grain-to-grain contact may lead to conductivity-temperature functions which are difficult to interpret in detail. Yet, the point where the conductivity increase by three to four orders of magnitude is terminated can be taken as an unambiguous indicator of an established interconnected liquid phase. This is verified in the experimental part (see figure 35 on page 64).

## 2.4.2 Further generation of liquid phases

As said before in chapter 2.2, the stage where primary melt has formed is characterized by the presence of un-reacted original batch constituents, intermediate crystalline reaction products, and melt. There are two kinds of melts that can be produced in the batch: ionic low-viscosity melts and glass forming melts with much higher viscosity. Hence, three basic situations can occur: (i) presence of molten salts without glass forming melt, (ii) presence of glass forming melt without molten salt, (iii) presence of both melts. These two types of melts are partly mutually soluble. As said before, the viscosity of molten silicates and borates is about six orders of magnitude higher. When consulting the field encompassed by the 900 °C isotherm in figure 16, the wide composition range of low-liquidus silicate melts is seen. As said before, the temperature minimum settles somewhere around 760 °C.

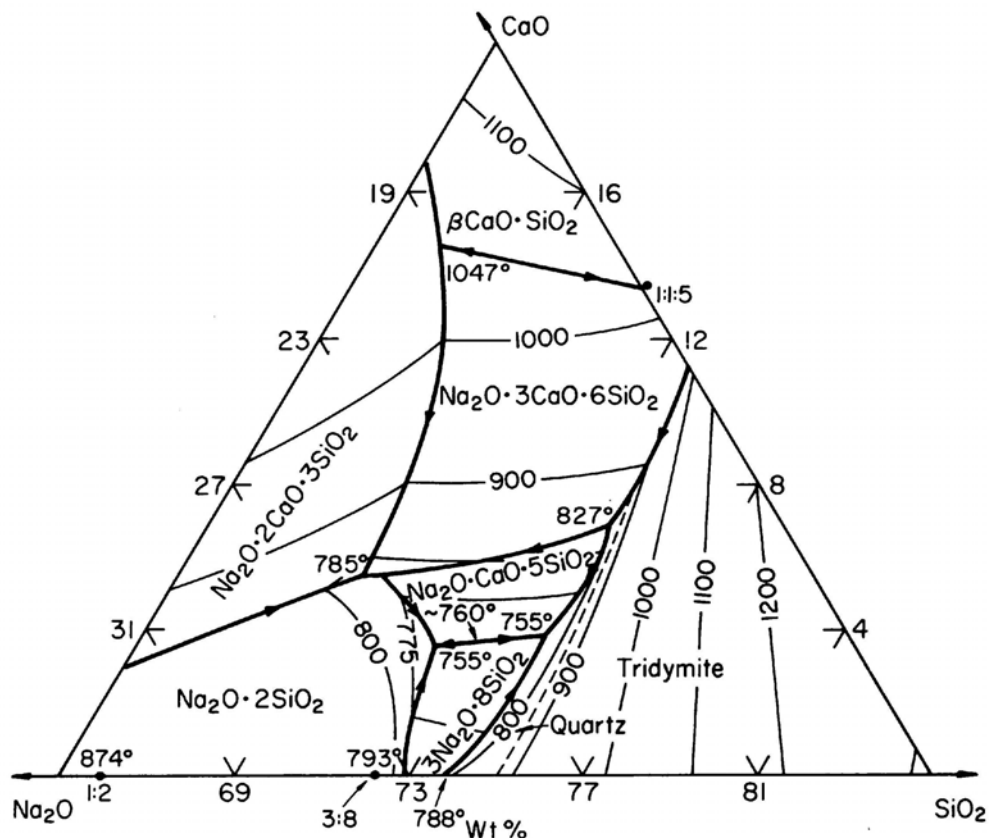


Fig. 16. Ternary phase diagram of Na<sub>2</sub>O-CaO-SiO<sub>2</sub>

The process in a multi-phase batch right after primary melt formation is most complicated: some primary melts readily wet solid phases, until their

surfaces are completely coated. Precipitating solid products reduce the amount of melt and a large number of tiny precipitated crystals hold the melt and obstruct its mobility. Reduced fraction of melt means thinner liquid films enhanced due to shorter diffusion distances. If gaseous products evolve, liquid is stirred, which enhances diffusion, but gas may also separate liquid from solid, thus inhibiting reaction. Finally, a combination of steep concentration gradients within the liquid phase and a large gas-liquid interface area introduce surface tension gradients that drive additional convection.

As the amount of melt increases, batch volume initially decreases because of sintering and pulling solid particles together by melt bridges. Heat conductivity of the batch is reduced again when foam develops. The individual stages of primary melt formation (conductivity jump) and thermal diffusivity increase are shown in figure 17.

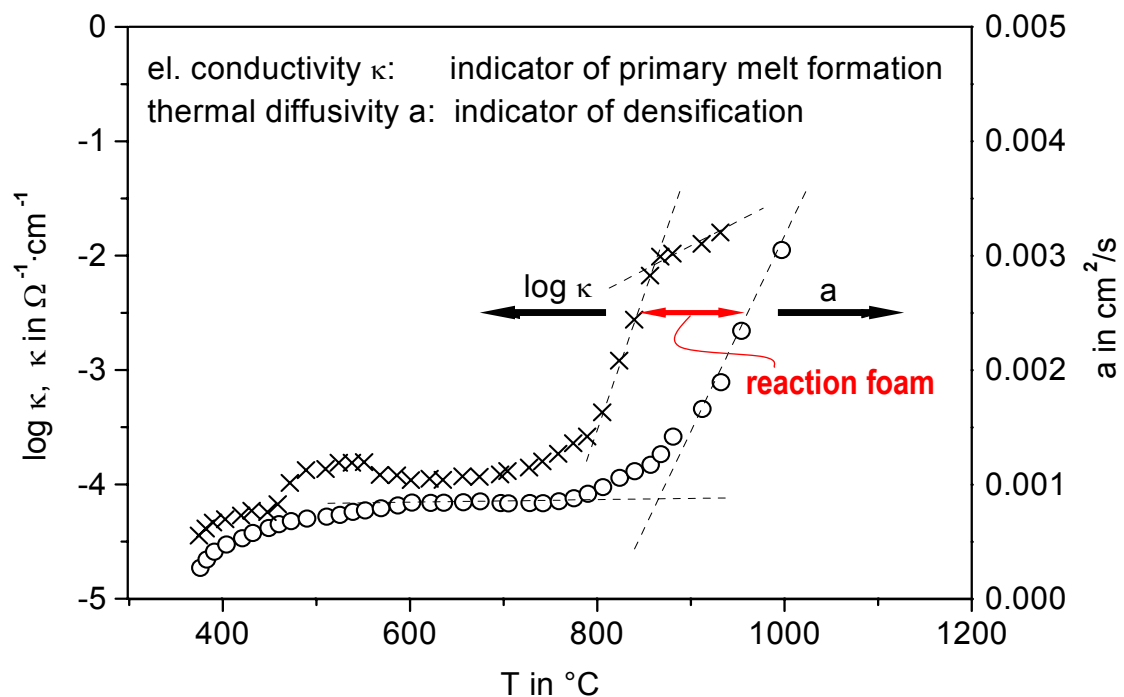


Fig. 17. Electrical conductivities  $\log \kappa$  and thermal diffusivities  $a$  [20]

Unless the batch size is very small, or the batch is percolated by other gases, or melting proceeds in a fluidized state, the reaction atmosphere is that of the reaction gases. Depending on the redox state of the batch, this is essentially a CO/CO<sub>2</sub> mixture. In a reducing batch containing coal, O<sub>2</sub> migration into the batch may play a role, though. These gases can initially freely escape through open pores. When the percolation limit is exceeded with a further increase of the amount of melt, batch porosity becomes closed. If gases still evolve and melt viscosity is high, the material acquires a foamy structure with a volume that can many times exceed its original value. Eventually, the foam collapses, all solid particles – except a significant portion of silica and other grains – are dissolved, and the process enters the stage of rough melt.

### 2.4.3 Effect of minor additions

The lowest temperature at which melt occurs can be reduced by minor additions of fluxes. As a prerequisite, such a minor addition must not form a solid solution with any of the main components. Ginstling and Fradkina [59] describe a scenario at which such a minor addition of melting agent operates. Consider the binary phase diagram of sodium carbonate and an inorganic salt (the melting agent) that does not react with silica. At a constant temperature between the eutectic temperature and the lower melting temperature of either salts, the equilibrium mixture will consist of solid sodium carbonate and a melt containing all the inert salt (present only in a small quantity), saturated with sodium carbonate (point A in figure 18). If silica particles are present, both solid and dissolved sodium carbonate react with silica producing crystalline sodium silicates. At the same time, solid carbonate dissolves in the melt to compensate for the loss from the melt due to reaction with silica. Thus, the melt acts as a mobility bridge between the reaction partners. The overall reaction rate depends on the fraction of the wetted silica surface. The amount and composition of melt remains constant at this stage.

After the solid carbonate disappears, the melt becomes impoverished in carbonate until the point of saturation by the inert salt (point B in figure 18) is reached. Then the melt composition remains constant due to crystallization

of the inert salt. When all carbonate is finally consumed, the mixture consists of un-reacted silica, crystals of the inert salt and crystalline silicates.

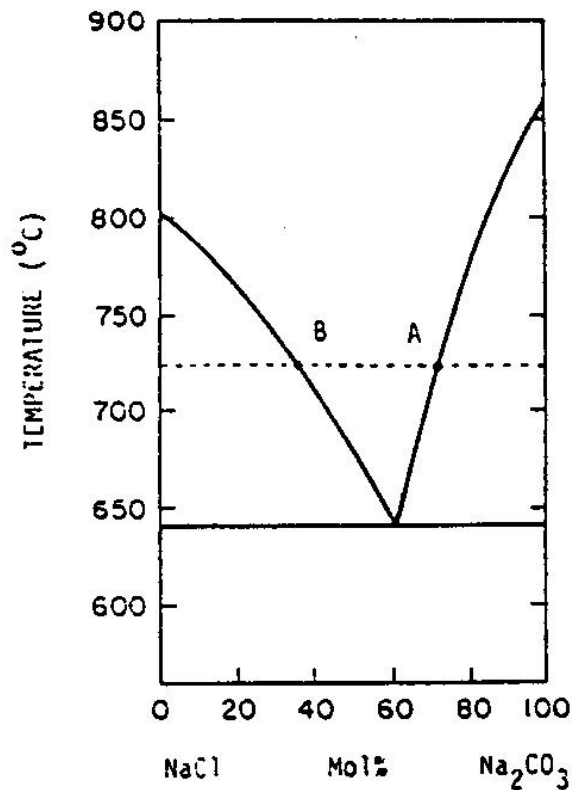


Fig. 18. NaCl-Na<sub>2</sub>CO<sub>3</sub> phase diagram

The rate-controlling process is most likely diffusion of sodium carbonate through the melt. Very little is known about the spatial configuration of melt, silica grains and different crystalline phases during the process. It is certainly a dynamic situation, because evolving carbon dioxide continuously disturbs the mixture.

Thomasson and Wilburn [2] showed by thermal analysis (heating rate 10 K/min) that if the sodium carbonate-silica batch (with 150-200  $\mu\text{m}$  grains of both components) contained 2 mol % NaCl, the temperature of the maximum mass loss rate decreased by 55 K (from 845°C without additions, see figure 19).

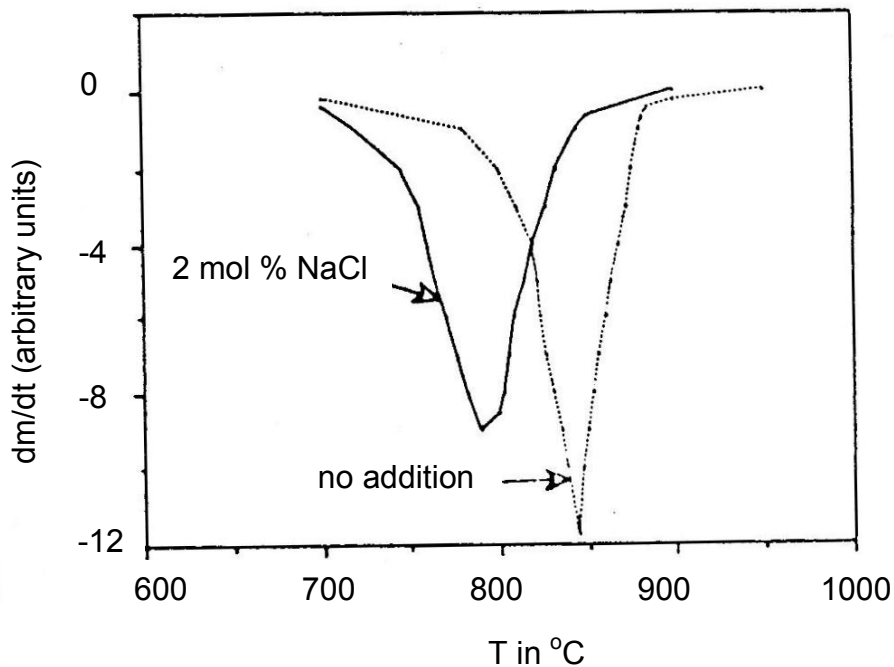


Fig. 19. Rate of mass change against temperature for quartz-sodium carbonate mixture (15 %  $\text{NaCO}_3$ , both materials of grain size 150-200  $\mu\text{m}$ ; heating rate 10 K/min) with and without addition of NaCl

If NaF was used, the temperature drop was 85 K. In a batch with less than 50  $\mu\text{m}$  grains, the drop (from 790 °C without additives) was even larger: 135 K in the case of NaCl and 90 K in the case of NaF. The reversal of order of the effects of NaCl and NaF on batch with fine and coarse silica cannot be taken too literally; the reproducibility of TGA results was not reported by the authors.

Of course, in view of emission control, one would hesitate to recommend the use of NaCl or NaF as a melting accelerant. Nevertheless, it is the principle of acceleration which is stressed in the given example.

Another important issue, which however cannot be covered by the present thesis, is the potential segregation of the batch due to the simultaneous presence of granular solids, low and high liquidus melts.

## Chapter 3

### Experiments

#### 3.1 Preparation of materials; investigated systems

##### 3.1.1 Characterization of raw materials

All raw materials used during the study are industrial glass grade materials. Most of them were provided by Nienburg GmbH (nowadays: Rexam Glass). Sand was also provided by Quarzwerke Frechen (see chemical compositions in table 4).

Table 4. Chemical analysis of raw materials used in the study

raw materials	SiO <sub>2</sub>	Al <sub>2</sub> O <sub>3</sub>	Fe <sub>2</sub> O <sub>3</sub>	CaO	MgO	Na <sub>2</sub> O	K <sub>2</sub> O
sand	99.5	0.14	<0.05	<0.1	<0.05	<0.1	<0.02
sand(QW*)	99.8	0.11	0.03	-	-	-	-
limestone	2.1	0.72	0.28	53.4	0.65	<0.1	0.21
dolomite	1.4	0.45	0.46	31.5	20.11	0.1	0.03
phonolite	60.8	18.98	2.53	0.9	0.26	7.2	5.53

\* Quarzwerke Frechen



### 3.1.2 Preparation of grain size fractions

Different fractions of sand and cullet were prepared by dry sieving.

Table 5. Size fractions of sand

raw materials	size fractions in $\mu\text{m}$			
sand	355-500	250-355	180-250	125-250

### 3.1.3 Glass batch compositions

Six glass compositions were used for small scale tests (200 g) throughout this work. However, not all were selected for every investigation. Soda lime silicate glass corresponded to 74 wt. %  $\text{SiO}_2$ , 10 wt. %  $\text{CaO}$ , and 16 wt. %  $\text{Na}_2\text{O}$ . Its composition was adjusted to a redox number -13 by an appropriate sulfate to coal balance. Tables 6 and 7 show batches and oxide compositions used in this work.

### 3.1.4 Investigated systems

Tables 8 and 9 give an overview over the small-scale experiments on 200 g batches. One-component, binary, ternary, and multi-component raw material mixtures were investigated by using the electrical conductivity sensor. These tests not only proved the accuracy of the measuring system, but also yielded results for the fundamental understanding of the batch melting process. Further tests focused on the duration of the “reaction foam period”, which is depicted as a term to describe the intermittent stage between granular bulk solid and rough melt, and on the thermal diffusivity measurement. In the later tests, silica sand was used to calibrate the system.

Table 6. Composition of the batches in g/100 g glass

raw materials	70-10-16	container flint 1	container flint 2	container green	container amber	crystal	lead
sand	74.00	67.97	67.84	64.00	67.63	56.82	55.67
feldspar		7.66					
phonolite			6.71	10.99	6.69		
dolomite			14.38	10.35	14.33		
limestone	17.84	23.80	10.07	12.93	9.97		
soda ash	25.15	17.67	19.18	20.13	19.22	3.87	
potash						20.70	22.65
BaCO <sub>3</sub>						0.84	
borax unhydr.						0.38	
PbO						25.22	
Pb <sub>2</sub> O <sub>3</sub> *)							28.49
Cr <sub>2</sub> O <sub>3</sub>				0.43			
Fe <sub>2</sub> O <sub>3</sub>				0.14			
sulfate	2.96	0.71	0.72		1.37		
coal	0.37				0.18		
NaNO <sub>3</sub>			0.96				
KNO <sub>3</sub>						1.16	1.31
As <sub>2</sub> O <sub>3</sub>						0.22	
Sb <sub>2</sub> O <sub>3</sub>						0.11	0.82
sum batch	120.32	117.81	119.86	118.97	119.39	109.32	108.94
sum glass	100.00	100.00	100.00	100.00	100.00	100.00	100.00

\*)  $\frac{1}{2}$  Pb<sub>3</sub>O<sub>4</sub> +  $\frac{1}{2}$  PbO<sub>2</sub>

Table 7. Overview over the small-scale tests on thermal diffusivity

components	raw materials	ratios	grain size variation
one component	sand		sand
multi	soda lime silicate glass	*)	no
	container green	*)	no
	container flint 2	*)	no
	crystal glass	*)	no

\*) batches, see table 6

In multi-component systems, standard tests were performed in air, except glass 74-10-16. With this glass, additional tests with different coal additions (0.5 and 2 wt. %), and atmospheres (flow air at 10 l/h, CO<sub>2</sub> at 10 l/h, and H<sub>2</sub>O:N<sub>2</sub> (50:50) at 56 l/h) were also performed.

Table 8. Overview over the small-scale tests on electrical conductivity

components	raw materials	ratios	grain size variation
single	soda ash		-
	sand		-
	limestone		-
	dolomite		-
	phonolite		-
binary	soda ash + sand	1:1, 1:1.5, 2:3, 4:1, 9:1	-
	soda ash + sand	1:1	varied
	soda ash + limestone	1:1	-
	soda ash + dolomite	1:1	-
	soda ash + phonolite	1:1	-
ternary	soda ash + sand + limestone	1:1:1	-
	soda ash + sand + dolomite	1:1:1	-
	soda ash + sand + phonolite	1:1:1	-
multi	74-10-16	*)	-
	container green	*)	-
	container flint 2	*)	-
	crystal glass	*)	-
	lead glass	*)	-

\*) batches, see table 6

### 3.1.5 Preparation of melting crucibles

The crucibles used in the tests were made in-house. Two types of compositions for low and high temperature application (1300, and 1600 °C) were chosen as shown in table 10. Different shapes of crucibles were made. For the electrical conductivity and batch free time test (BFT), 70 mm wide and 80-100 mm high crucibles were used (fig 20 a). For the mass loss tests; two different designs, a closed and open one were used (fig 20 b-c). Before mixing, raw materials were ground in a porcelain dish and passed through a sieve, then mixed in a ball mill for 3 h for low temperature and 24 h for high temperature crucibles. After that, a slip was prepared and cast into plaster molds (plaster of Paris at a gypsum to water ratio of 70 wt. %). The objects were dried in air for 2 days and in an oven for 24 h at 120 °C, then biscuit fired at 950 °C and sintered at 1200 °C, or 1700 °C, respectively.

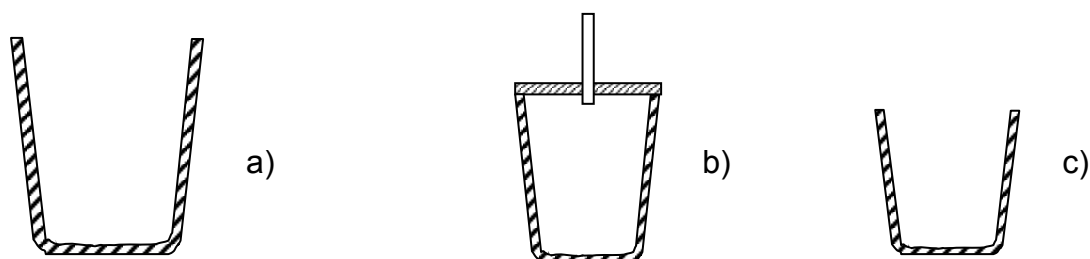


Fig. 20. Sketch of crucibles

Table 9. Composition of crucibles as prepared for low and high temperature (T) application

raw materials	compositions in wt. %	
	low T	high T
CaCO <sub>3</sub>	-	2
talcum powder	-	4
kaolin	20	-
ball clay	40	4
alumina	40	90

## 3.2 Methods of investigation

Methods frequently used in the investigation of batch melting are differential thermal analysis (DTA), differential thermogravimetry (DTG) – often combined with a mass spectrometer for the analysis of evolving gases –, differential scanning calorimetry (DSC), and hot-stage X-ray diffraction analysis. These are very accurate methods providing deep insights into the course of thermochemical reactions. When it comes to the investigation of batch melting, however, the small sample sizes involved in all of these methods (typically 250 mg) are a severe limitation. The methods under discussion work best with well-mixed fine powders. But this is a very unusual situation for industrial glass batches. In such batches, large mass fractions of grains bigger than 0.5 mm are found. Samples of 250 mg taken from such batches have very little chance of being representative. Even worse, the strong influence of grain-to-wall contact in the tiny sample compartments yields effects which never occur in a large scale situation, hence, must be considered as experimental artifacts.

In view of this situation, a major part of research efforts was devoted to the further development of new experimental methods suitable for the investigation of batch melting, which are:

- conductometry on 200 g batches,
- measurements of local thermal diffusivities in 200 g batches by a heat,
  - pulse run time sensor,
- mass loss from 200 g batches.

The methods were supplemented by batch free time tests and by heating microscopy. For the latter method, a new way of experimentation was developed, too.

### 3.2.1 Conductometry

#### a) Research furnace

An electrical furnace as shown in figure 21 was used. It was constructed by a light weight alumina brick and used silicon carbide as heating elements. A digital temperature controller was used to control the furnace temperature to a maximum temperature of 1200 °C with heating rates from 1 to 30 K/min. The furnace could be flushed with different atmospheres. The data were recorded by a computer bus and stored.

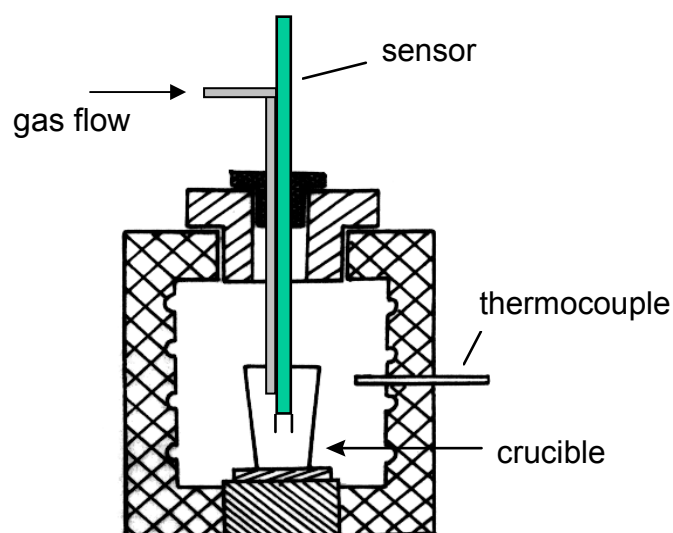


Fig. 21. Sketch of the small study furnace

#### b) Thermocouples and sensors

Two different types of sensors were used. These are: a solenoid type sensor as shown in figure 22 (for the standard tests) and a double cylinder platinum sensor for an exact determination of the electrical conductivity (in lead glass only) as explained in figure 23. The resistivity of the material was determined by the voltage drop across the sensor by a circuit as shown in figure 22. The voltage  $U_0$  was selected as 2 to 3 V AC, 50 or 1000 Hz, respectively. Thus, with  $U_0$  known,  $R_x$  is readily calculated. The probe was

connected to a circuit as shown in figure 22. With  $C_{\text{cell}}$  in  $\text{cm}^{-1}$  as the cell constant of the sensor, the conductivity  $\kappa$  in  $(\text{ohm}\cdot\text{cm})^{-1}$  is derived as

$$\kappa = \frac{C_{\text{cell}}}{R_x} \quad \text{with } C \approx 1 \text{ cm}^{-1}. \quad (3.1)$$

By fundamental laws of electrical circuits, the following equations hold

$$\frac{1}{R_y} = \frac{1}{R_1} + \frac{1}{R_x}, \quad (3.2)$$

$$\frac{U_x}{R_y} = \frac{U_0}{R_1 + R_x}, \quad (3.3)$$

$$R_y = \frac{R_1 \cdot R_x}{R_1 + R_x}. \quad (3.4)$$

Thus the  $U_x$  value read by the voltmeter can be converted into  $R_x$ ,

$$R_x = \frac{U_x (R_1 + R_x)^2}{U_0 R_1} \quad (3.5)$$

and

$$\kappa = \frac{C_{\text{cell}} \cdot U_0 \cdot R_1}{U_x \cdot (R_1 + R_x)^2}. \quad (3.6)$$

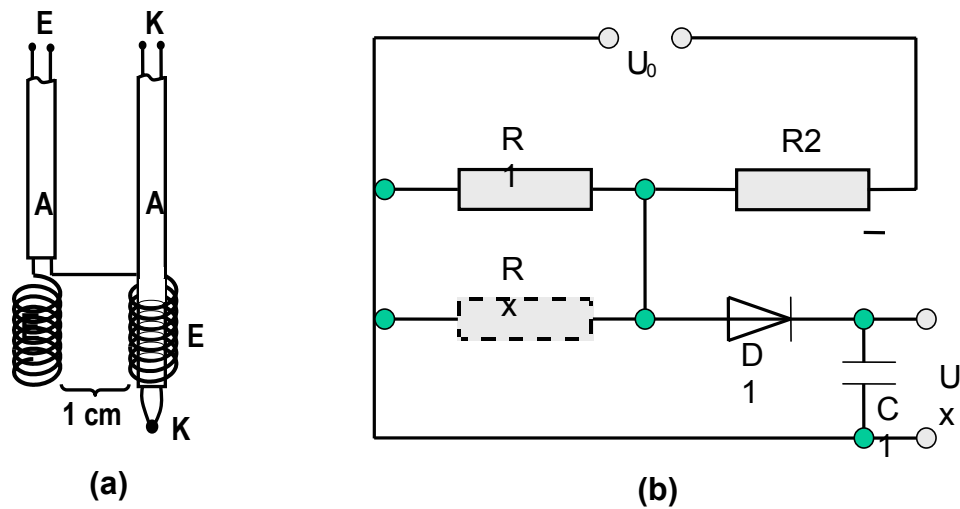


Fig. 22. Sketch of the temperature-resistivity sensor (a) and of the electrical circuit (b) used to measure the voltage drop across the batch; E: electrode; A: alumina tube; K: NiCr-Ni thermocouple (type K);  $R_1 = 1 \text{ M}\Omega$ ;  $R_2 = 10 \text{ k}\Omega$ ;  $U_0 = 3 \text{ V AC}$ ,  $R_x$  represents the resistivity across 1 cm of batch

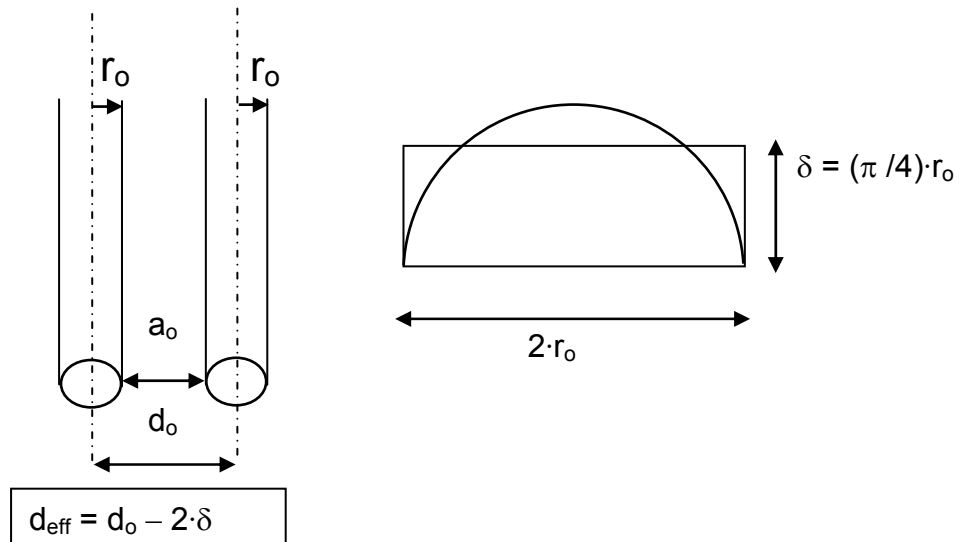


Fig. 23. Sketch of the double cylinder sensor (made of Pt);  $r_0 = 0.35 \text{ cm}$ ,  $d_0 = 1.65 \text{ cm}$ , the sketch at the right hand side illustrates how the effective distance  $d_{\text{eff}}$  between the electrodes is approximated ( $d_{\text{eff}} \approx 1.10 \text{ cm}$ ).



The double cylinder platinum sensor illustrated in figure 23 was used to determine an exact electrical conductivities of lead glass, which is meant to provide information for electrically heated furnaces. For this type of sensor, the cell constant is estimated to approx.  $1 \text{ cm}^{-1}$ , which is sufficient for the interpretation of the results.

In additional tests,  $R_x$  was determined by a zero current bridge (see figure 24). For the isothermal experiments, Pt sensors were used. In some of the non-isothermal tests, NiCr sensors were employed. In order to continue the measurement beyond the melting onset, the circuit as shown in figure 24 was modified in that different values of the resistor  $R_2$  could be chosen. The electrical conductivity is given by

$$\kappa = C_{cell} \cdot \left[ \left( \frac{U_o}{U_x} - 1 \right) \cdot \frac{1}{R_2} - \frac{1}{R_1} \right] \quad (3.7)$$

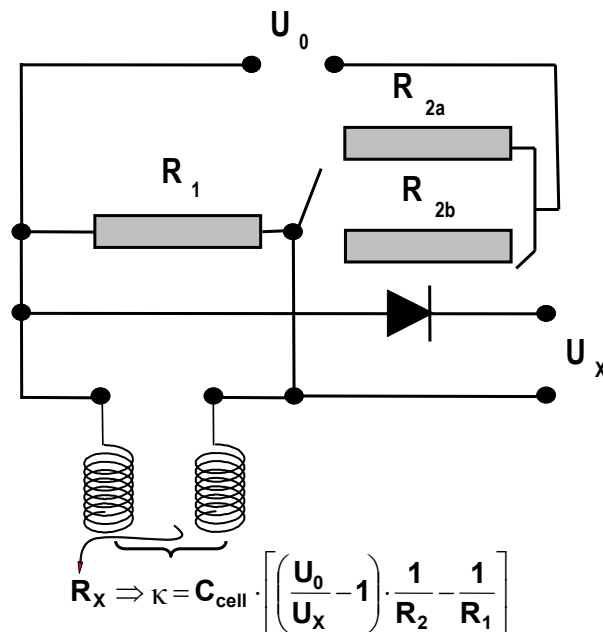


Fig. 24. Modified electrical circuit with  $U_o = 3V \text{ AC}$ ,  $R_1 = 1 \text{ M}\Omega$ ,  $R_{2a} = 10 \text{ k}\Omega$ ,  $R_{2b}$  adjustable between 100 and 1000  $\Omega$

### c) Sample preparation

The 200 g samples were loaded into a commercial crucible and exposed to the small study furnace. The resistivity and temperature probes were placed in the middle of the crucible. The immersion depth was approx. 4 cm in the batch. The probes were connected to a computer which recorded both the voltage  $U_x$  and the thermovoltages of the thermocouples placed in the furnace, respectively. The signals were read in intervals of 1s. The furnace space was flushed with CO<sub>2</sub> at 10 l/h.

## 3.2.2 Thermal diffusivity

### a) Thermal diffusivity sensors

In glass melting the superficially fusing batch is a heat sink. Earlier calculations for batches composed of raw materials showed that the thermal conductivity  $\lambda^*$  of the batch only has a small influence on the time needed for the batch melting. This statement is not valid for batches containing high ratios of cullet. Additions of cullet to the batch do not only decrease the chemical fraction of the heat demand, over a threshold value of 40 percent they increasingly influence the thermal diffusivity and enhance the heat flux into the batch. In the following, a sensor is described by which the local thermal diffusivity can be measured. The thermal diffusivity  $a$  is related to the heat conductivity  $\lambda$  by

$$\mathbf{a} = \frac{\lambda^*}{c_p \cdot \rho} \quad (3.8)$$

where  $\rho$  is the bulk density in g/m<sup>3</sup> and  $c_p$  is the specific heat capacity in J/(g·K).

Without a sensor as described below, the thermal diffusivity of batches has to be determined from the temporal and local derivative of the measured

temperature field in the batch using Fourier's law. This is a very imprecise method, because chemical reactions distort the temperature field during the whole melting process. To develop a new measuring concept of thermal diffusivity, a similar measuring system as the conductivity sensor was applied. This new type of sensor was equipped with a heat source. A heating coil was made by a 0.2 mm thick Ni wire connected to a 1 mm thick Kanthal wire. The Kanthal wire was connected to a voltage source (10 V AC) triggered by a computer bus, generating a 10 s heat pulse every 150 seconds. The thermal diffusivity was determined by evaluating the run time of the heat pulses (< 5 K temperature difference at the receptor thermocouple) across a distance of 1 cm. The method and its evaluation are explained in [60]. Meanwhile, it has been further improved by my colleagues, and used in their research [64, 70]. Special reference is made to the thorough mathematical treatment by [64]. The expected precision is approximately  $\pm 5 \cdot 10^{-4} \text{ cm}^2/\text{s}$ . Figure 25 shows a prototype of the sensor. In figure 26, an additional thermocouple was directly attached to the heating coil.

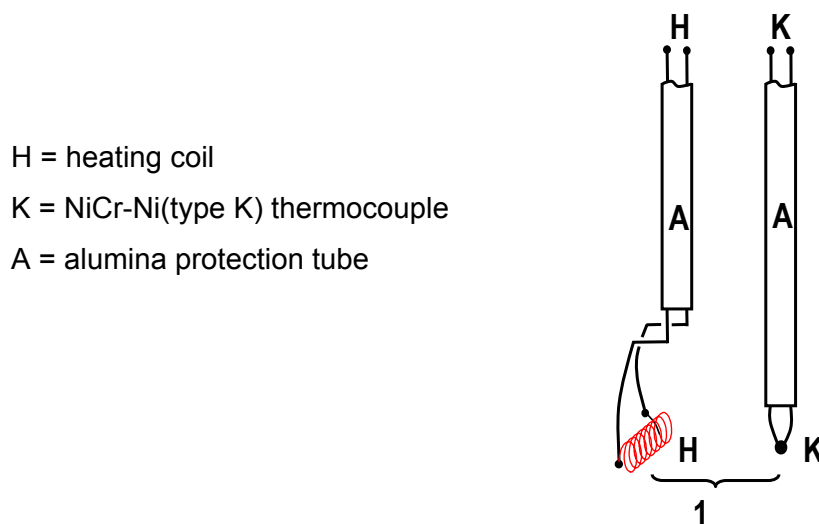


Fig. 25. Sketch of the sensor for thermal diffusivity measurement [60]

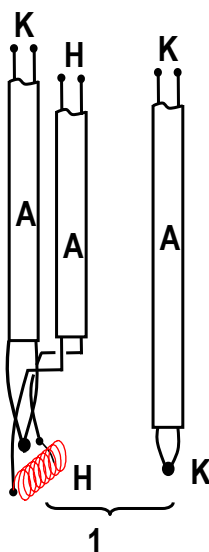


Fig. 26. Thermal diffusivity sensor, modified version

### b) Sample preparation

The samples (200 g) were loaded into a commercial crucible and exposed to the small study furnace. The thermal diffusivity and temperature probes were placed in the middle of the crucible. The immersion depth was approx. 4 cm in the batch. The probes were connected to a computer which recorded the duration of the heat pulses, and the temperatures received by the sensor, and the temperature of the furnace, in time intervals of 1 s.

## 3.2.3 Heating microscopy

### a) Conventional use

The softening behavior of glass batches was studied by heating microscope. For this purpose, samples were ground to a particle size  $< 63 \mu\text{m}$  and 5-10 mg were hand pressed into pellets of 2 mm diameter and height 3-4 mm. Each sample was then placed on an alumina sample holder, which was covered by a thin platinum foil and was put into the heating microscope, Leitz type II A (figure 27). The measurement was performed under  $\text{CO}_2$  atmosphere up to  $1400 \text{ }^\circ\text{C}$  at a rate of  $10 \text{ K/min}$ . According to DIN 51730, the

characteristic temperatures, start of visible gas release (T1), round edge point (T2), and half sphere point (T3), were observed as can be seen in figure 28.

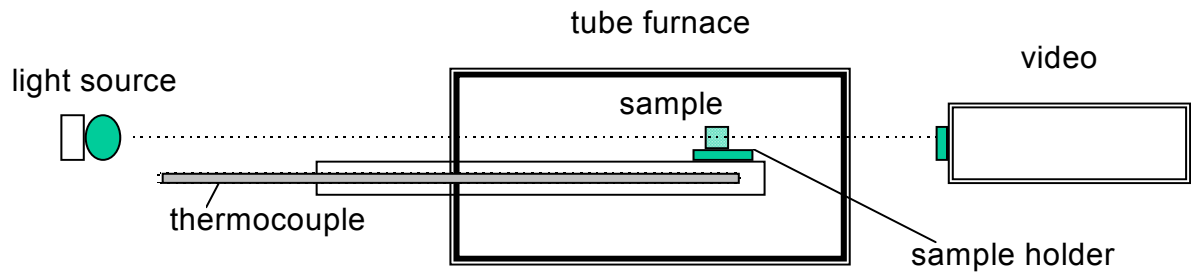


Fig. 27. Sketch of the heating microscope

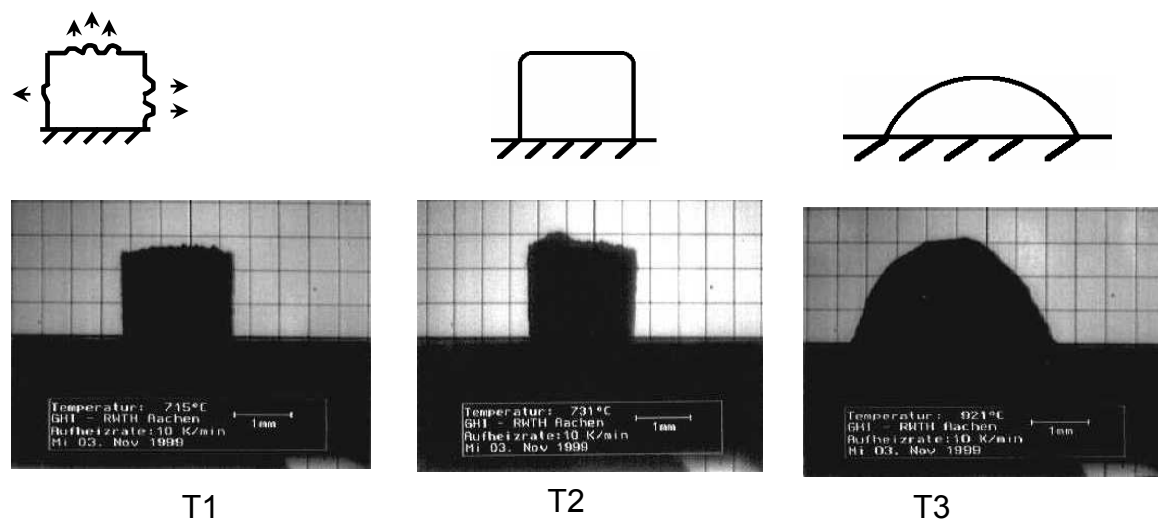


Fig. 28. Three characteristic temperatures T1: start of visible gas release; T2: round edge point; T3: half sphere point [61]

### b) Alternative use

In order to study the grain-to-grain reactions, small piece of raw materials (single test) were placed on alumina sample holder covered with Pt foil. For binary and ternary components tests, each material was placed by edge to edge contact similar to the procedure described in [12] (see the

investigated system in table 8). The measurement was performed at the same condition as described before.

For studying the progress of gas release, the experiment was focused only on soda lime silicate (74-10-16) glass batches with small additions of 1 wt. % NaCl, NaNO<sub>3</sub>, and NaOH. The sample was weighed before and after testing within an accuracy of 0.00001 mg. All tests were performed at the same condition of heating rate 10 K/min to 1400 °C, no soaking time, CO<sub>2</sub> atmosphere 10 l/h, and rapidly cooled down to room temperature within 30 min. After testing, the residues of quartz and bubbles were observed by optical light microscope. The progress of gas release was calculated as

$$\text{progress of gas release} = \frac{\Delta m_1(\text{gas, real})}{\Delta m_2(\text{gas, total})} \times 100 \quad , \quad (3.9)$$

where  $\Delta m_1(\text{gas, real})$  is the mass loss of gas determined from heating microscope (manually weighed before and after the tests), and  $\Delta m_2(\text{gas, total})$  is the theoretical mass loss determined from batch calculation.

### 3.2.4 Batch free time (BFT) experiments

In this investigation, different types of furnace were used. The design of the batch free time experiments at GHI is shown in figure 29 a and the furnace at SCHOTT Co. is shown in figure 29 b.

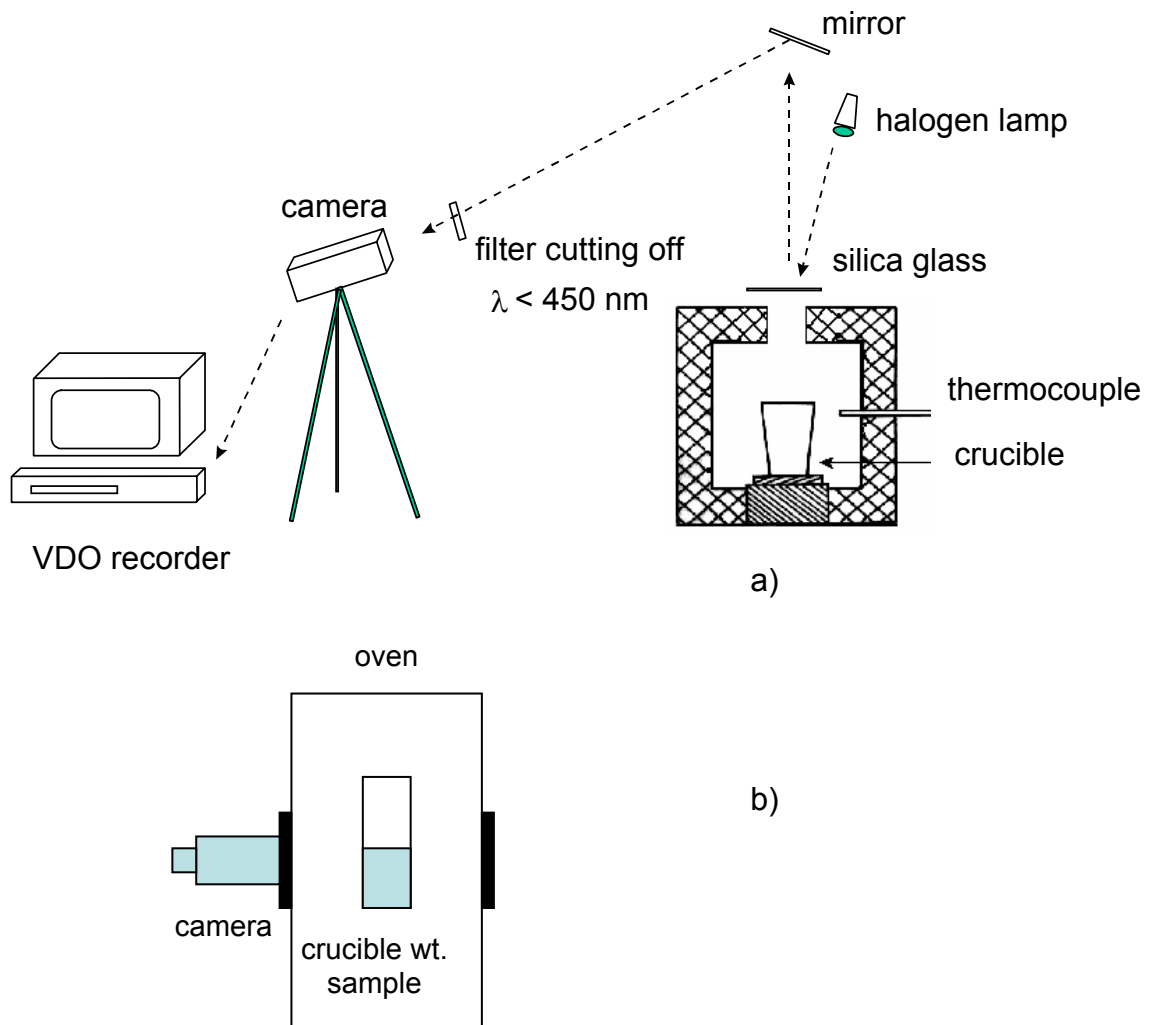


Fig. 29. Design of the batch free time experiment at GHI a), and at SCHOTT Co. b)

In evaluating the batch free time experiments thus performed, a procedure differing from the one originally suggested by [21-22] was used, since there was no objective criterion to decide when “the batch had disappeared under the melt level by more than 99 wt. %”. The crucibles were firstly loaded with 150 g of cullet, preheated to 900 °C in an electrical furnace, and raised to  $1400 \pm 10 \text{ °C}$ . Then, 86 g of batch was quickly charged on top of the established cullet melt in the crucible. Different tests were performed which were interrupted after 10, 20, 30 minutes, respectively. Within the scope of the present study, five different batches were investigated (see compositions in table 11 and 12), which were:

- S1: a crystal glass,
- S2: a container flint 1 glass,
- S3: a sodium silicate glass (Na:Si = 2.05),
- S4: a sodium silicate glass (Na:Si = 3.3), and
- S5: a sodium silicate glass (Na:Si = 3.4).

All five compositions were sent by an industrial partner in two forms as mixed batches and cullet. The cullet had the same compositions as the glass expected from the mixed batch. Cullet were used only for the batch free time study. Time durations of 10, 20, and 30 min were chosen with crystal glass (S1). For sodium silicate glasses; S3, S4, and S5, the test duration was 50 and 80 min. For container flint 1 glass S2, the time was additionally extended to 100 min. The melting of the batch was recorded by a video camera. After testing, the crucibles were extracted from the hot furnace and annealed for 2 h. After that, the samples were vertically cut and visually evaluated. The residual crystalline phases were inspected by light microscope from slices with 1.5 mm thickness.



Table 10. Composition of the batches used in studying batch-free time; in g per 100 g glass

raw materials	S1	S2	S3	S4	S5
sand	56.61	67.97	66.53	76.19	76.72
feldspar		7.66			
limestone		23.80			
soda ash	3.81	17.67	57.24	40.72	39.80
potash	20.63				
BaCO <sub>3</sub>	0.84				
PbO	25.12				
borax unhydr.	0.38				
sulfate		0.71			
KNO <sub>3</sub>	1.15				
As <sub>2</sub> O <sub>3</sub>	0.23				
Sb <sub>2</sub> O <sub>3</sub>	0.12				
sum batch	108.54	117.81	123.77	116.91	116.52
sum glass	100.00	100.00	100.00	100.00	100.00

Table 11. Nominal oxide composition of glasses S1 to S5 after table 10 in wt. %

	S1	S2	S3	S4	S5
SiO <sub>2</sub>	56.61	73.53	66.53	76.19	76.72
Al <sub>2</sub> O <sub>3</sub>		1.49	33.47	23.81	23.28
B <sub>2</sub> O <sub>3</sub>	0.26				
CaO		13.39			
BaO	0.66				
PbO	25.12				
Na <sub>2</sub> O	2.38	11.59			
K <sub>2</sub> O	14.61				
As <sub>2</sub> O <sub>3</sub>	0.23				
Sb <sub>2</sub> O <sub>3</sub>	0.13				
sum	100.00	100.00	100.00	100.00	100.00

### 3.2.5 Mass loss measurements (50 g scale)

The conventional methods to determine mass loss of materials as a function of temperature is thermal gravimetry analysis (TGA), however, within a limit of typically 250 mg only. This amount of sample range has very little chance of being representative for the batches, especially in view of the influence of grain sizes. Therefore a new concept of mass loss measurement was designed to determine gas loss during melting. The experimental setup is shown in figure 30. Crucibles as shown in figure 20 b were used. The method did not allow resolving the gas release with respect to time. In an alternative furnace design, the mass loss signal was directly detected on-line from a balance at  $\pm 0.001$  mg.

The sample was heated in a vertical resistance tube-furnace with three heating zones. Each zone was separately controlled with a Eurotherm controller with proportional, integral, and differential (PID) characteristics within  $\pm 1$  K. A schematic diagram of the furnace used is given in figure 31.

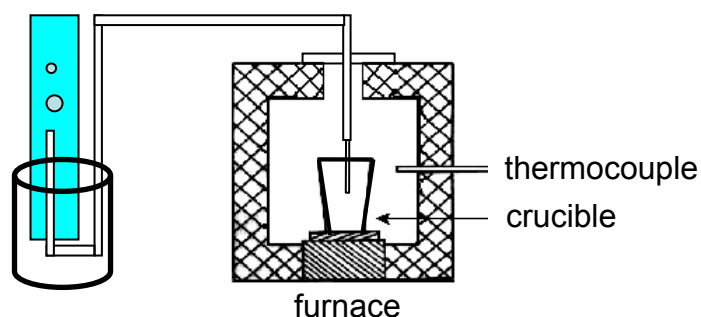


Fig. 30. Design of the gas mass loss determination furnace

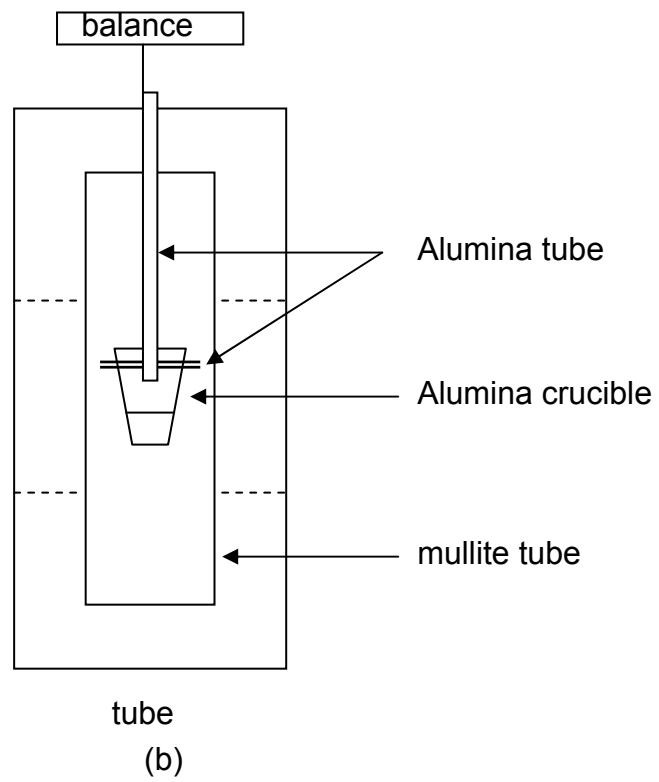


Fig. 31. Sketch of macro thermo balance furnace, designed and tested at GHI

## Chapter 4

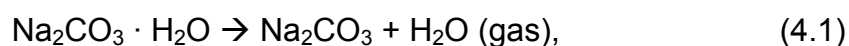
### Results and discussion

#### 4.1 Conductometry

The measuring method of electrical conductivity has been started in 1993 at Chulalongkorn University, Thailand as a part of an ASAHI research foundation sponsored project, with the author being part of the research team [63]. At that time the results could only investigate on some certain systems. In specific, the conductivity could be measured up the onset of melting only. Four years after that the measurement was again conducted at the Institute for Mineral Engineering (GHI), RWTH Aachen, Germany within the frame of a DFG sponsored project with the author being the performing scientist. The accuracy of the measuring system was firstly checked. After this, the method was extended to one-component, binary, ternary, and multi-component systems and to temperatures beyond the onset of melting.

##### 4.1.1 Accuracy of the measurement

Soda ash and sand were firstly used to investigate the accuracy of the measuring system. A good accuracy of the measurement could be seen from the endothermic peak of release crystal water release of soda ash at  $104 \pm 1$  °C as shown in figure 32. The results are interpreted by the reaction



which according to [52] occurs at  $104 \pm 1$  °C. The calculated equilibrium temperature (using data base [51]) confirms the 104 °C. The experimental

set-up from both places (Chulalongkorn University, Bangkok, Thailand, and GHI, RWTH-Aachen) has a high reproducibility. Due to the high humidity of the tropic air in Thailand, the respective peak is more pronounced (higher amount of monohydrate in the soda ash). Further calibration was focused on the melting of soda ash and the quartz inversion point as can be seen in figures 33 and 34. Melting peaks from soda ash at  $855 \pm 5$  °C agree very well with literature value of 859 °C [45]. The quartz inversion at 573 °C also matches well with the literature value. It is again stressed that these data are obtained from 200 g samples with industrial grain sizes. Thus the author can be confident that the 200 g scale tests are not any less accurate than conventional DTA.

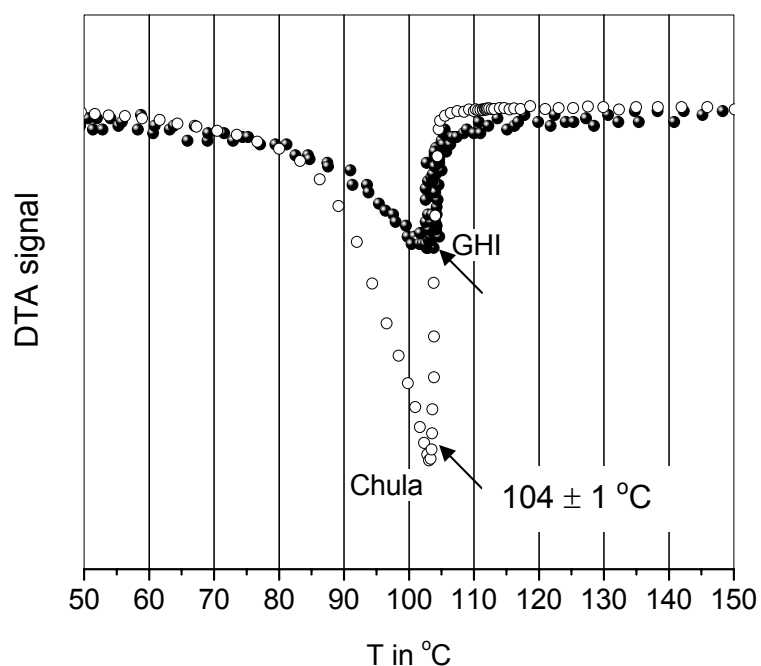


Fig. 32. Crystal water peaks of soda ash tested at Chulalongkorn [63-65] and GHI, RWTH-Aachen University

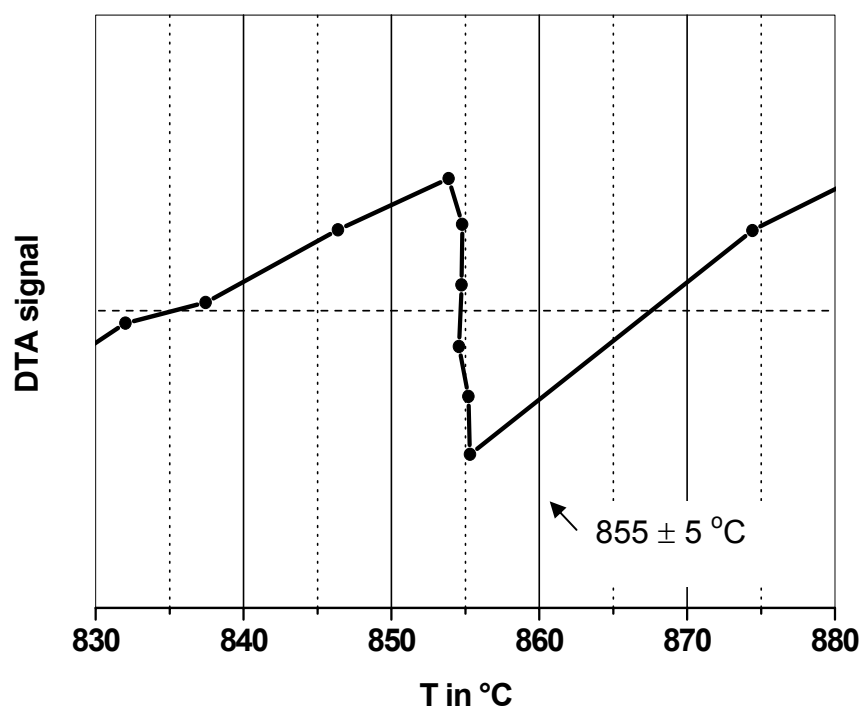


Fig. 33. Melting peak of soda ash at  $855 \pm 5$  °C

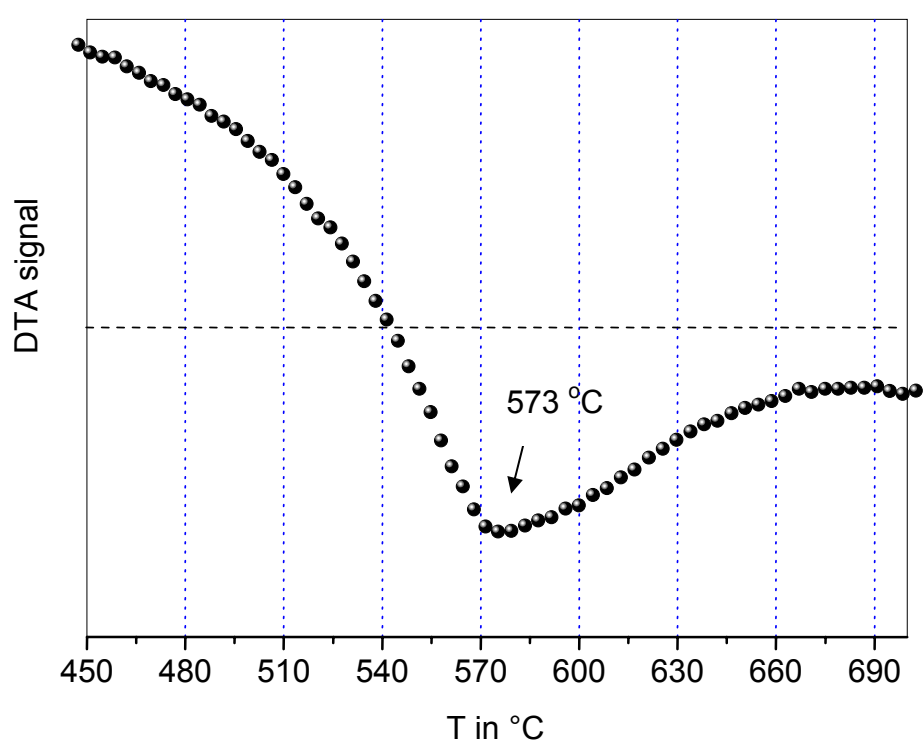


Fig. 34. Plot of DTA signal vs. temperature showing quartz inversion at 573 °C from silica sand

### 4.1.2 Detection of foam formation period

In order to continue measurement beyond the melting onset the circuit was modified as shown in figure 24 and the tests were continued after the ramp heating at constant temperature for 30 minutes. Because of the corrosivity of the primary melts, the Ni-Cr-Ni sensor was replaced by a Pt sensor. A typical result is shown in figure 35. The finding is in perfect agreement with the model by Ungan and Viskanta [37].

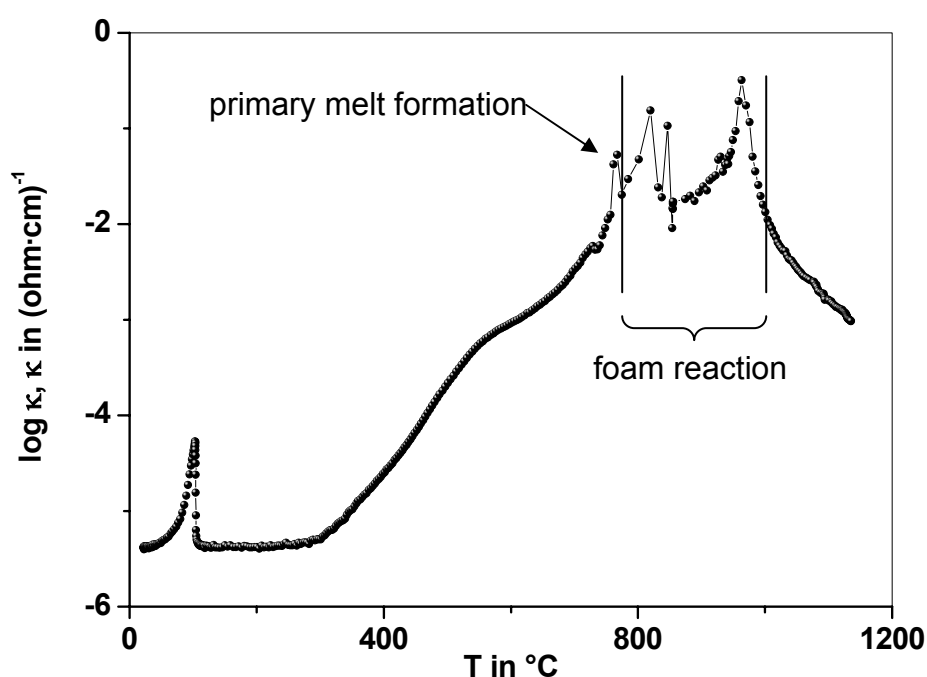


Fig. 35. Plot of soda-sand reaction showing first melt formation and foam forming region

### 4.1.3 Evaluation and presentation of results

After having gained experience with several hundred measurements, it could be concluded that there are three favorable ways to evaluate and present the results of electrical conductivity measurements. The first one is a “DTA” signal. It is the plot of batch temperature as x-axis and the signal calculated from batch temperature minus furnace temperature as y-axis. The second one is the “voltage drop” signal, i.e.; a presentation of the voltage drop

$U_x$  (see figure 36). The signal detected from resistivity probe may be plotted either as a function of batch temperature or of melting time. The last one is the “electrical conductivity” signal. In this case, the calculation of  $\log \kappa$  ( $\kappa$  = electrical conductivity in  $(\text{ohm}\cdot\text{cm})^{-1}$ ) is plotted versus  $1/T$  ( $T$  = temperature in K) or alternatively versus  $T$  in  $^{\circ}\text{C}$ . These three signals are shown in figures 37 a-c.

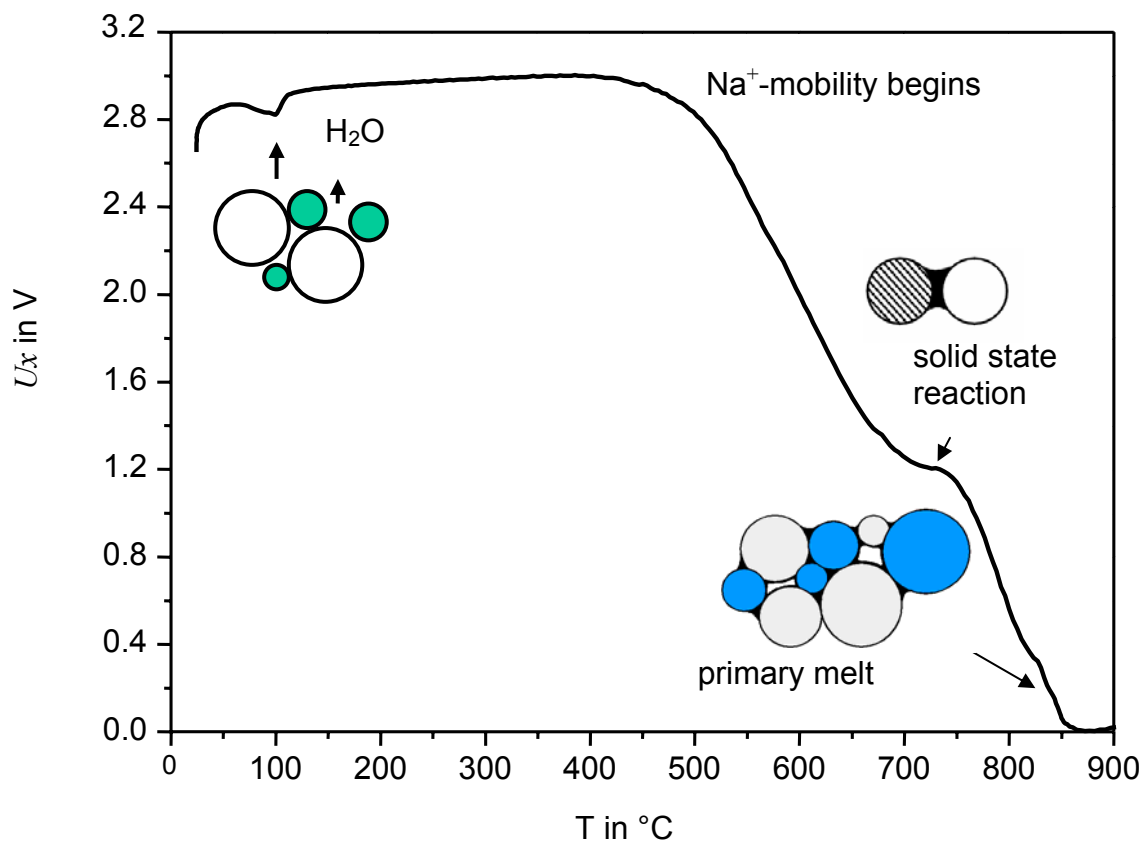


Fig. 36. Illustration of the voltage drop  $U_x$  with  $T$  [66]



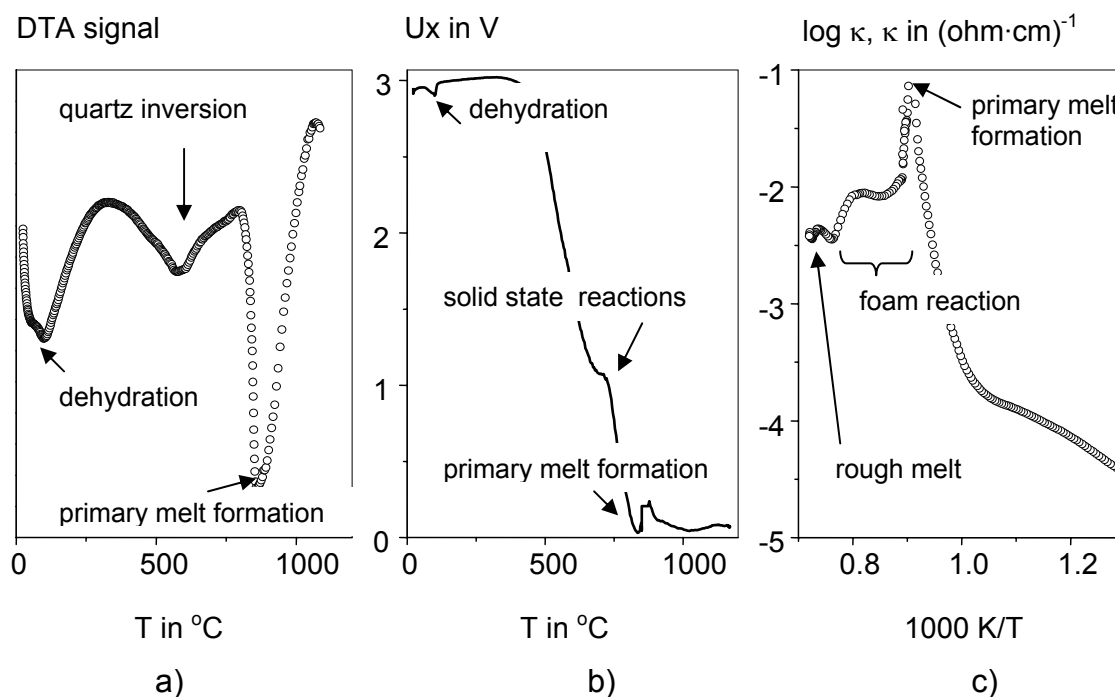


Fig. 37. Illustration of three characteristic signals plot of soda-sand specify reactions between a) DTA signal with T, b) voltage drop with T, and c) electrical conductivity with 1/T

#### 4.1.4 One-component tests

The raw materials; soda ash, sand, limestone, dolomite, and phonolite, which are typically used for glass production were studied. Soda ash and sand were already reported in section 4.1. and will be resumed in 4.1.5. They show a similar electrical conductivity signal as can be seen in figure 38. Most of them have similar value of electrical conductivity approx.  $10^{-4}$ -to- $10^{-5}$  ohm·cm<sup>-1</sup> except phonolite. It shows a higher value of 0.01 ohm·cm<sup>-1</sup> after liquid film formation is formed at temperature above 1200 °C.

#### 4.1.5 Tests on binary mixtures

Four systems with two components; soda-sand, soda-limestone, soda-dolomite, and soda-phonolite were tested.

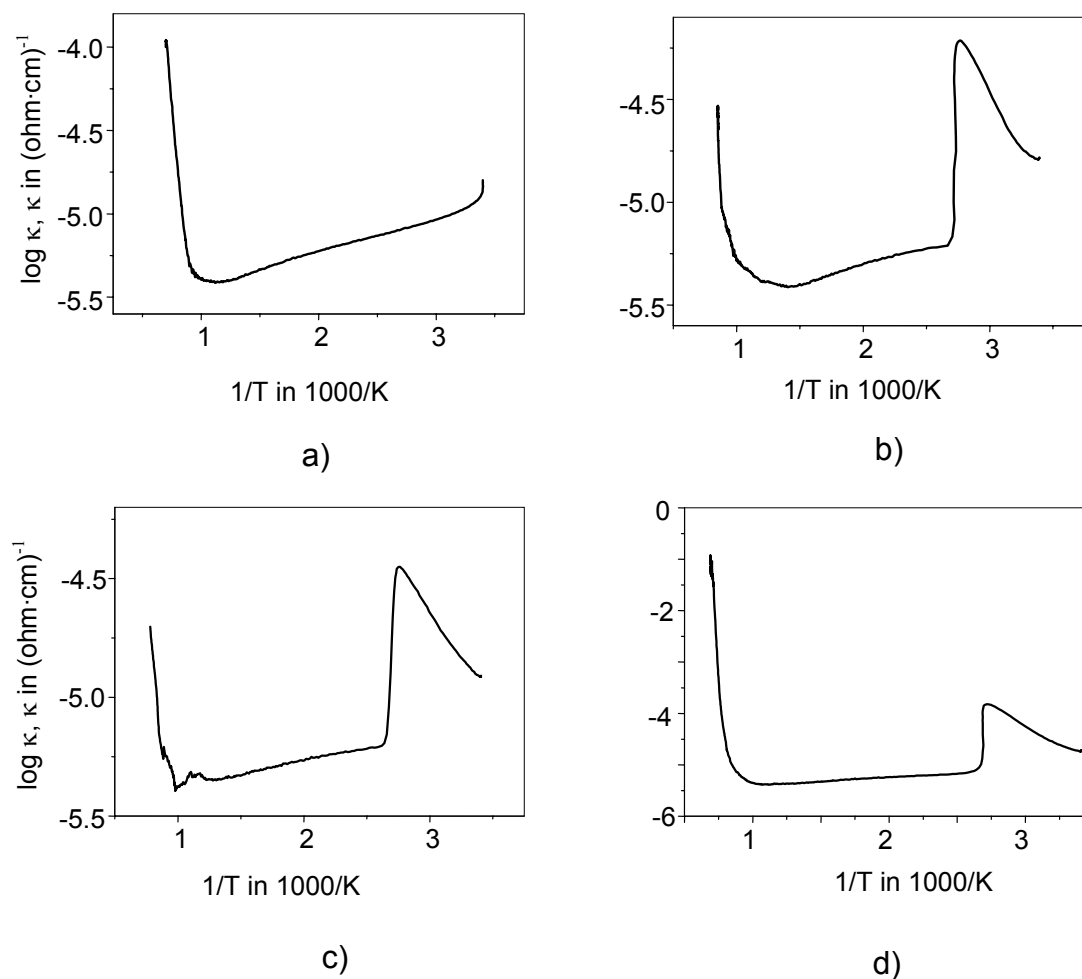
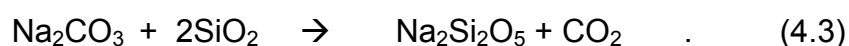
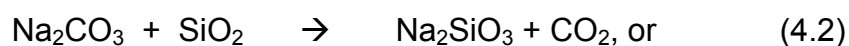


Fig. 38. Plot of electrical conductivity and temperature of a) silica sand, b) limestone, c) dolomite, and d) phonolite

#### a) Soda ash - sand (varied ratio)

Mixed soda-sand shows a strong reaction detected between 800-1000 °C as can be seen from the DTA signal in figure 39, which represent the meta- or di-silicate formations as



(compare the phase diagram in figure 8, page 19).

Comparison between DTA signals from DTA instrument and conductometry measurement mark exactly the same events, however, differ in peak direction and shape, which is due to the higher amount of sample (200 g) was used in conductometry measurement compare to a milligram range used in DTA measurement.

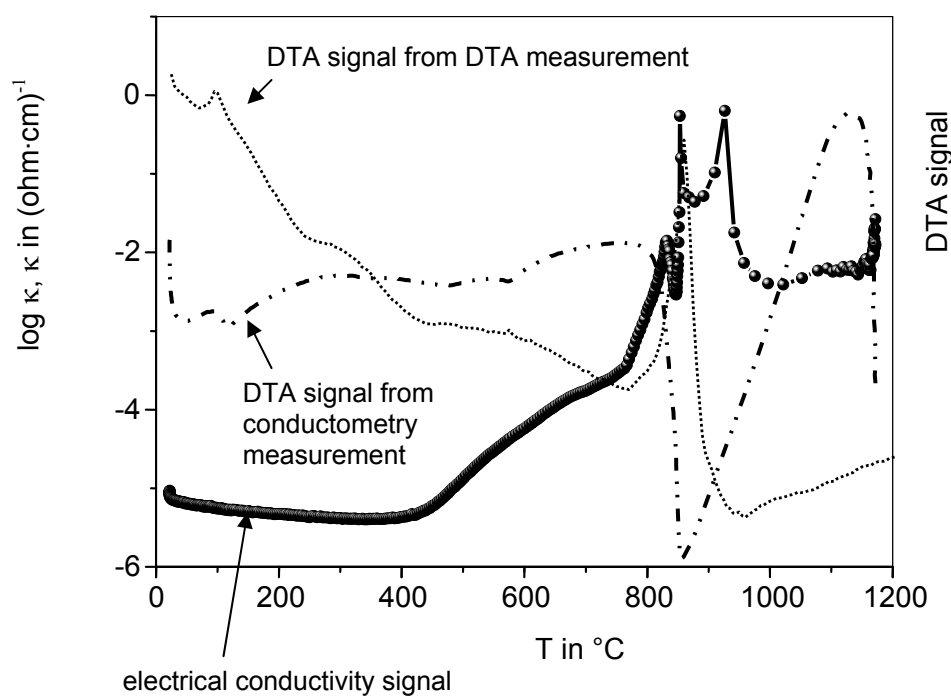


Fig. 39. Plot of DTA and electrical conductivity signals with temperature of soda-sand

Further studies of mixed sand and soda mixtures at different ratios of 50:50, 60:40, 70:30, 80:20 and 90:10 were also performed as shown in figure 40 a. The voltage drop begins at high temperature for low soda content and decrease dramatically with increasing of soda content. This voltage drop signal represents an effect of the motivation from  $\text{Na}^+$  ion. At above 30 wt. % soda ash, a grain to grain contact reaction occurred. Figure 40 b shows the plot of electrical conductivity with  $1/T$  of mixed sand-soda at different ratios of 10:90 to 90:10. Similar effect as voltage drop signals was observed. Electrical conductivity start to increases at high temperature for less soda content and increase dramatically at lower temperature with increasing of soda content.

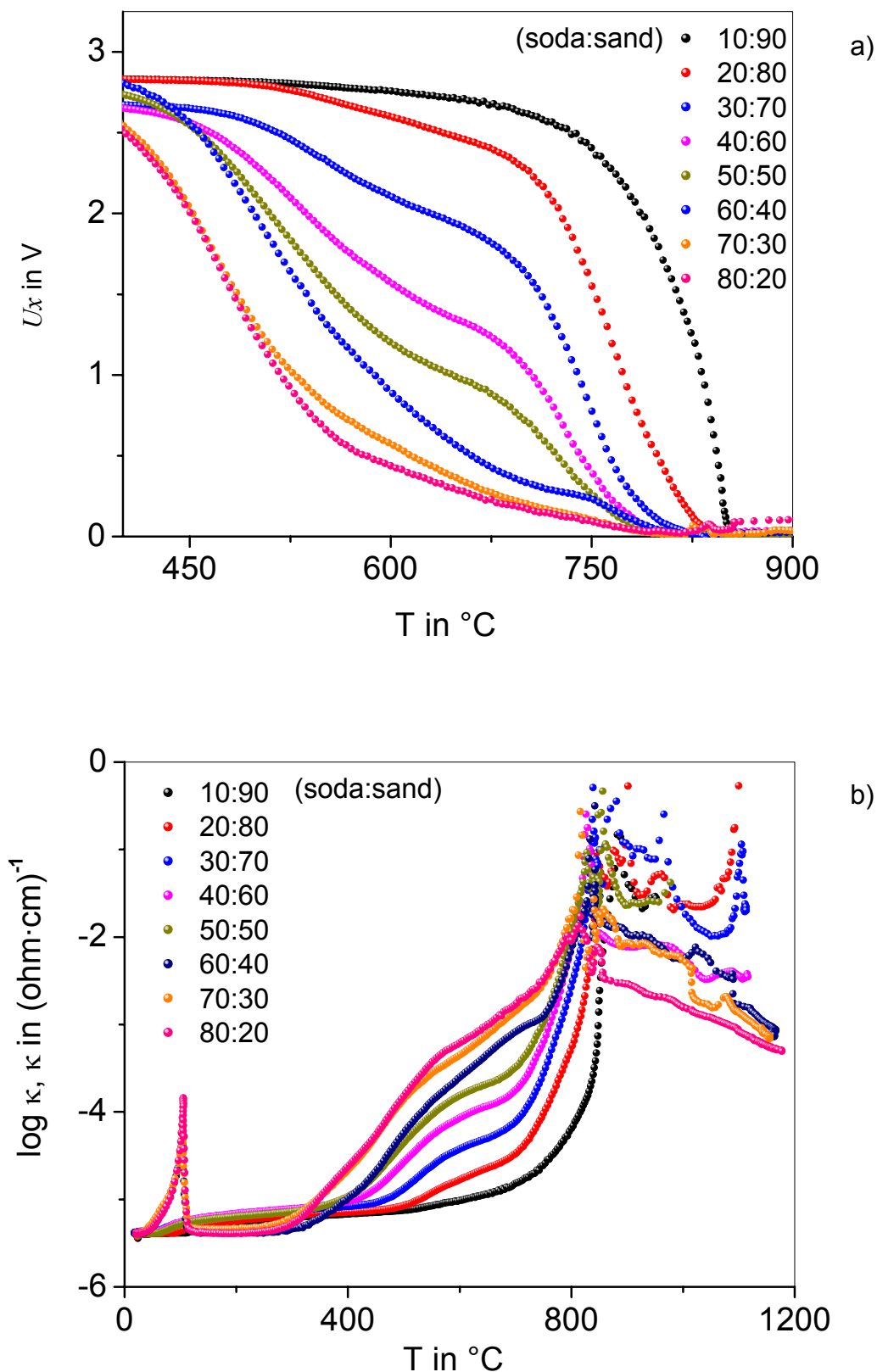


Fig. 40. Variation of the composition of soda-sand mixtures; a) plot of the voltage drop  $U_x$  and temperature, b) plot of the electrical conductivity  $\kappa$  in  $\text{ohm}^{-1}\cdot\text{cm}^{-1}$  as  $\log \kappa$ , both as a function of temperature

### **b) Soda ash - sand (varied grain sizes)**

As this system is probably the most important sub-system of commercial mass glass batches, it has been studied many times before. Yet there are still many aspects which need clarification. One of the most important questions refers to the role of grain size. Earlier DTA studies gave very dim insights only, which is a direct consequence of the small sample sizes used in the method. The newly developed method helps to overcome this difficulty.

Figure 41 a shows the electrical conductivity plots for 3 different particle size fractions of quartz sand in 50 : 50 mixtures of soda ash and sand. The fractions 335-500  $\mu\text{m}$ , and 185-200  $\mu\text{m}$  were obtained by sieving an industrial grade sand, while the fraction denoted  $< 40 \mu\text{m}$  is a quartz powder used in ceramic industry with a  $d_{90} < 40 \mu\text{m}$ . The soda ash used is an industrial grade material. For the coarse fractions, electrical conductivity exhibits a more or less steady decrease between 300 and 800  $^{\circ}\text{C}$ , which is due to the increasing solid state mobility of the  $\text{Na}^+$  ion. For increasingly finer fractions, this tendency is superimposed by a reaction immobilizing the  $\text{Na}^+$  again. The reaction is strongest between 600 and 750  $^{\circ}\text{C}$ . For the quartz powder, this is the predominant reaction, while for the fractions sieved from the industrial grade sand, it is an additional effect only. The observed reaction is most likely a solid state formation of sodium silicates. Figure 41 b shows the formation of primary melt, for all fractions, it occurs in the range between 820 and 835  $^{\circ}\text{C}$ . In the quartz powder sample, primary melt formation is immediately followed by the precipitation of a new solid phase. Thus a sequence of melt formation is observed.

The shapes of the curves in figures 40 and 41 prior to the onset of melting are attributed to the ratio of soda ash surface to sand surface. For a rough estimate, let us assume a mean particle diameter for the as-received raw materials of 300  $\mu\text{m}$ , yielding a specific surface area of approx. 77  $\text{cm}^2/\text{g}$ . The sand fractions 355-500  $\mu\text{m}$ , 185-250  $\mu\text{m}$ , and  $< 40 \mu\text{m}$  yield 55, 110, and 770  $\text{cm}^2/\text{g}$ , respectively. This leads to surface area ratios soda : sand of 1.4, 0.7, and 0.1, respectively. In the tests with varied mass ratios, similar surface area ratios soda : sand are realized for the 60 : 40, 40 : 60, and 10 : 90 mixtures. Hence, a similar course of the voltage drop curves is found.

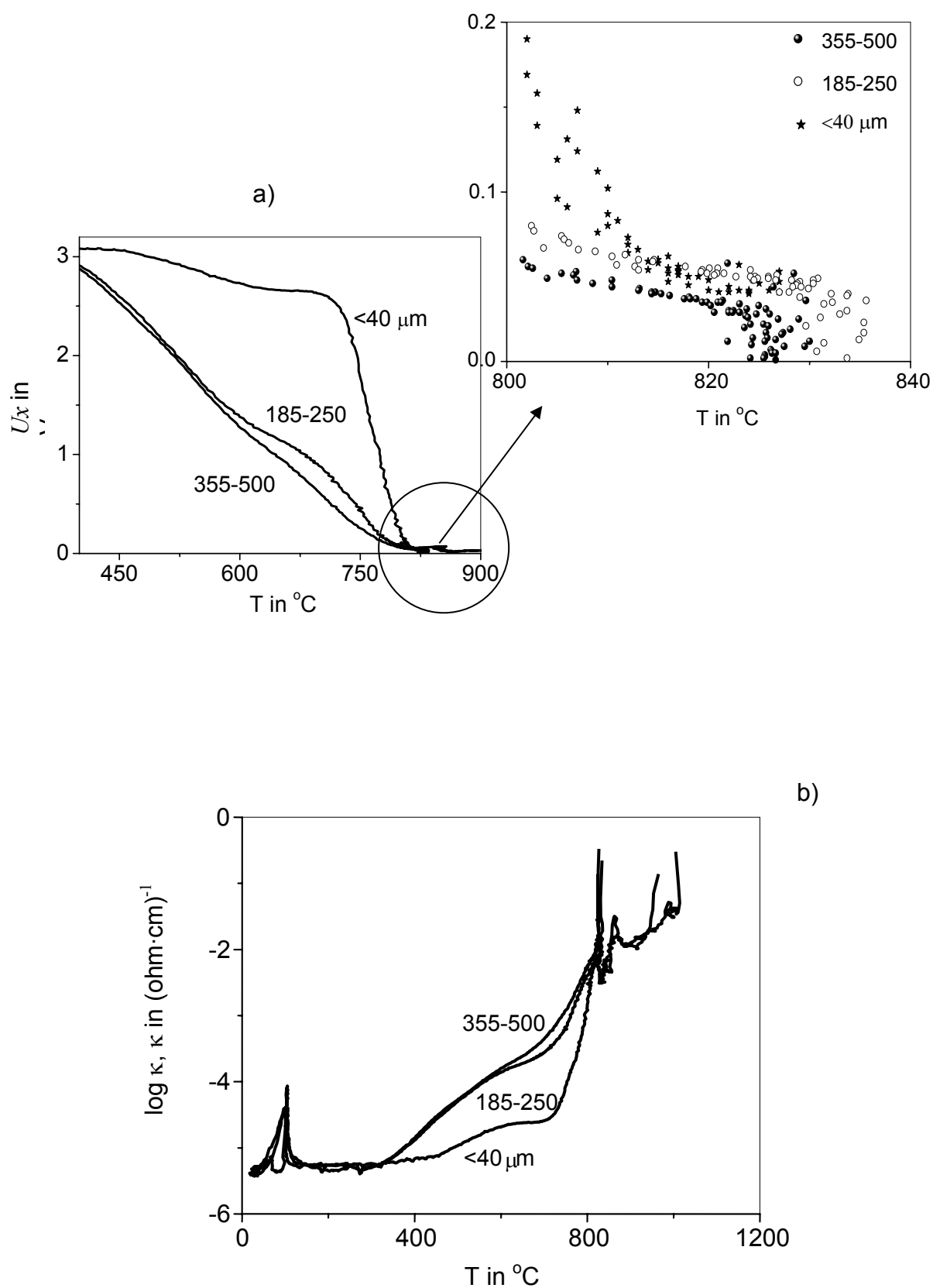


Fig. 41. Illustration of soda-sand mixtures; grain size fractions of sand varied; a) electrical conductivity signals, and b) voltage drop signals

The DTA data show that the predominant reaction for heat turnover is NS-NS<sub>2</sub> eutectic melting. A detailed analysis is presented in figure 42. In general, all the curves are similar, but, as the grain size of the silica is decreased, an endothermic peak is shifted towards higher temperature from 825 to 850 °C.

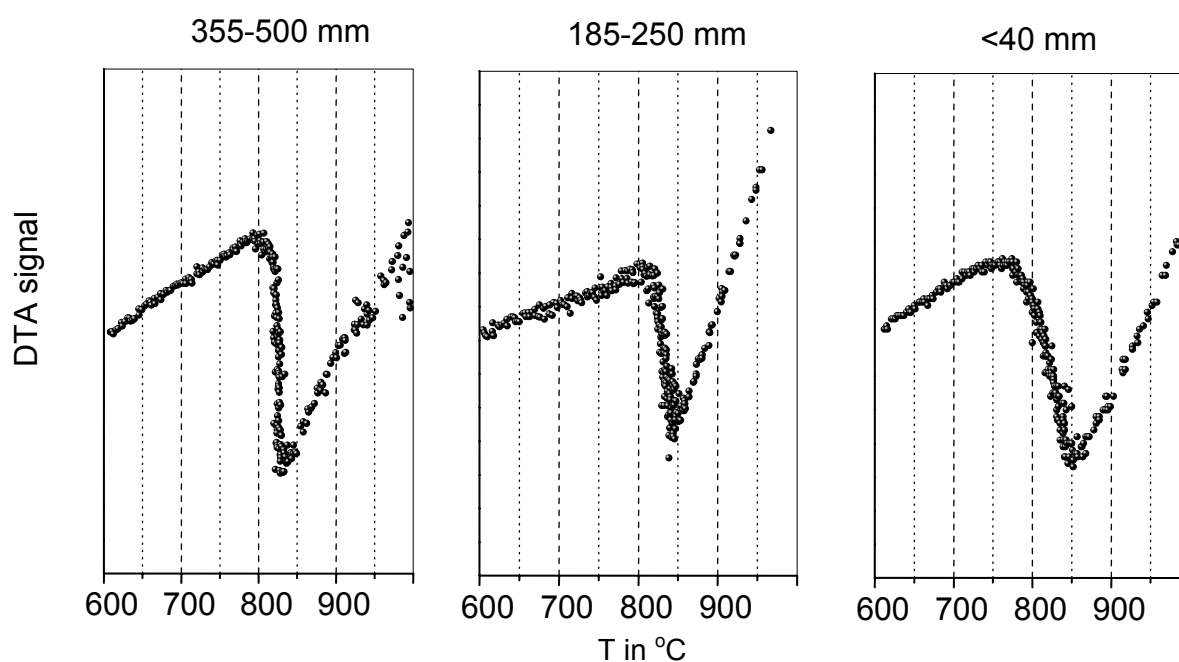


Fig. 42. DTA plots of mixtures soda ash and sand; grain size fractions of sand varied; area relevant for primary melt formation enlarged

### b) Soda ash - limestone

For the mixture of soda ash and limestone, the electrical conductivity begins to rise beyond 358 °C. This temperature was also found to be related to an effect by slowing down weight loss found in DTGA experiments [6-7]. Primary melt formation occurred at 720 °C, compared to the eutectic point of Na<sub>2</sub>CO<sub>3</sub>-Na<sub>2</sub>Ca(CO<sub>3</sub>)<sub>2</sub> at 785 °C. After this a fluctuation of the foam formation signal was quite high in the temperature range of 700-1050 °C due to the high gas release, presumably limestone, as can be seen in figure 43.

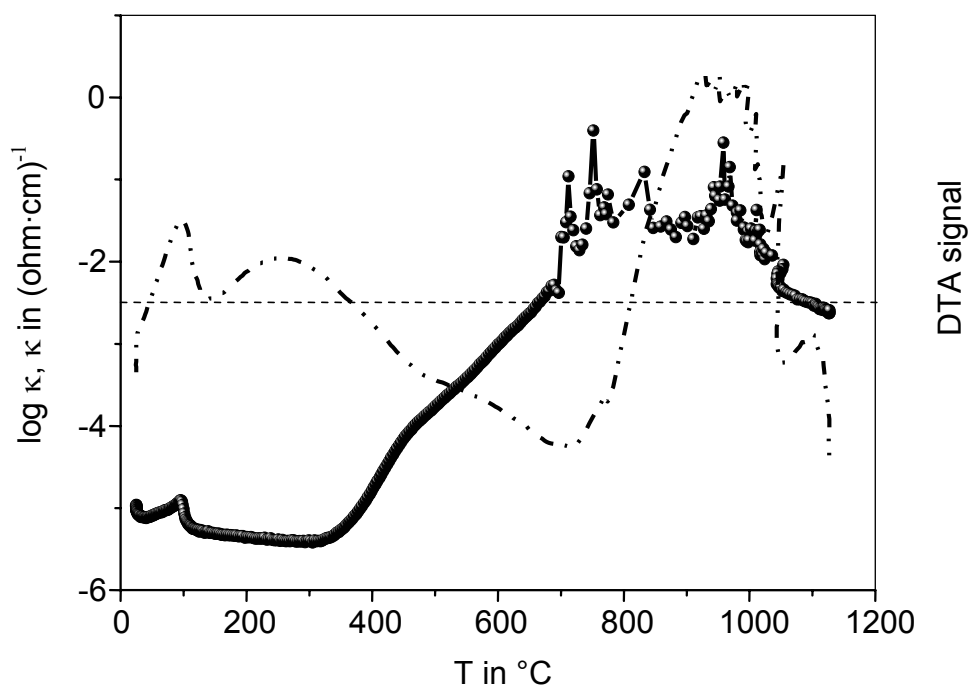


Fig. 43. Plot of a) DTA and b) electrical conductivity signals of mixed soda-limestone

### c) Soda ash - dolomite

Electrical conductivity of the mixture between soda ash and dolomite shows strong reaction peaks (DTA signal) between 550-1000 °C (figure 44) and low primary melt formation temperature at 681 °C, which is close to the decomposition peak detected by [45] at 680 °C. The reaction foam stage extends over a wide temperature range.



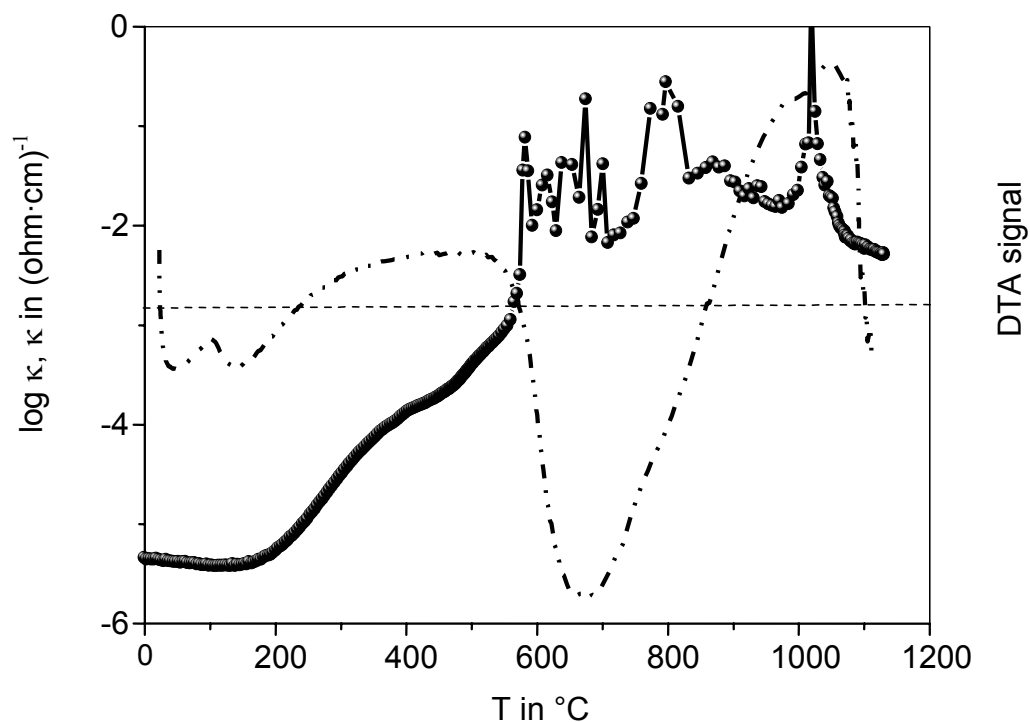


Fig. 44. Plot of a) DTA and b) electrical conductivity of mixed soda-dolomite

#### d) Soda ash - phonolite

This system shows a reaction peak right below 800 °C and a very sharp onset of melting at 835 °C. The reaction between soda and phonolite is very violent. The melt literally jumped out of the crucible.

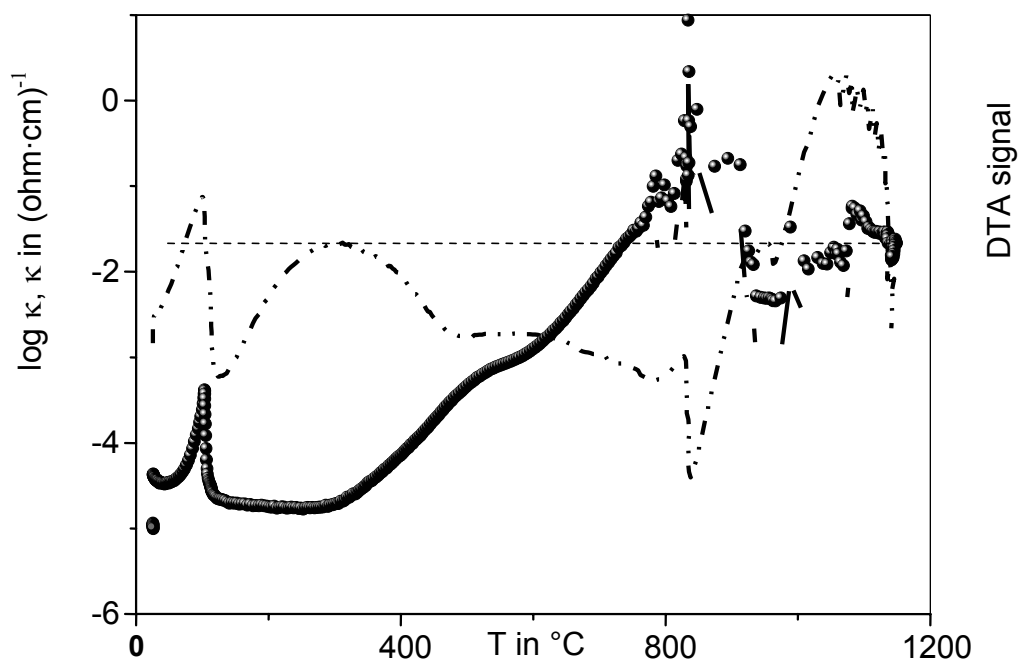


Fig. 45. Plot of a) DTA and b) electrical conductivity of mixed soda-phonolite

#### 4.1.6 Test on ternary mixtures

Two significant effects can be seen in this experiment. Firstly, foam formation of the mixture between soda-sand-phonolite is less than soda-sand-lime and soda-sand-dolomite. These three systems have relatively similar electrical conductivity values. However, a slightly higher value could be detected in the soda-sand-dolomite system (figure 46). Secondly, the signals of three-component systems appear in between that of the two binary systems containing sand (figure 47). For example, in soda-sand-dolomite, the first melt formation, electrical conductivity, and DTA signals appear between the signals of soda-sand and soda-dolomite.

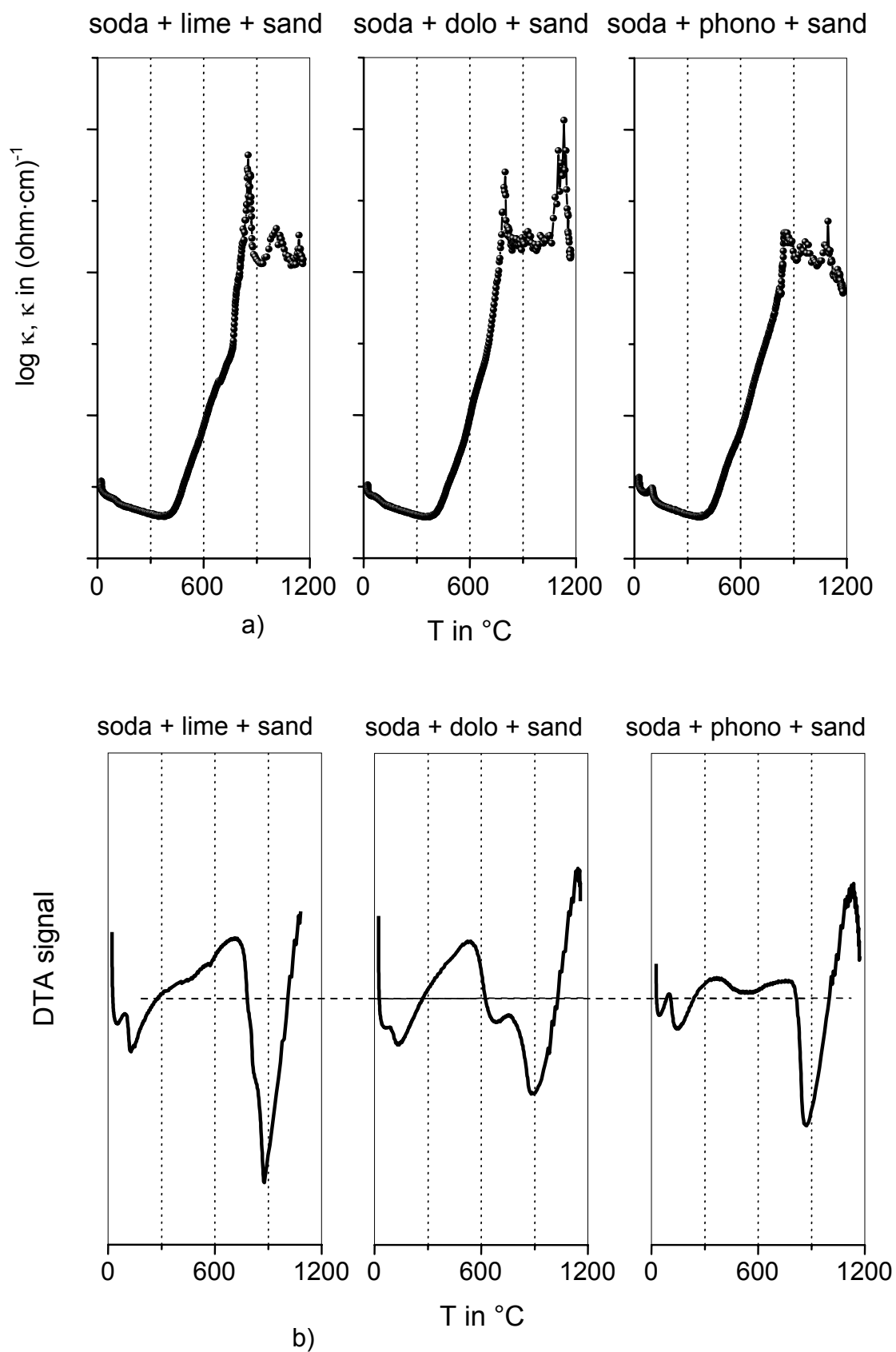


Fig. 46. Illustration of a) electrical conductivity plot with temperature, and b) plot of DTA signals with temperature

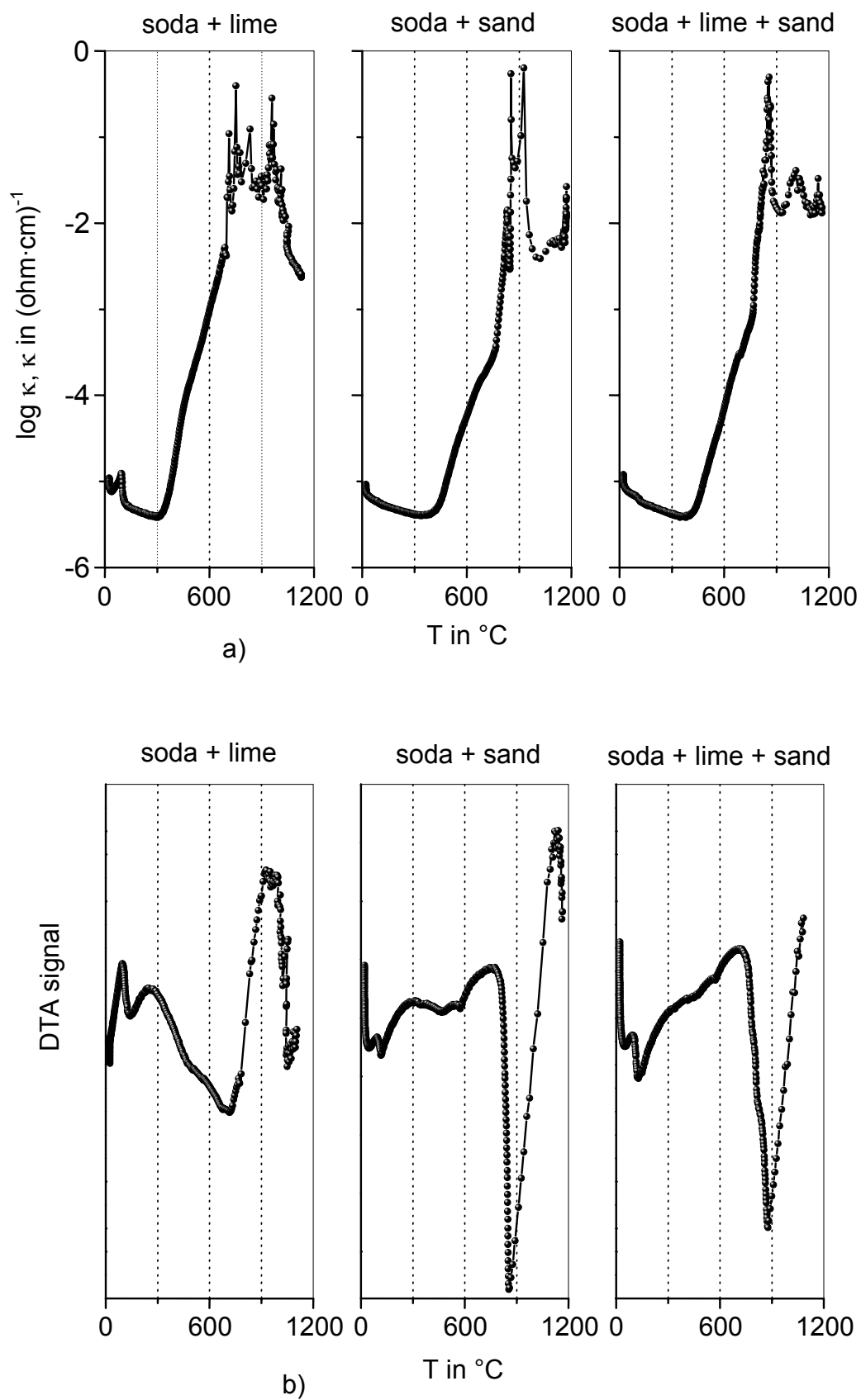


Fig. 47. Investigation of soda-lime-sand system showing a) electrical conductivity and b) DTA signals

### 4.1.7 Test on multi-component mixtures

#### a) Six commercial glass batches

In multi components tests, six different glass batches (see composition in tables 6 and 7) were investigated. As can be seen in figures 48 and 49, their electrical conductivity signals are more complex than the former results (in 4.1.2 and 4.1.3). This is because they have more complex reactions than two or three components systems. Due to higher fluxing content, crystal glass shows the lowest primary melt formation with a slightly higher electrical conductivity than container flint 1.

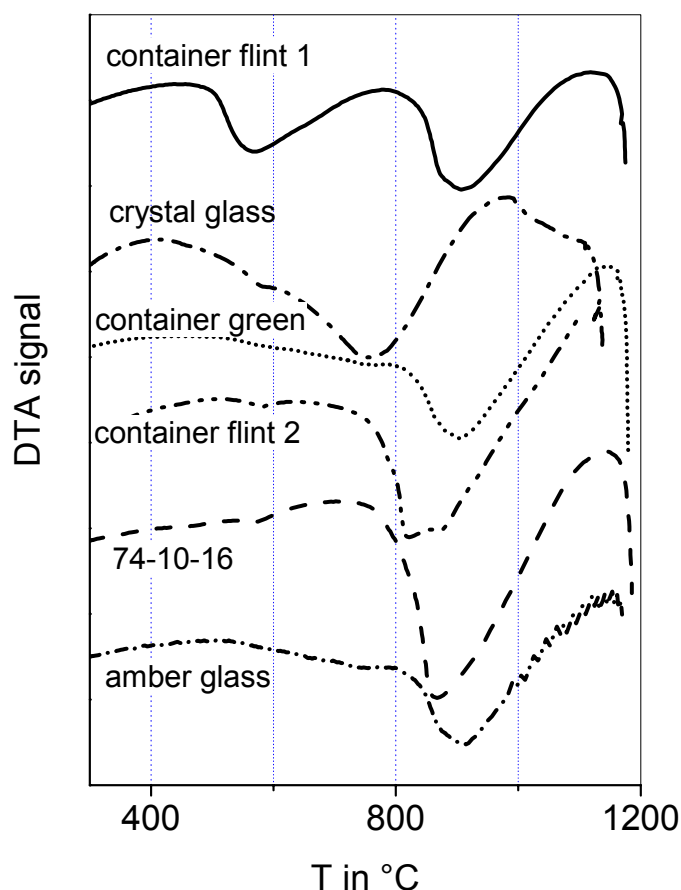


Fig. 48. DTA signals of container flint 2, container green, crystal, container flint 1, 74-10-16, and amber glasses

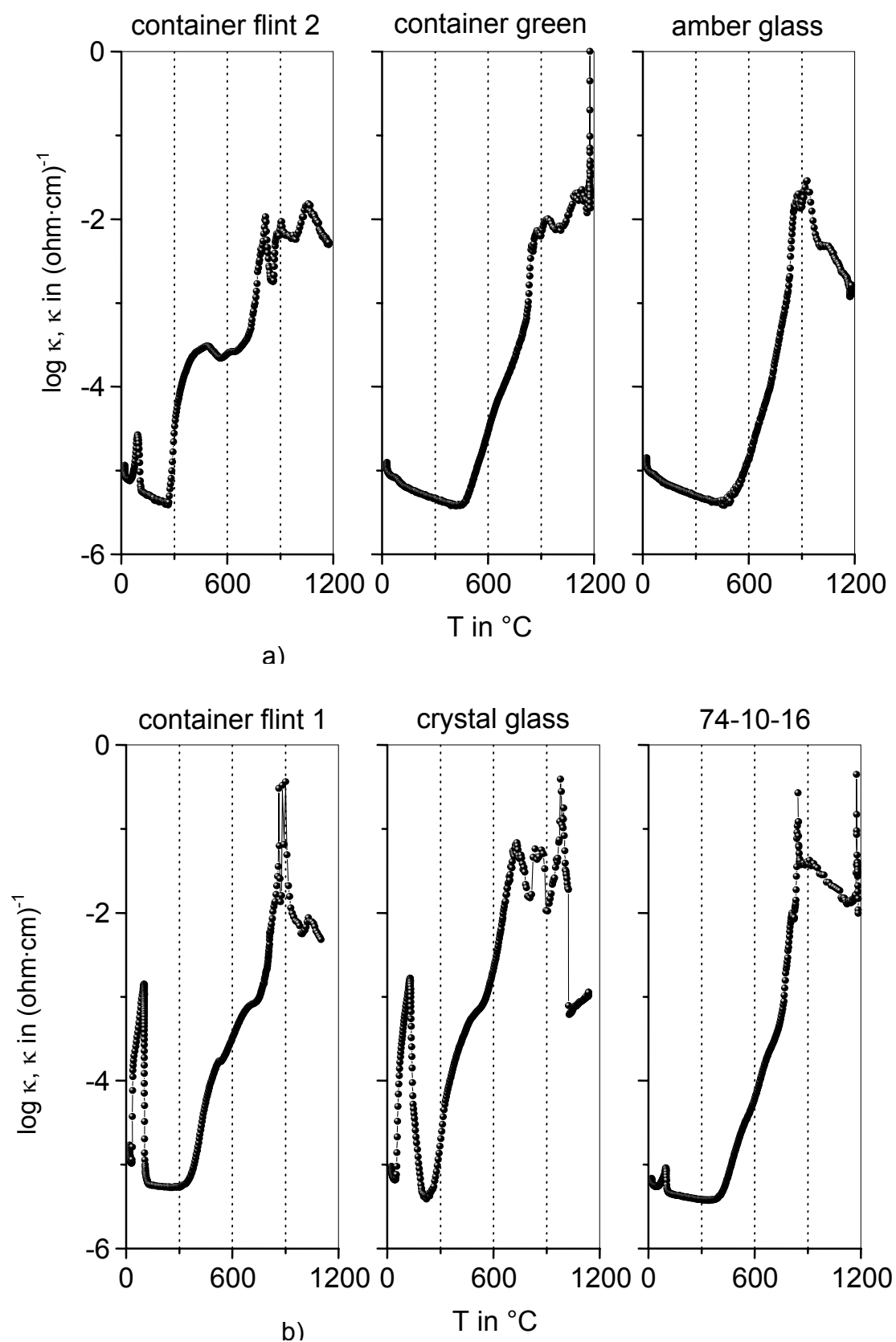


Fig. 49. Investigation of multi-component batches showing the electrical conductivity signal for container flint 2, container green, and amber glass batches a), and container flint 1, crystal, and 74-10-16 glass b)

**b) Influence of different atmospheres on the 74-10-16 glass batch**

Electrical conductivity of glass batch 74-10-16 was also performed under flowing of CO<sub>2</sub> at 10 l/h, and H<sub>2</sub>O:N<sub>2</sub> (50:50) at 56 l/h. As a function of temperature, both tests yield similar electrical conductivity (fig. 50 b) and caloric effects (fig. 50 c). However, under flowing of H<sub>2</sub>O-N<sub>2</sub> atmosphere, there is a significantly accelerated onset of melting and a likewise significantly reduced reaction foam period (fig. 51 a).

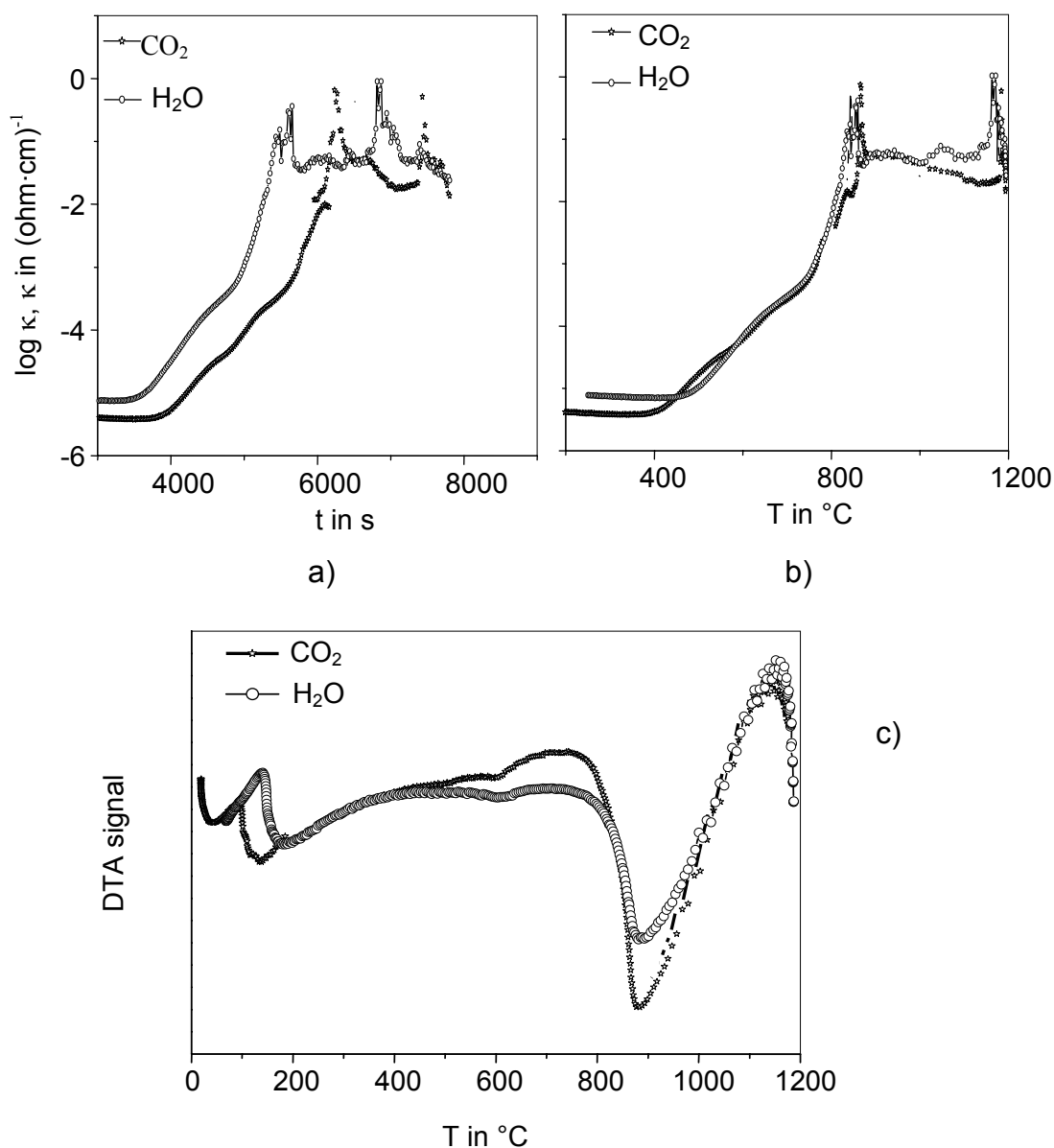


Fig. 50. Influence of atmospheres on melting reactions of glass 74-10-16; a) plot of electrical conductivity vs. time, b) plot of electrical conductivity vs. temperature, and c) plot of DTA signal vs. temperature

### c) Lead glass cullet melt measured with double cylinder sensor

As describe before in section 3.2.1, two types of sensors were applied for electrical conductivity test. All results described earlier were employed from the solenoid type sensor. For this type of sensor, the cell constant is estimated to approx.  $1 \text{ cm}^{-1}$ , which is sufficient for the interpretation of the results. If batches are to be characterized for the use in electrical furnaces, then the use of a more accurate method is recommended. An alternative to measure  $C_{\text{cell}}$  for the solenoid sensor by using pure liquid NaCl failed. NaCl seemed to be an appropriate standard since tabulated resistivity values are available at a high accuracy. However, in the course of experiments, it turned out that NaCl reacted with Pt. So, different strategies for the determination of  $C_{\text{cell}}$  were chosen.

An upper estimation of the cell constant  $C_{\text{cell}}$  is derived by plane geometry equivalent with areas equal to half the cylinder envelope (at immersion depth  $L$ ) kept at a distance  $d_{\text{eff}}$ . This yields  $C_{\text{cell}} = 1.0$  and  $0.5 \text{ cm}^{-1}$  for  $L = 1$  and  $2 \text{ cm}$ , respectively. Measurement in glass melts at different immersion depth and extrapolation toward  $L = 0$  helped to quantify the additional effect of the cylinder faces, yielding overall  $C_{\text{cell}}$  values of  $C_{\text{cell}} = 0.55$  and  $0.35 \text{ cm}^{-1}$ , respectively. Finally measurements in aqueous KCl solution (71.13 g KCl filled to a total amount of 1 kg solution by D.I. water) were used for calibration. For this solution, tabulated data for the electrical conductivity are available at highest accuracy (see table 12). The cell constants determined for 1000  $\text{Hz}$  were  $C_{\text{cell}} = 0.591$  and  $0.345 \text{ cm}^{-1}$ , respectively, which is in excellent agreement with the values derived by geometrical considerations and the additional measurements at varied immersion depths  $L$ . With the KCl calibration method thus confirmed, the cell constant of the solenoid type sensor was determined, too. Due to its design,  $C_{\text{cell}}$  is approx. independent of the immersion depth, with  $C_{\text{cell}} = 5.1$  and  $0.56 \text{ cm}^{-1}$  for 50 and 1000  $\text{Hz}$ , respectively.

Table 13 summarizes the results derived for the lead crystal melt under isothermal conditions. Due to the improved calibration procedure, the reported resistivities are higher by a factor of approx. 5 to 10 than those reported



before (reading 5.9 and 4.5 ohm-cm at 1000 and 1100 °C, 1000 Hz, respectively).

Table 12. Conductivity standard solutions, KCl in D.I. water

soln. a	71.1352 g KCl filled up to 1 kg of total soln.
soln. b	7.41913 g
soln. c	0.745263 g

1/T 1000/K	T in °C	soln a $\kappa$ in ( $\Omega \cdot \text{cm}$ ) <sup>-1</sup>	soln. b $\kappa$ in ( $\Omega \cdot \text{cm}$ ) <sup>-1</sup>	soln. c $\kappa$ in ( $\Omega \cdot \text{cm}$ ) <sup>-1</sup>
<u>standard data</u>				
3.660992	0	65.144	7.1344	0.77326
3.424655	18	97.790	11.1612	1.21992
3,354016	25	111.287	12.8497	1.40808

Table 13. Resistivity measurement with pure lead glass cullet melt, double cylinder sensor under isothermal conditions

type of tests	dept in cm	T in °C	R <sub>x</sub> in $\Omega$	$\kappa$ in ( $\Omega \cdot \text{cm}$ ) <sup>-1</sup>
circuit A, 1000 Hz	2.0	900	31.7	0.018
	1.0	900	51.3	0.011
	2.0	1000	15.4	0.036
	1.0	1000	25.9	0.022
	2.0	1100	8.7	0.064
	1.0	1100	15.9	0.035
circuit B, 1000 Hz	2.0	900	19.3	0.029
	2.0	1000	9.79	0.057
	2.0	1100	6.13	0.091
bridge C, 1000 Hz	2.0	900	19.25	0.029
	2.0	1000	9.80	0.057
	2.0	1100	6.06	0.092

The results of the non-isothermal tests are shown in figure 51 a-c. They were performed on batches without cullet, i.e., with primary raw materials only. The  $U_x$  versus  $T$  plot in figure 51 a displays a large peak related to the removal of physical batch water, an increase of solid state ionic mobility in the regime of 200 to 500 °C, a solid state reaction taking place at approximately 520 to 580 °C, and the formation of a primary liquid phase at exactly 779 °C. The conductivity assumes very high values as soon as the primary liquid phase appears (fig.51 b). For reasons of comparison, the values of the pure cullet melt are shown in figure 51 c, too. When the melting process is accomplished (i.e., all quartz is dissolved), then usually the melt assumes conductivities significantly lower than during batch melting as demonstrated in figure 51 c, the same data of the batch are presented as already shown in figure 51 b, however, extended to temperatures of 1200 °C and plotted versus the exposure time.

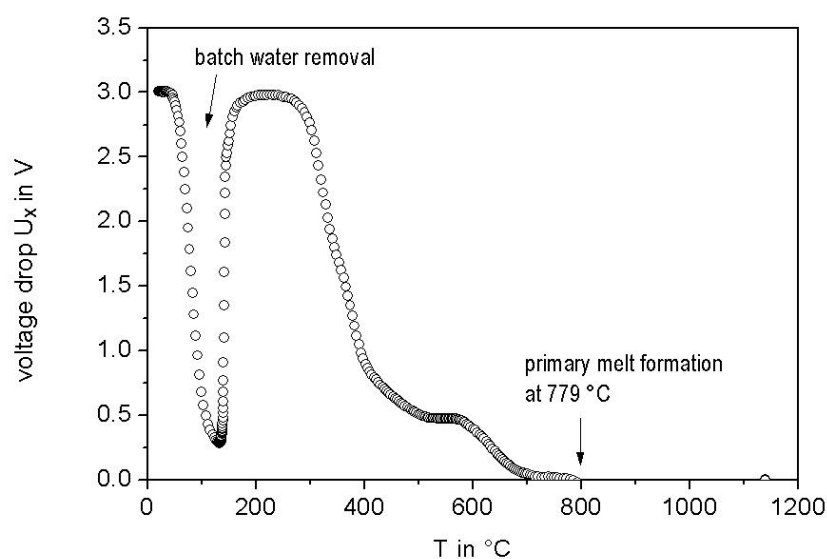


Fig. 51 a. Voltage drop across a lead glass batch (see table 6, chapter 3) during heating at 10 K/min; external voltage 3 V AC (50 Hz), presented as a function of temperature

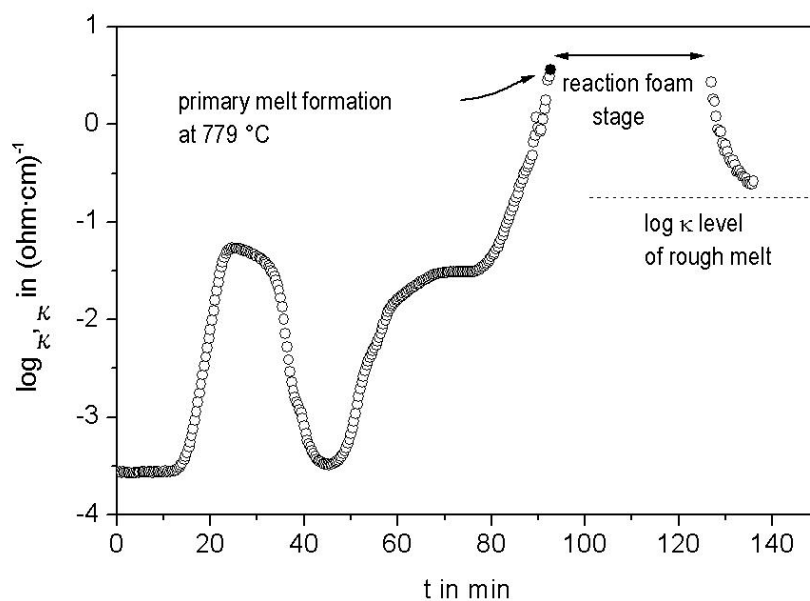


Fig. 51 b. Electrical conductivity  $\kappa$  in a lead glass batch heated up at 10 K/min, presented as a function of time; the onset of melting occurs at 779 °C, the reaction foam stage lasts about 35 min

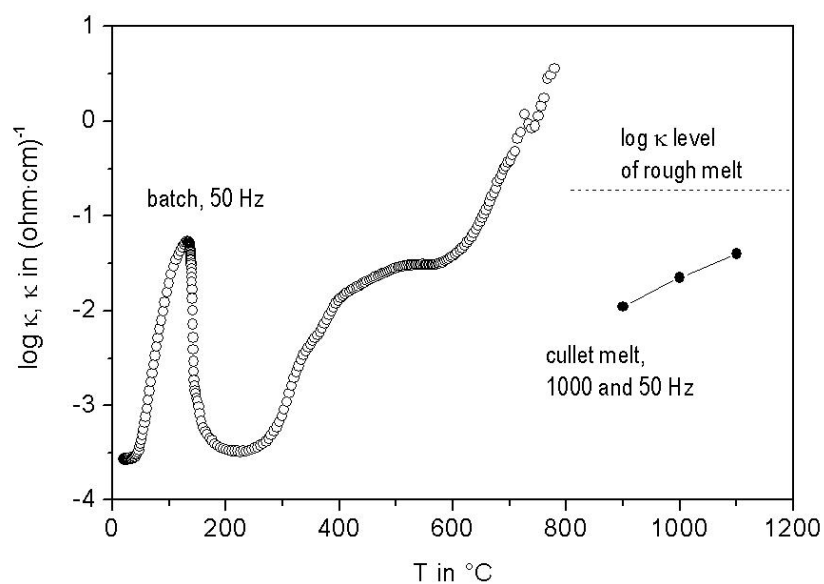


Fig. 51 c. Electrical conductivity  $\kappa$  in a lead glass batch heated up at 10 K/min, presented as a function of temperature; the data are contrasted to data for the pure glass melt measured at 900 to 1100 °C (see table 13), and to the level of rough melt (figure 51 b)

After the initial period leading to the formation of a primary salt-like melt and to a steep increase of the electrical conductivity, a chaotic period follows where the conductivity strongly fluctuates between the values of a salt melt and a silicate melt. This period characterized by the time interval is termed reaction foam period. During this time interval, an intensive chemical turnover accompanied by gas release takes place, resulting in the said chaotic fluctuations. Finally, the conductivity steadily approaches lower values corresponding to the glass melt (as seen from a comparison with the values for the pure glass melt in figure 51 c).

## 4.2 Thermal diffusivity

### 4.2.1 Calculation of the thermal diffusivity

The following relation gives the expression of heat transfer by heat conductance in an unsteady state:

$$\frac{\partial \vartheta}{\partial t} = a \cdot \frac{\partial^2 \vartheta}{\partial x^2} \quad (4.4)$$

A heat pulse generated at time  $t = i \cdot \Delta t$ , recorded at a distance  $r^*$ , yield a temperature pattern expressed as follows:

$$T_i(t) = \text{const} \cdot (4 \pi \cdot a \cdot t)^{-3/2} \cdot \exp - \frac{(r^*)^2}{4 \cdot a \cdot t} \quad (4.5)$$

$t = (r^*)^2 / (6 \cdot a)$  corresponds to the maximum temperature. The temperature pattern registered by superimposition of several heat pulses at a distance  $r^*$  is shown in figure 52. The mathematical expression of the curve obtained by summing the heat pulses is given by:

$$T(t) = \sum_{i \geq 0} \theta(t - i \cdot \Delta t^*) \cdot T_i(t) \quad (4.6)$$

where  $\theta$  is a step-function having a value of unity for  $t \geq i \cdot \Delta t^*$  and zero for  $t < i \cdot \Delta t^*$ . The value  $\Delta t_{\text{exp}}$  cannot be used to directly calculate the thermal diffusivity because of its dependence on  $\Delta t^*$ . The following empirical expression for the relation between the three time values was focused:

$$\Delta t_{\text{exp}} / \tau \approx 0.981 + 1.06 \cdot \tau / \Delta t^* + 0.184 \cdot (\tau / \Delta t^*)^2 \quad , \quad (4.7)$$

where  $\Delta t^*$  and  $\tau$  are experimental parameters,  $\Delta t_{\text{exp}}$  is evaluated. Thus, using eq. (4.6) the thermal diffusivity can be calculated.

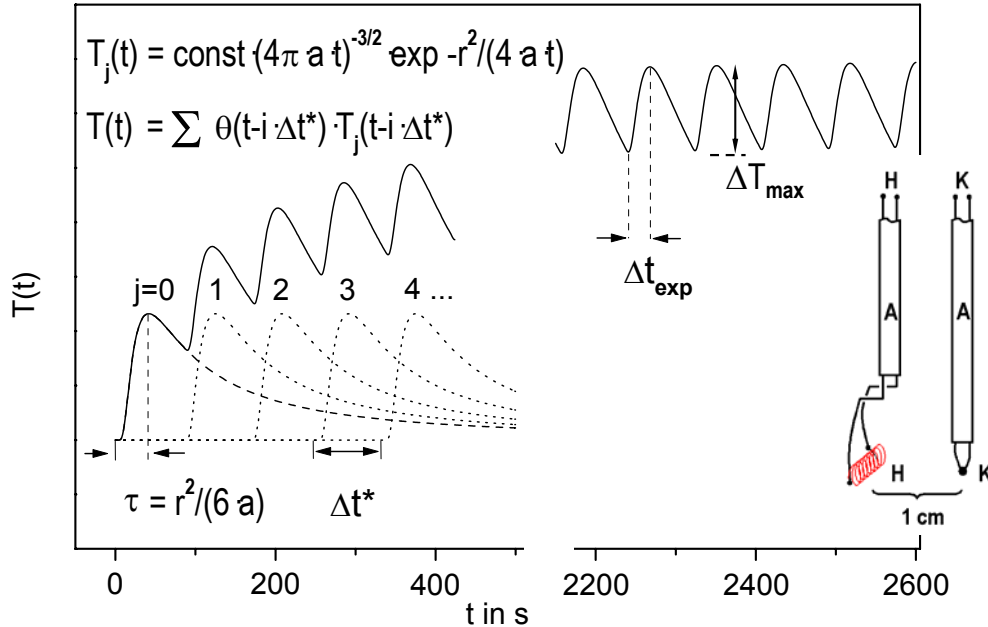


Fig. 52. Superimposition of heat pulses registered at a distance  $r$  from the heating source  $T_j(t)$ ,  $i = 0, 1, 2, \dots$  as a summed curve;  $t$  = duration of heat pulse,  $\Delta t^*$  = time between two pulses,  $\Delta t_{\text{exp}}$  = runtime

#### 4.2.2 Evaluation of immediate results

A typical signal is obtained from the difference between the average batch temperature  $T^*$  and the instant batch temperature  $T_b$ . From the thermal diffusivity experiments, data were collected and evaluated for 100 K ranges between 300 and 700 °C. Figure 53 shows an example of a sodium silicate glass batch in the range of 400 to 500 °C. Each peak is evaluated numerically in the way illustrated in figure 49. An enlargement of the curve is required for evaluating the time  $\Delta t_{\text{exp}}$  (figure 54). The evaluation over the entire time scale of the succession of heat pulses is a statistically reliable analysis. A software program is then used to calculate the thermal diffusivity of the batch. The computer records values each second. Thus, for every range, an average value of the thermal diffusivity based on at least three temperature peaks is obtained.

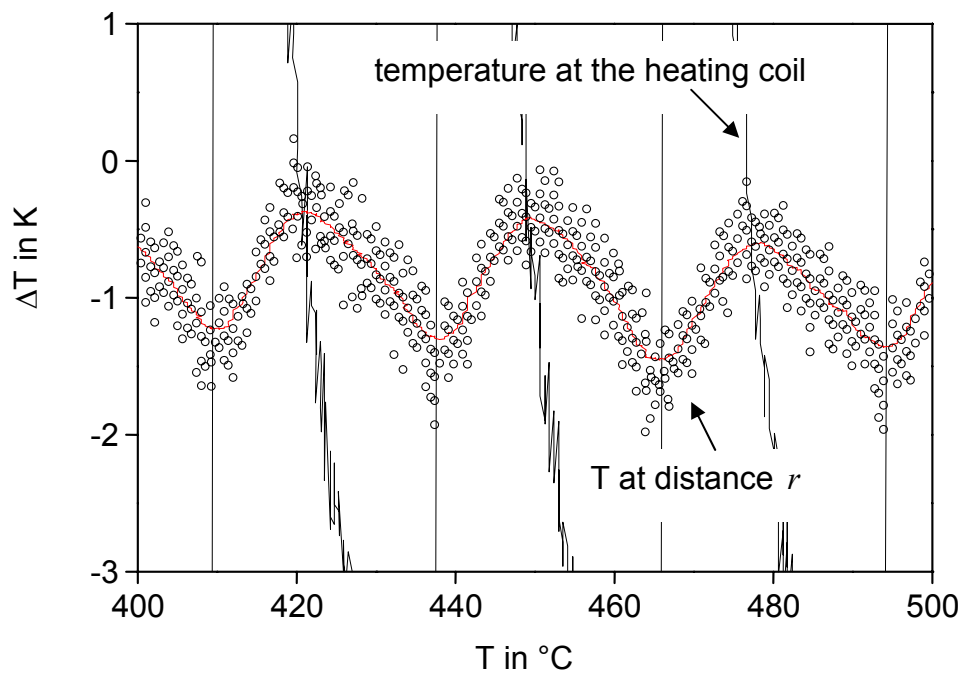


Fig. 53. Plot of temperature difference between sensor and batch vs. overall batch temperature (at the heating coil and at distance  $r$ ); the steep curves show the temperature pulse at the heating coil in the range of 400-500 °C.

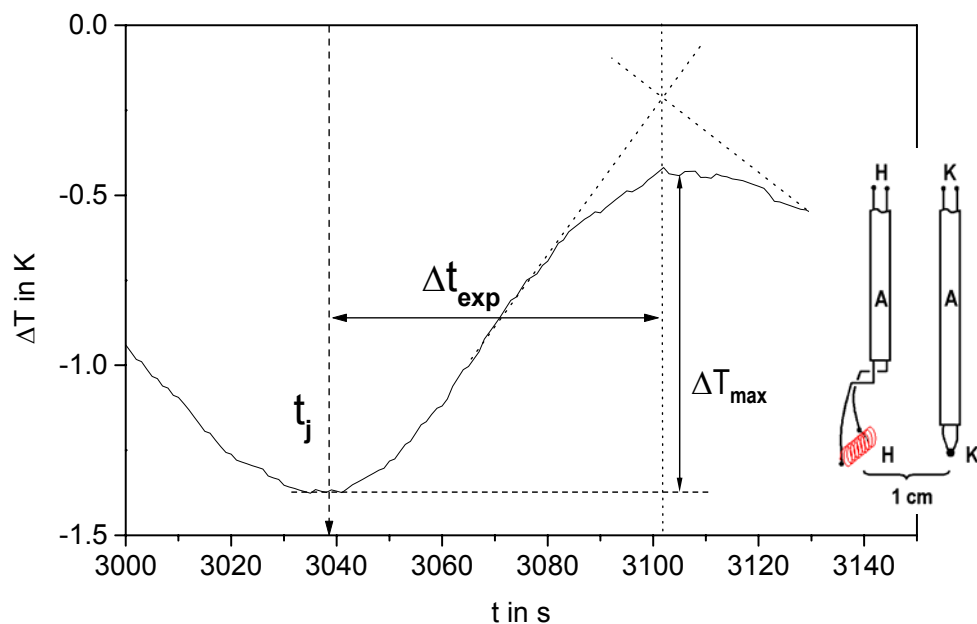


Fig. 54. Plot of time vs. temperature difference between sensor and batch;  $t_j$  represents the beginning of the pulse and  $\Delta t_{\text{exp}}$  represents the run time

### 4.2.3 Accuracy of the measurement

Before measuring the thermal conductivity of the real glass batches, the accuracy of the system was firstly checked by silica sand as can be seen in figure 55. The tests were performed at different frequencies and different interval times. An optimum output signals was observed at the frequency of 50 Hz and a time interval of 150 s. After that two different sand grain sizes were tested. Of course, the thermal diffusivity loose its meaning in the vicinity of a phase transition. In the given example, an evaluation cannot be performed in the vicinity of the quartz inversion. Right below and above, the evaluation remains unaffected.

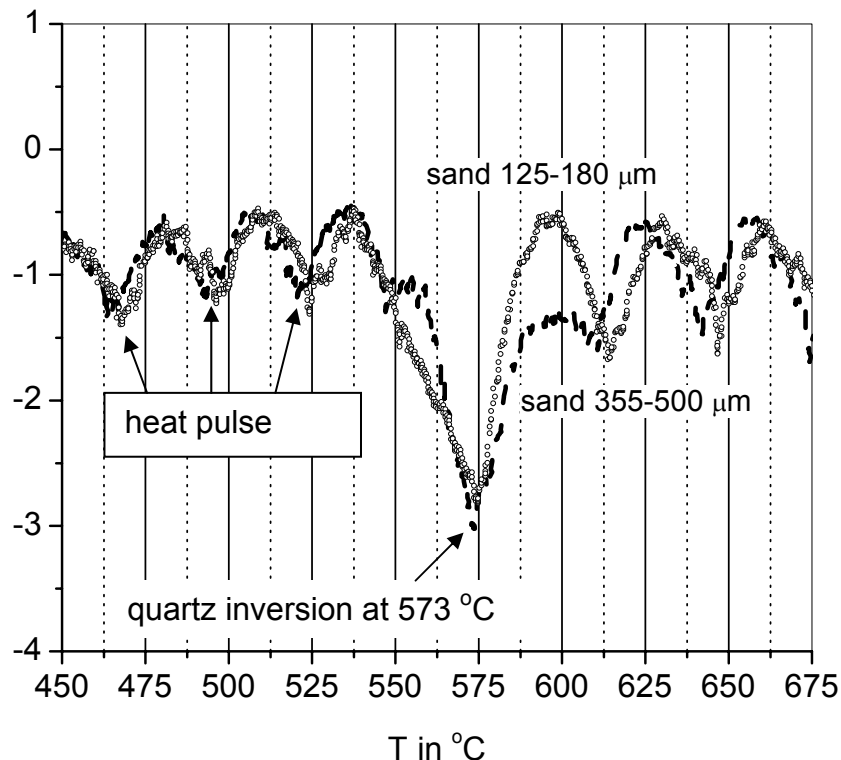


Fig. 55. Illustration of the tests from silica sand indicated quartz inversion at 573 °C

### 4.2.4 Examples of the measurement

#### a) Sand: at different grain sizes

Thermal diffusivity of three different grain sizes of sand from Quarzwerke Frechen was investigated. The results are summarized in table 14. Since thermal conductivity values in bulk solids are extremely difficult to

validate, a calculation was performed in parallel according to [63]. From the measurement, it follows that for a finer grain size distribution the thermal diffusivity is lower. All three grain fractions show a correlative of  $\kappa$  value with temperature as can be seen in figure 56.

Table 14. Thermal conductivity (a) of sand at different grain sizes

T in °C	a at different grain sizes in $10^{-3} \text{ cm}^2/\text{s}$		
	125-180 $\mu\text{m}$	180-250 $\mu\text{m}$	355-500 $\mu\text{m}$
300-400	$2.91 \pm 0.3$	$4.09 \pm 0.1$	$3.71 \pm 0.1$
400-500	$3.35 \pm 0.1$	$4.12 \pm 0.1$	$3.78 \pm 0.0$
500-600	$3.45 \pm 0.0^*$	$4.07 \pm 0.2$	$3.97 \pm 0.1$
600-700	$3.71 \pm 0.3$	$4.54 \pm 0.1$	$4.24 \pm 0.2$
700-800	$4.02 \pm 0.3$	$4.86 \pm 0.1$	$4.97 \pm 0.0$
800-900	$4.95 \pm 0.1$	$5.15 \pm 0.1$	$5.18 \pm 0.0$

\*) only one peak is evaluated, a = thermal conductivity

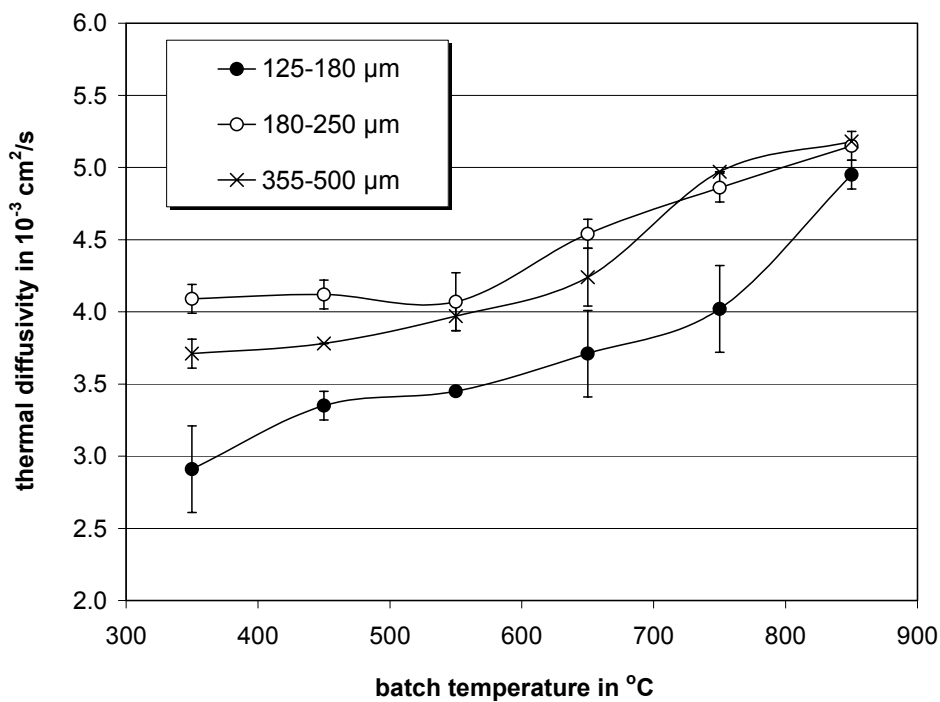


Fig. 56. Plot of thermal conductivity (a) with batch temperature of different grain sizes of sand; error bar indicates possibility error from the calculation



## b) Conventional glass batches

Four glass types of 74-10-16, container green, container flint 2, and crystal glasses were investigated. A summary of the results is shown in table 15. The calculations confirm that the measurement results may be trusted. Vice versa, we may learn from this comparison that the grain to grain contact in the model should be taken into account by a dimensionless shape factor [69] of 2.5 to 3.5 for glass batches (1.25 denotes hard spheres with point contact).

Table 15. Thermal conductivity  $\alpha$  of different glass types in  $10^{-3} \text{ cm}^2/\text{s}$ ; pulse time every 150 s, pulse length 10 s

glass types	300-400 °C	400-500 °C	500-600 °C	600-700 °C
soda lime silicate	$3.4 \pm 0.2$	$3.7 \pm 0.1$	$3.9 \pm 0.1$	$4.2 \pm 0.3$
green	$3.4 \pm 0.1$	$3.6 \pm 0.2$	$3.4 \pm 0.0$	$4.1 \pm 0.2$
crystal	$3.9 \pm 0.1$	$4.2 \pm 0.1$	$4.3 \pm 0.2$	$4.6 \pm 0.2$
white	$3.2 \pm 0.1$	$3.2 \pm 0.1$	$3.6 \pm 0.4$	$3.7 \pm 0.1$
calculation by using shape factors between 2.5-3.5				
glass types	350 °C	450 °C	550 °C	650 °C
white*	2.7 - 3.3	2.9 - 3.6	3.0 - 3.7	3.5 - 4.3

\*) theoretical thermal conductivity in  $10^{-3} \text{ cm}^2/\text{s}$ ;  
shape factors between 2.5-3.5

## 4.3 Heating microscope

### 4.3.1 Conventional use

Conventional evaluation of the results obtained from heating microscope is the observation and identification of several characteristic temperatures (see DIN 51730, [61]). A set of temperatures described here is: the start of visible gas release (bubbling) (T1), the round edge point (T2), and the half sphere point (T3). Two groups of tests; i.e., commercial glass batches and 74-10-16 glasses added with small additives were investigated.

### a) Commercial glass batches

Four commercial glass types; 74-10-16, container green, container flint 1, and crystal glasses were investigated by heating microscope. The results of T1, T2, and T3 clearly depend on the type of the batch. The start of visible gas release was found at 870 °C for silicate, at 857 °C for green, at 791 °C for white, and at 715 °C for crystal glasses. The lowest temperature of the round edge point was observed at 731 °C for crystal glass, which contains low liquidus raw materials such as  $\text{KNO}_3$ , and borax. The half sphere point was observed at 1063 °C for silicate, at 1029 °C for green, at 1080 °C for white, and 921 °C for crystal glasses as presented in figure 57.

Comparison of these tests with conductometry experiments in figure 49 a) show a correspondent of T1 as a primary melt formation point, T1-T3 relate to the foam interval, and T3 represent an onset peak of primary melt formation (figure 19 b), however within an accuracy of  $\pm 20$  °C.

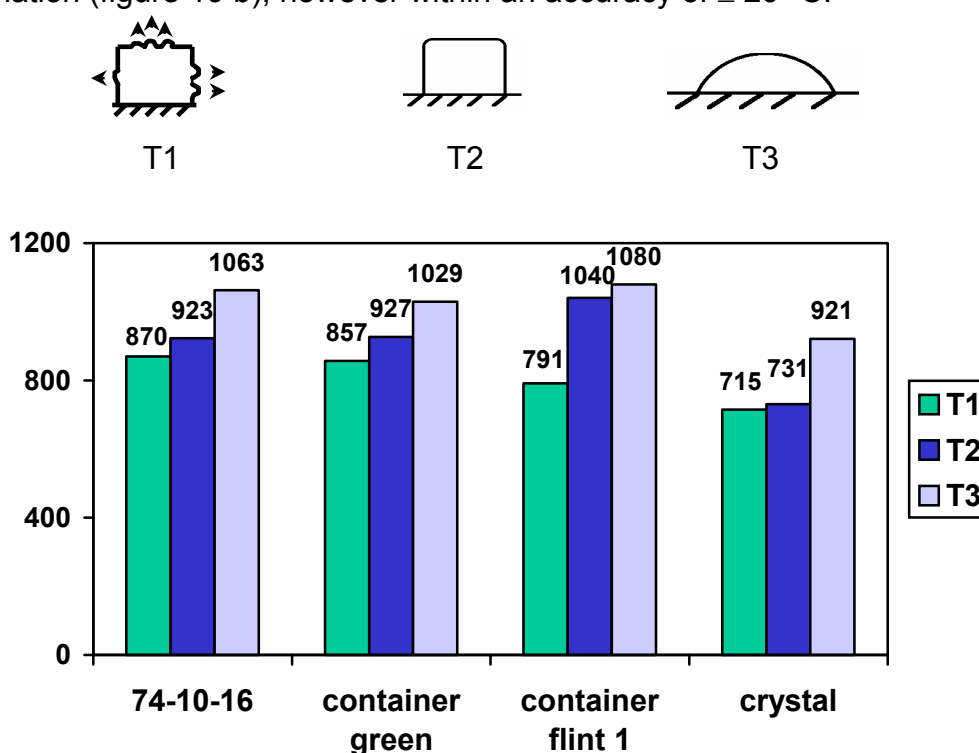


Fig. 57. Illustration of (T1) start of visible bubbling, (T2) softening point, and (T3) half sphere point determined from heating microscope of different glasses

### b) Soda lime silicate glasses with minor additives

Additional small amounts of NaCl, NaNO<sub>3</sub>, and NaOH at 1 wt. % in soda lime silicate batch were investigated by heating microscope. The two significant temperatures T1 and T2 were observed as shown in figures 58 a-b. Additions of NaCl showed the strongest effect of lowering the sintering temperature of the batch.

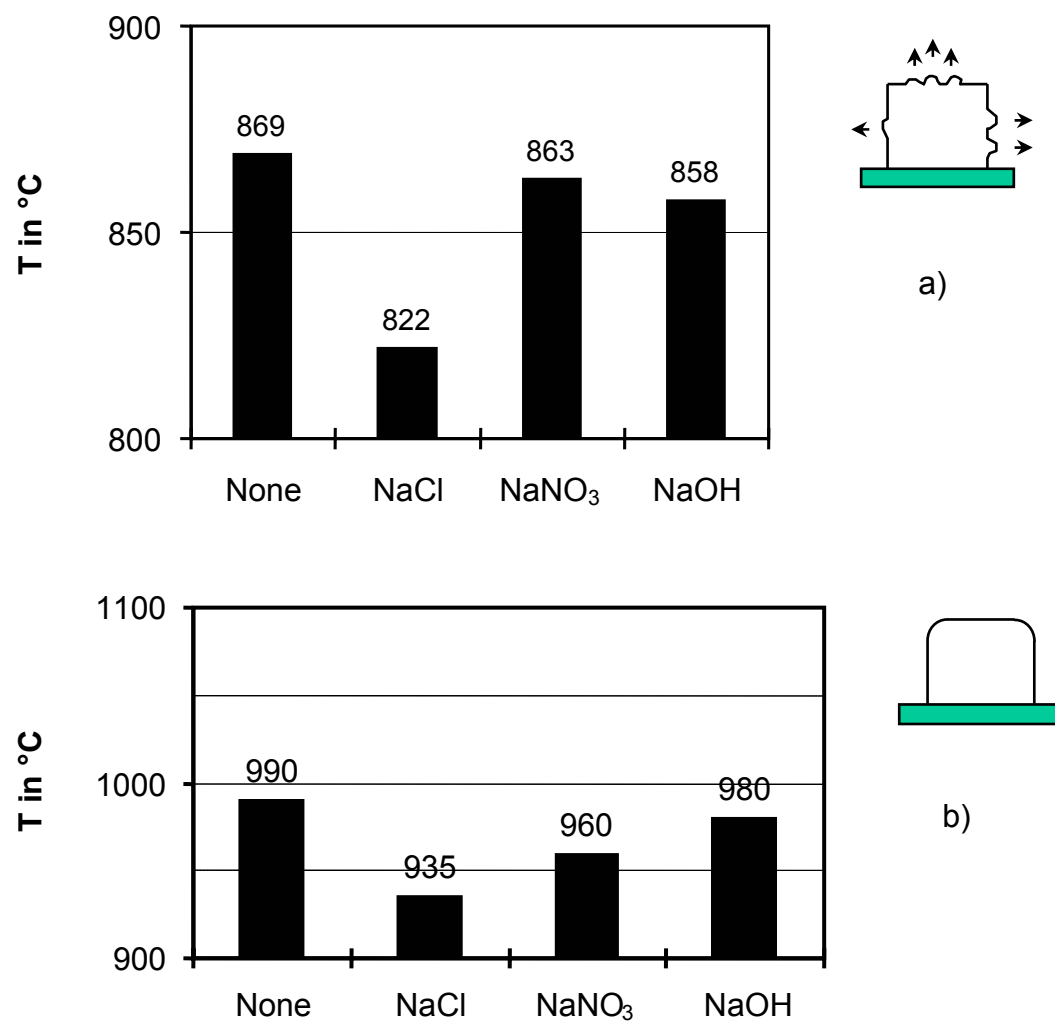


Fig. 58. Investigation of soda lime silicate glass with 1 wt. % additives showing an effect of a) gases release T1 and b) onset of melting T2

### 4.3.2 Extended use of heating microscope tests

#### a) Progress of gas release during the melting process

A new way to present the effect of gas release from a glass batch is developed. The gas release is calculated from the equation eq. (3.9) given in section 3.2.3.

Figure 59 illustrates the progress of gas release from 74-10-16 glass batches with additions of 1 wt. % NaCl, NaNO<sub>3</sub>, and NaOH as described in section 3.2.3. The sample was weighed before and after testing within an accuracy of 0.00001 mg. All tests were performed at the same conditions: heating rate 10 K/min to 1400 °C, no soaking time, CO<sub>2</sub> atmosphere 10 l/h, rapid cooling down to room temperature within 30 min. After testing, the residues of quartz and bubbles were inspected by optical light microscope and the progress of gas release was calculated. Comparing these results with the results obtained in figures 58 a-b, shows that an early onset of melting is not necessarily linked to an effective gas release. On the contrary, gases may be trapped in the system. In this study, NaNO<sub>3</sub> shows the most effective gas release, NaCl yields a minor improvement only. The most significant negative result is the protracted gas release with the NaOH containing batch. This should be a warning to the practitioner when considering a replacement of soda ash by caustic soda.

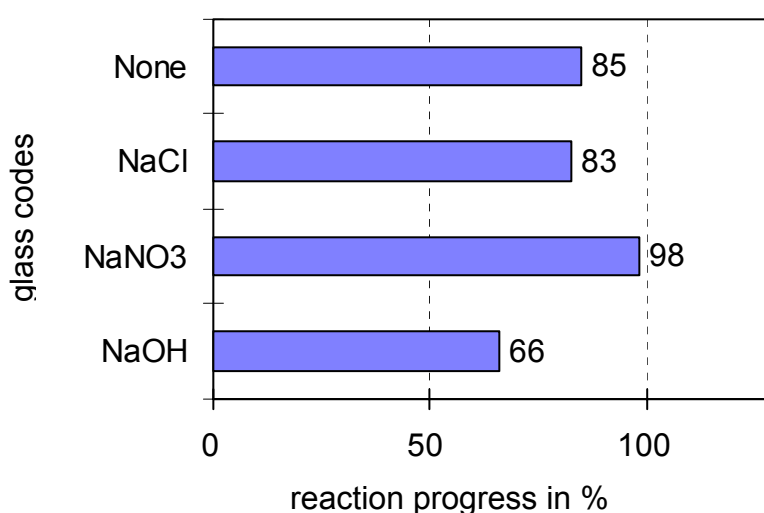


Fig. 59. Investigation of soda lime silicate glass added with 1 wt. % additives showing the progress of gas release

Further experiment was focused on the residues of sand grains and bubbles that remain in the melt. Tested samples from heating microscope were inspected by light microscope as shown in figure 60. Batch without any additive shows large remaining sand grains compared to smaller ones found in the batches with NaCl, NaOH, and NaNO<sub>3</sub>. Very small amounts of sand grains remained in the batch with NaNO<sub>3</sub>. The highest amount of remaining bubbles was found in the batch containing 1 wt. % NaOH, while the batches with 1 wt. % NaCl and without any additive showed medium bubbles contents. This is in agreement with the mass losses shown in figure 59. Table 16 shows the results of a count of the residual bubbles.

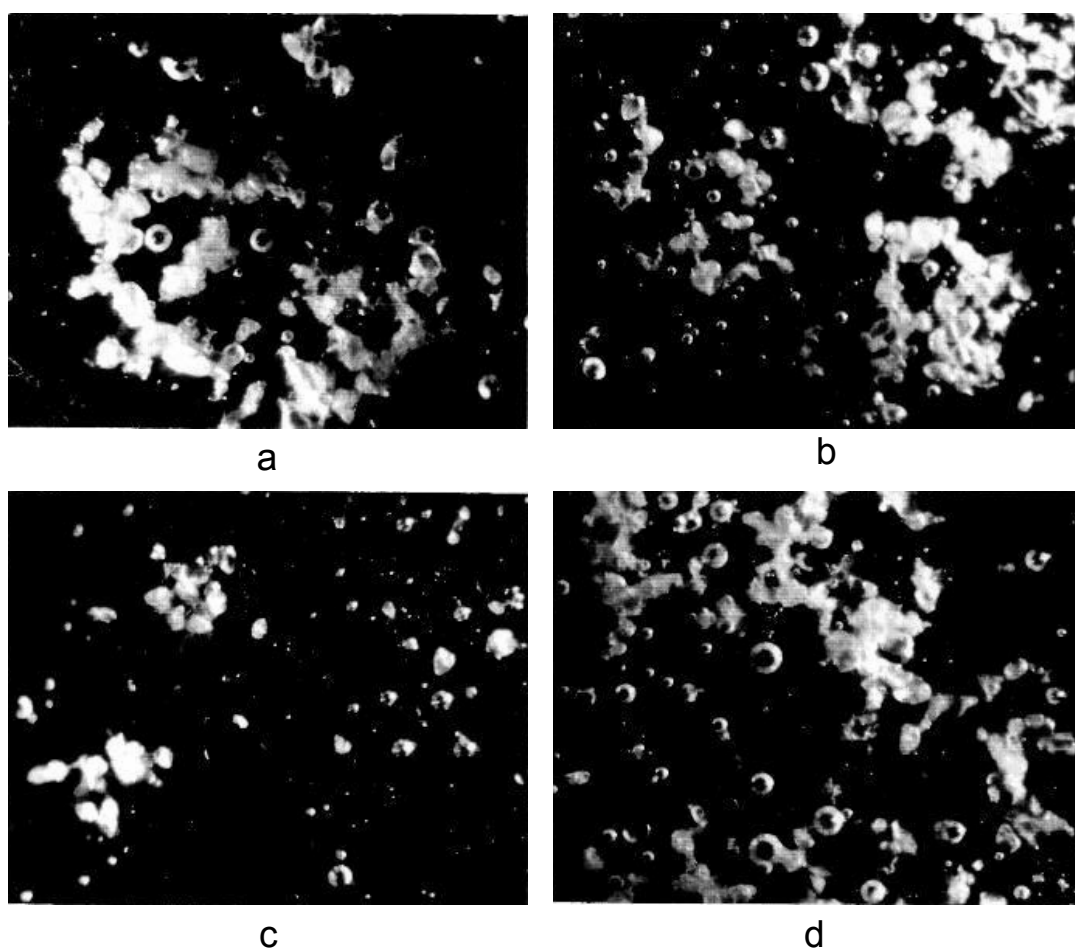


Fig. 60. Residual sand grains and remaining bubbles in the melt observed from light microscope of soda lime silicate glass added with 1 wt. % of a) no additive, b) NaCl, c) NaNO<sub>3</sub>, and d) NaOH

Table 16. Bubble quantities and sizes determined from light microscope

batches	bubble size big ( $> 90 \mu\text{m}$ )	bubbles size small ( $< 30 \mu\text{m}$ )	total
no additive	47	200	247
+ NaCl	73	180	253
+ NaNO <sub>3</sub>	39	140	179
+ NaOH	64	230	294

From table 16, it should be noted that NaNO<sub>3</sub> is best additive with respect to both big and small bubbles, NaCl helps in that the amount is shifted towards larger bubbles, which may easily escape by buoyancy. Again, NaOH is very unfavorable with a high amount especially of small bubbles.

#### a) Reactions by grain-to-grain contact

Soda-lime, soda-dolomite, soda-phonolite, and soda-cullet (container flint 2, container green, and amber glasses) combinations were investigated by heating microscope in air (no flow) and CO<sub>2</sub> atmospheres at a flow rate of 10 l/h and a heating rate 10 K/min. A combination denotes two individual grains being put into physical contact and observed in the heating microscope. As can be seen from figures 61 and 62, soda ash started to visibly react with silica sand at 866 °C, combined into one grain at 868 °C, formed a new phase at 954 °C and reached a complete melt at 1085 °C. Soda and lime started to react at 797 °C, formed a single array at 822 °C (soda and limestone attract each other!), and completely melted at 827 °C. The reaction between soda ash and dolomite started at 867 °C. Dolomite repels soda as not to form a physical contact. Dolomite after its first decomposition, composition step, however, sucks the soda ash to its side to form a new phase. But melting is not completed even at 1300 °C. Phonolite pulls the soda ash to form a liquid phase; it starts to react at 869 °C and reaches the final state at 1173 °C. Likewise, the cullet tends to pull the soda ash as soon as it melts. Their physical contacts begins at 866 °C and reaches a final stage at around 930-960 °C. Figure 63 is added to explain why the physical melting of soda ash is sensitive to the surrounding atmosphere. Even a minor

decomposition of  $\text{Na}_2\text{CO}_3$  yields a significant reduction of the liquidus temperature ( $\text{Na}_2\text{CO}_3\text{-Na}_2\text{O}$  melt). Single component tests of soda ash and phonolite were investigated by heating microscope under air and  $\text{CO}_2$  atmospheres at a flow rate of 10 l/h and heating rate 10 K/min. It could be seen that sintering of soda ash in air has much lower melting rate than sintering in  $\text{CO}_2$  atmosphere ( $\sim 100\text{-}200$  °C, see figure 64), due to the lower oxygen partial pressure of the sintering system. For the phonolite, it showed a much higher sintering temperature one.

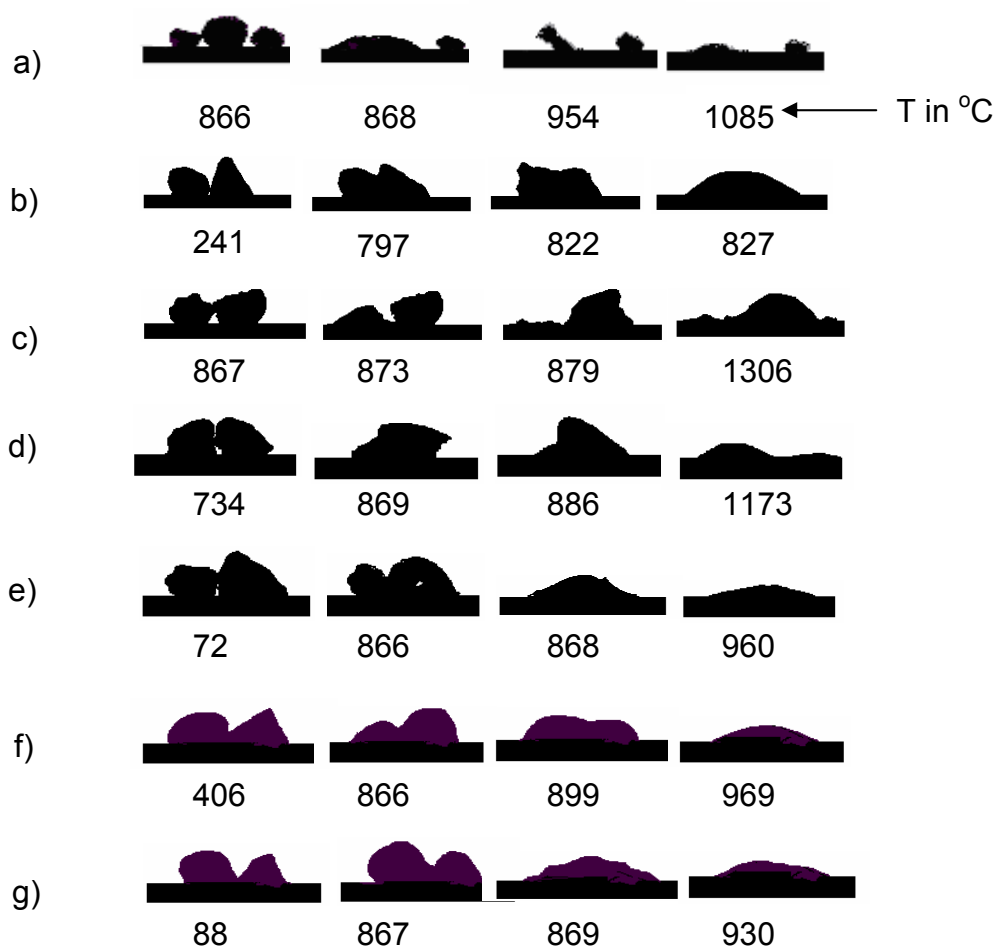


Fig. 61. Investigation by heating microscope under a flow  $\text{CO}_2$  at 10 l/h of a) soda-sand, b) soda-lime, c) soda-dolomite, d) soda-phonolite, e) soda-amber cullet, f) soda-container green cullet, and g) soda-container flint 2 cullet

From the investigations, shown in figures 61 and 64 it can be concluded that the reaction between soda ash and limestone occurs at the lowest temperature, followed by soda-phonolite, soda-cullet, and soda-

dolomite. Anyway, all reactions start with the physical melting of the soda ash. This physical melting occurs, however, earlier in air than in CO<sub>2</sub> atmosphere (figure 64), which is in agreement with figure 63.

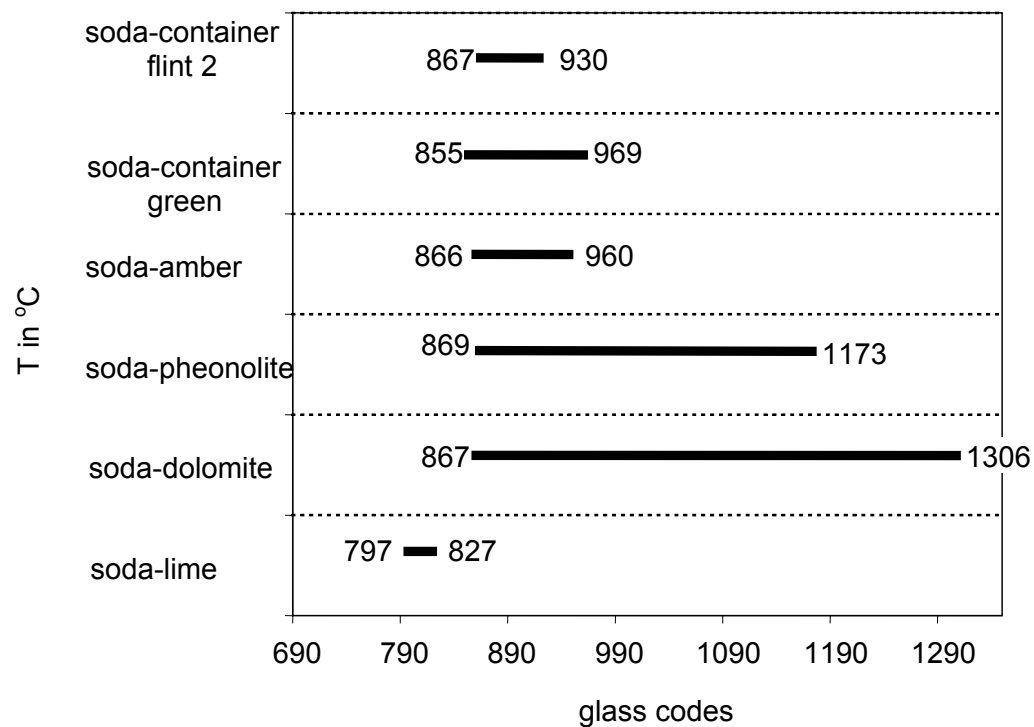


Fig. 62. Investigation of the results from fig. 61, plotted of T1 and complete melting temperature



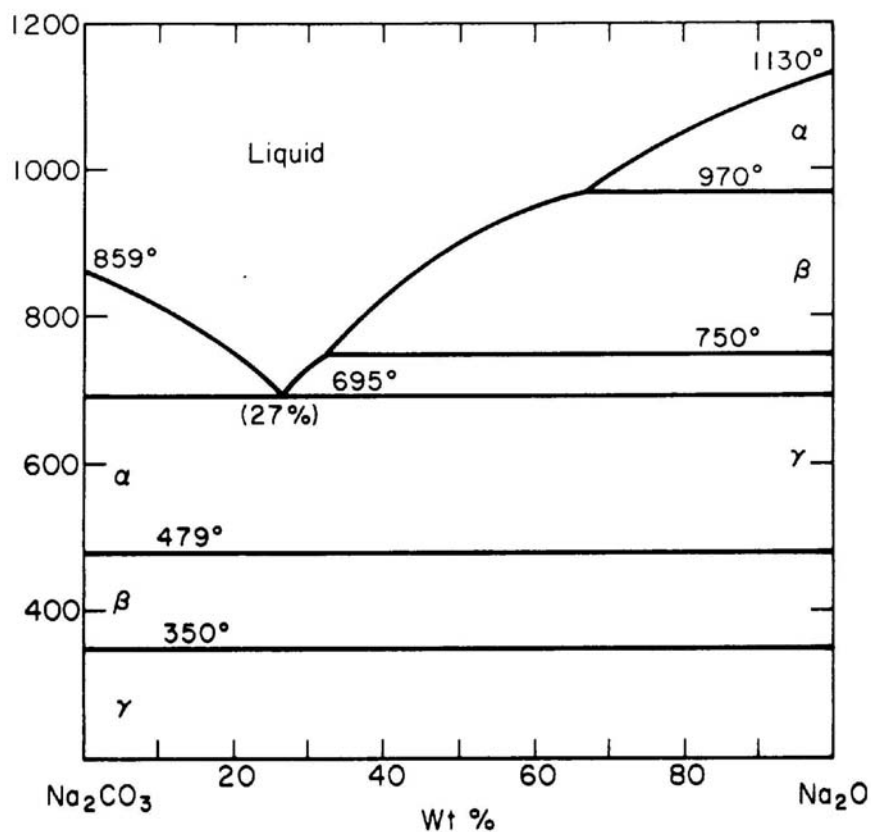


Fig. 63. Phase diagram of Na<sub>2</sub>O-Na<sub>2</sub>CO<sub>3</sub>

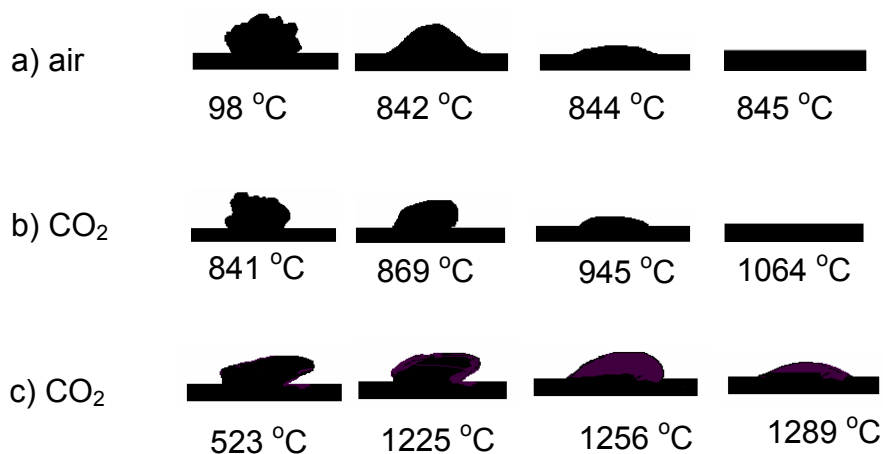


Fig. 64. Investigation of soda ash (a, b) and phonolite (c) in a flow of gases at 10 l/h

As a further conclusion, the observations displayed in figure 61 support the finding by practitioners that cullet “eats” the soda ash, i.e., consumes it on expense of the soda-ash reaction, and that phonolite does the same thing. This has also been found by [70].

## 4.4 Batch free time (BFT) experiments

Two different types of furnace; one from GHI and another one from Schott Glass GmbH were used. In evaluating the batch free time experiments, the crucibles were firstly loaded with 150 g of cullet, preheated to 900 °C in an electrical furnace, and raised to  $1400 \pm 10$  °C. Then, 86 g of batch was quickly charged on top of the established cullet melt in the crucible.

Five different batches of S1-S5 were used to perform the testes at GHI furnace. S1 refers to a crystal glass and S2 represents a container flint 1 glass. S3, S4, and S5 are sodium silicate glasses at Si:Na = 2.05, 3.3, and 3.4 respectively (see compositions in section 3.2.4, tables 11 and 12). Different tests were performed which were interrupted after 10, 20, 30 minutes for crystal glass. For sodium silicate glasses, the tests with duration of 50 and 80 min were performed and for container flint 1 glass, the time was additionally extended to 100 min. The melting of the batch was recorded by a video camera. After tested, the crucibles were extracted from the hot furnace and tempered for 2 h. After that, the samples were vertically cut and visually evaluated. The residual crystalline phases were inspected by light microscope from the sample of 1.5 mm thick.

For the tests at Schott Co. in silica tube furnace, only 74-10-16 glass batch was performed. The cullet were firstly heated up slowly at 10 K/min to 1500 °C for 30 min in silica tube. After that glass batch was charged on top of the melt and an on-line VDO recorder was record the batch melting reaction.

### 4.4.1 Tests at GHI

Much time was invested to improve the batch free time measurement. It was found that glass melting can be observed only 4-5 min in the early stage, when no optical manipulations are performed. Then the intense heat radiation veils all other effects. The use of a high pass filter for short wavelengths between 250-400 nm combined with a 70 W halogen lamp was mandatory for a successful observation. But even before the batch free time, some meaningful events were observed: This is the time at which all solid islands disappeared under a layer of foam.

From the tests, the time at which all solid islands disappeared was found to be: 132 s for crystal glass, 309 s for container flint 1 glass, 223, 267, and 244 s for sodium silicate glasses at Si:Na ratios of 2.05, 3.3, and 3.4 respectively. It was also found that the reaction behavior of container flint 1 was much slower than crystal glass. Figure 65 shows the reaction progress as: start of reaction time ( $t_1$ ), time of visible solid islands ( $t_2$ ), and time when the solid islands disappeared ( $t_3$ ). The reactions began within a few seconds after the glass batch was charged on top of the molten cullet melt and the reactions started from the edge to the middle of the crucible. However, this is still not enough to determine whether > 99 % of batch had disappeared under the glass melt.

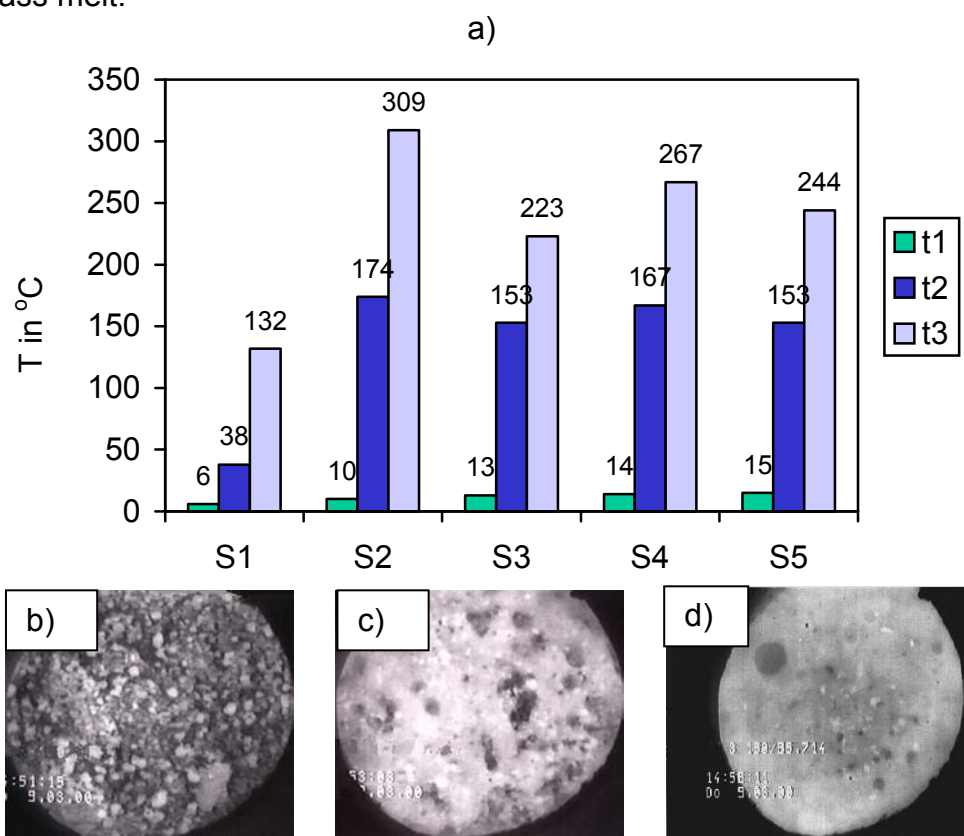


Fig. 65. Progress of glass batch melting, initial stage, as observed in a batch free time observation furnace at GHI at times  $t_1$ ,  $t_2$ , and  $t_3$  a); batch reactions detected by online video camera after charging of sodium silicate batch (S3) on molten cullet at 1400 °C for 13 s b), 153 s c), and 223 s d), which represent the stages  $t_1$ ,  $t_2$ , and  $t_3$ , respectively;  $t$  in second

Figure 66 shows the light microscopic images of sodium silicate glass batch (S4) at Si:Na ratio of 3.3. An observation of residual crystalline phases, bubbles, and seeds from 1.5 mm thick slices is shown (for the sample preparation see figure 68). A bulk of remaining crystalline phases still remains at the melted surface after 10 min (figure 66 a). Many bubbles and seeds are observed both in a rough melted batch layer and in the lower part of the melt. After 20 min (figure 66 b), less crystalline grains, bubbles, and seeds are found; they do not disappear even after 50 min (figure 66 c). After 80 min, all remaining grains are dissolved in the glass melt, but some tiny bubble still remain (figure 66 d).

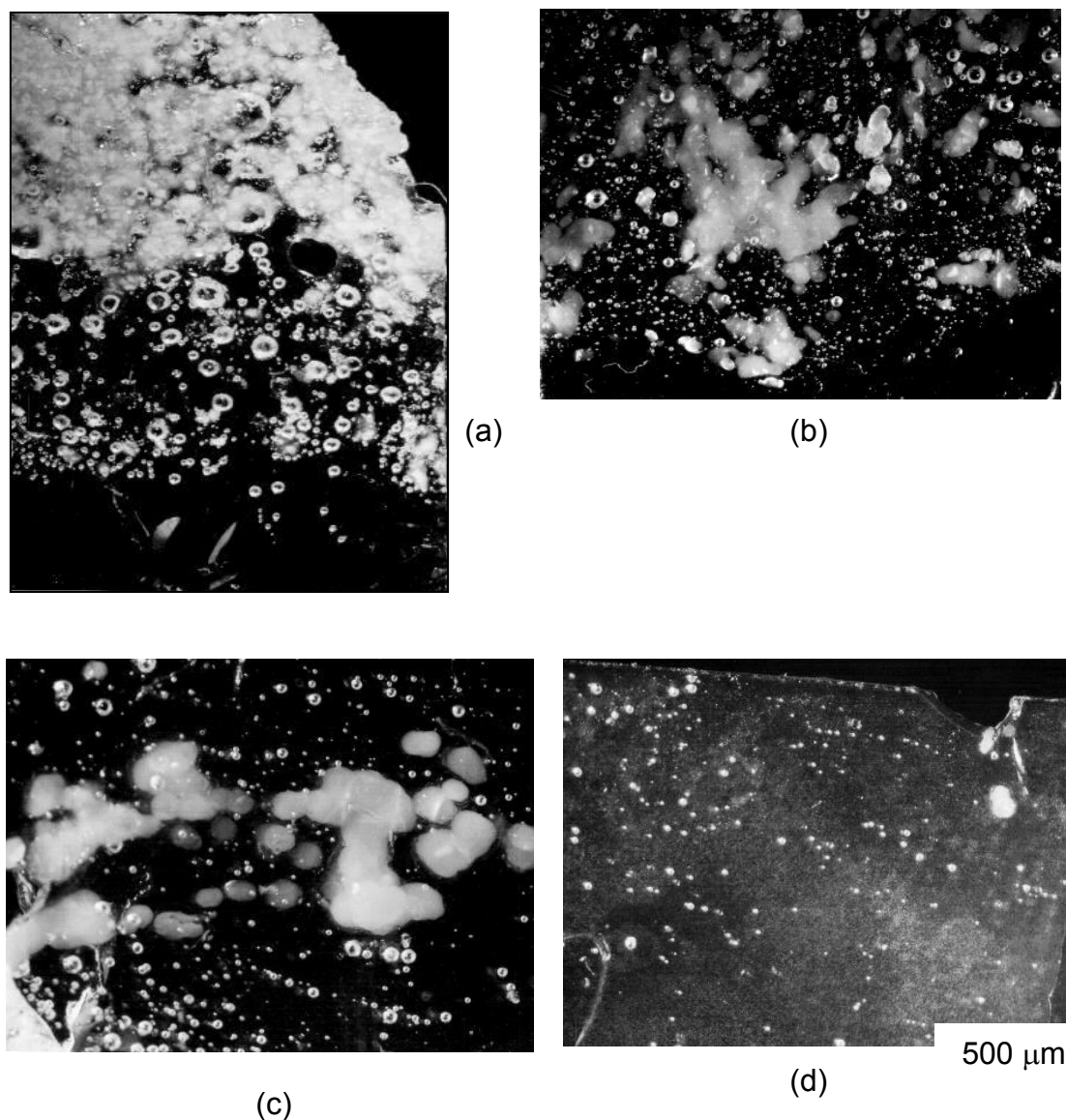


Fig. 66. Residual crystalline phases in glass S4 after a) 10 min, b) 20 min, c) 50 min, and d) 80 min

Figure 67 shows molten glasses in crucibles a) and a vertically cut and visually evaluated for all investigated glasses b). From these cuts, slices were prepared for microscopic inspection.

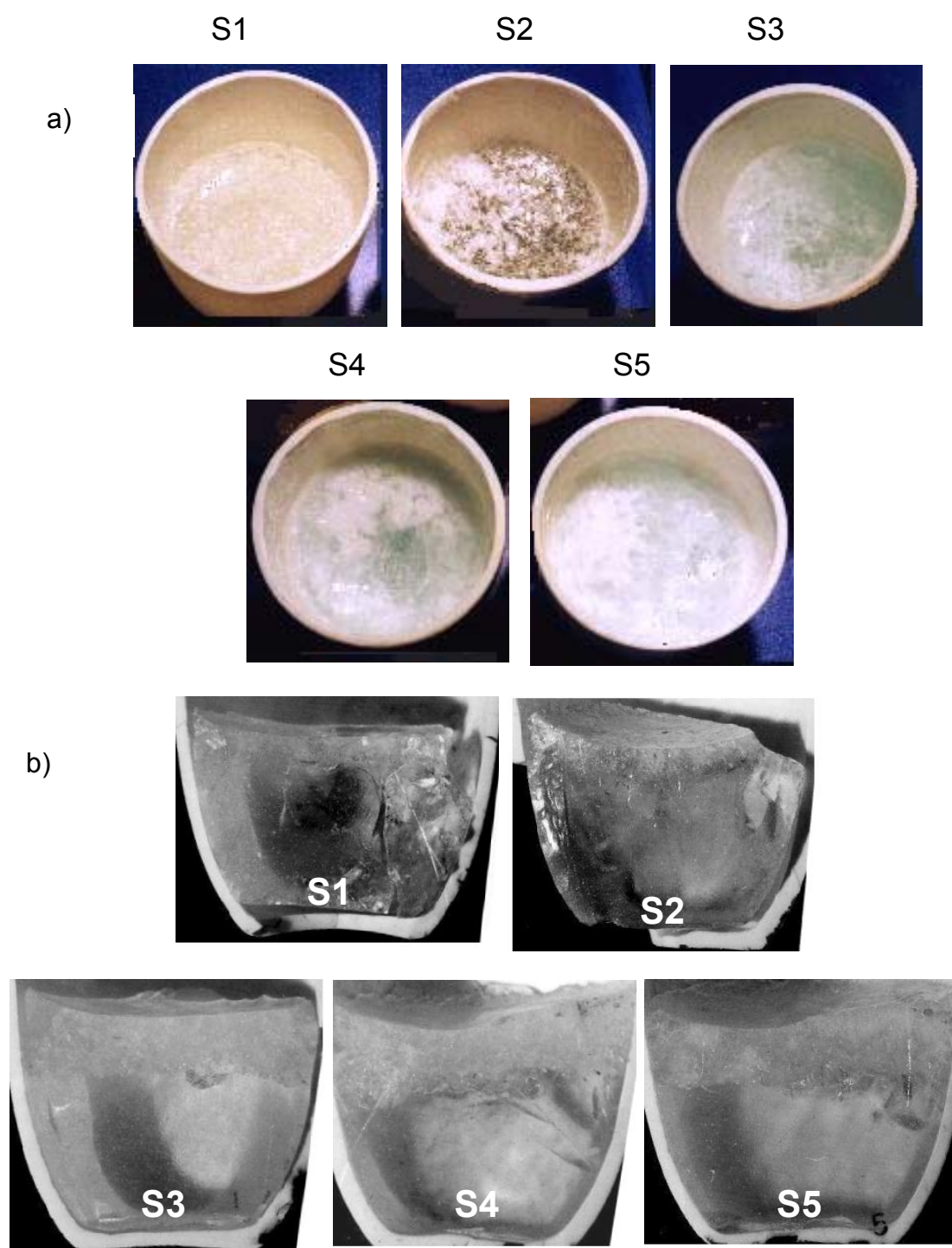


Fig. 67. Photographs of all batches melted at 1400 °C for 30 min, a) top view and b) vertical sections; S1: crystal glass, S2: flint glass, S3 to S5: sodium silicate glasses (water glasses)

Sodium silicate melts have a slightly green color with a degree of  $S_3 > S_4 > S_5$  and assume a white color in the sequence of  $S_3 < S_4 < S_5$ .

Further evaluation of the residual crystalline phases was performed with all samples illustrated in figure 67 b. It was found that high residual crystalline phases in glass located at the edge of the crucible (see figure 68). The remaining rough melted layers (measured in cm) at the middle of the crucible ( $batch_{middle}$ ), a height of the overall melt (include cullet) at the left corner ( $h_{left}$ ), in the middle ( $h_{middle}$ ), and at the right corner ( $h_{right}$ ) are summarized in table 17. The thinnest layers were observed in crystal glass and white container flint 1 glass batches.

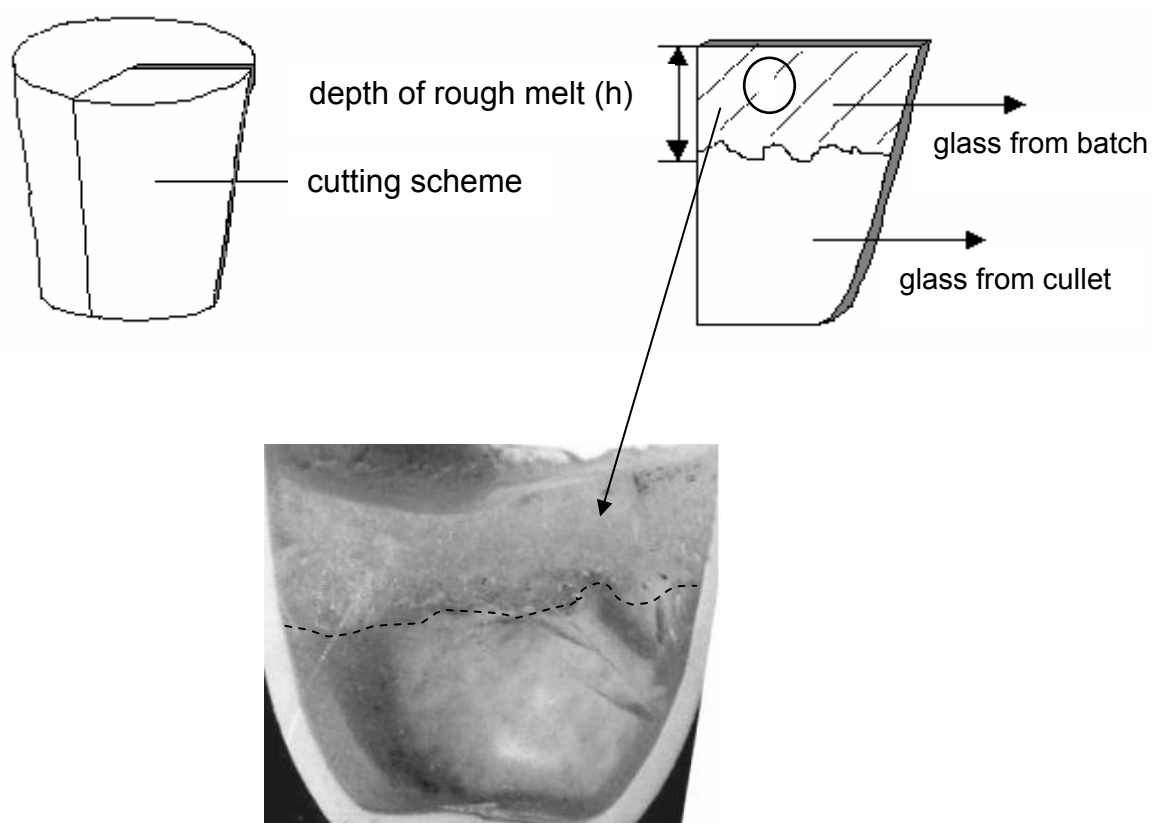


Fig. 68. Illustration of region with high crystalline phase content

Table 17. Height of remaining rough melt layers ( $h_{\text{left}}$ ,  $h_{\text{middle}}$ , and  $h_{\text{right}}$ ) and remaining batch layers above cullet melt ( $\text{batch}_{\text{middle}}$ ) in cm after 30 min

batches	$h_{\text{left}}$	$h_{\text{middle}}$	$h_{\text{right}}$	$\text{batch}_{\text{middle}}$ (h)
S1	3.45	3.40	3.45	0.5
S2	3.90	3.75	3.90	0.7
S3	4.20	4.10	4.10	1.1
S4	4.10	4.10	4.60	1.1
S5	4.10	3.95	4.35	1.1

#### 4.4.2 Tests at SCHOTT Co.

Soda lime silicate glass batch was also investigated by a batch free time method using a silica tube observation furnace at SCHOTT Co. The furnace itself can be operated at heating rates from 1 to 150 K/min with a temperature maximum of 1600 °C. In this experiment, the cullet were firstly heated up slowly at 10 K/min to 1500 °C for 30 min. After this, the glass batch was charged on top of the melt and an on-line VDO recorder was used to record the batch melting reactions.

Figure 69 illustrates the melting progress observed from the silica tube furnace. It is clearly seen that after charging the batch blanket onto cullet melt, the reaction starts at the contact zone and progresses deeply into the batch blanket. The batch sinks under the clear zone of the cullet level; foaming begins. Some large bubbles are formed and trapped under the melt. After 2 min, most of the raw materials are lifted up by foam formed during melting. It takes around 4 min to dissolve all raw materials. At this state, the diameter of foam bubbles decreases. The height of the foam forming is around 150 % higher than the thickness of the original batch blanket. After 10 min, the foam level decreases dramatically and remains constant after 25 min. At this state, small bubbles are still released from the bottom of the melt to the top. After 54 min, the sample was taken from the furnace and visually inspected. No batch residues were found.

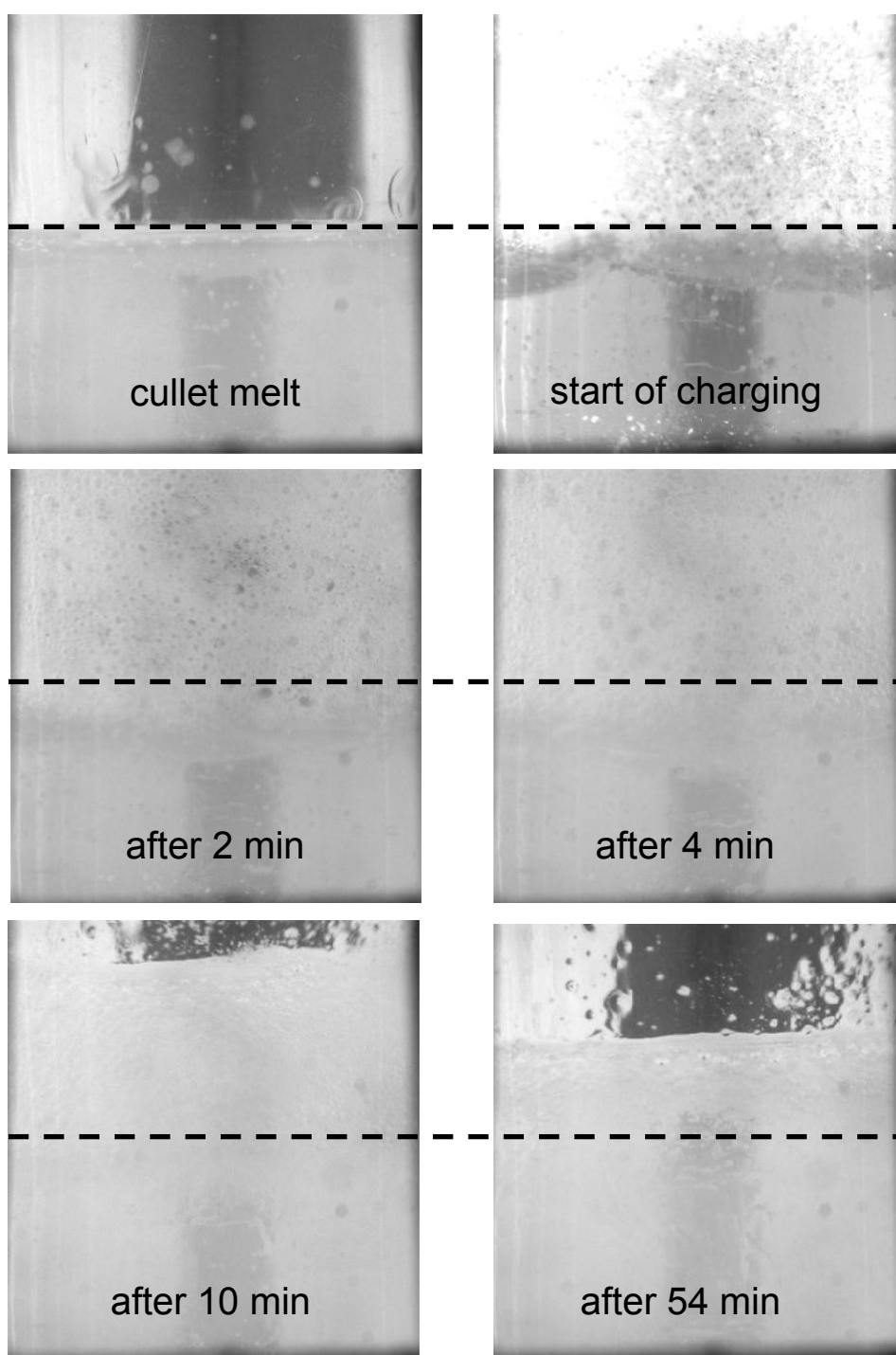


Fig. 69. Sequence of a soda lime silicate glass batch charged on top of a cullet melted at 1550 °C, dotted line indicates the initial level of the cullet melt



## 4.5 Mass loss measurements (50 g scale)

As mentioned before in section 3.2 and 3.2.5, the mass loss of materials is conventionally measured by thermogravimetric analysis (TGA), however, within the limit of typically only 250 mg. TGA samples should be mixtures of finely ground powders. For industrial glass batches, large mass fractions of grains bigger than 0.5 mm are typical. Samples of 250 mg taken from such batches have very little chance of being representative. Even worse, the strong influence of grain-to-wall contact in the tiny sample compartments yields effects which never occur in a large scale situation, hence, must be considered as experimental artifacts.

Therefore a new concept of weight loss determination by a tube furnace integrated with on-line mass loss signal detection from a balance ( $\pm 0.001$  mg) was constructed. By this method, it was possible to measure batches up to 200 g. The method was only initiated during this thesis. The development to maturity is left to further researchers.

### 4.5.1 System calibration

The system was calibrated by measuring the mass loss of limestone and dolomite. No thermocouple was immersed into the batch in order not to disturb the weight measurement. Therefore, a separate measurement of mass loss and batch temperature was performed. Figures 70-72 show smooth signals of mass loss from limestone and dolomite that match well with theoretical mass loss (figure 70). Limestone showed a mass loss of 42.5 wt. % compared to a theoretical loss of 43.97 wt. %, while commercial grade dolomite showed a mass loss of 45.8 wt. % compared to theoretical loss of 47.73 wt. %.

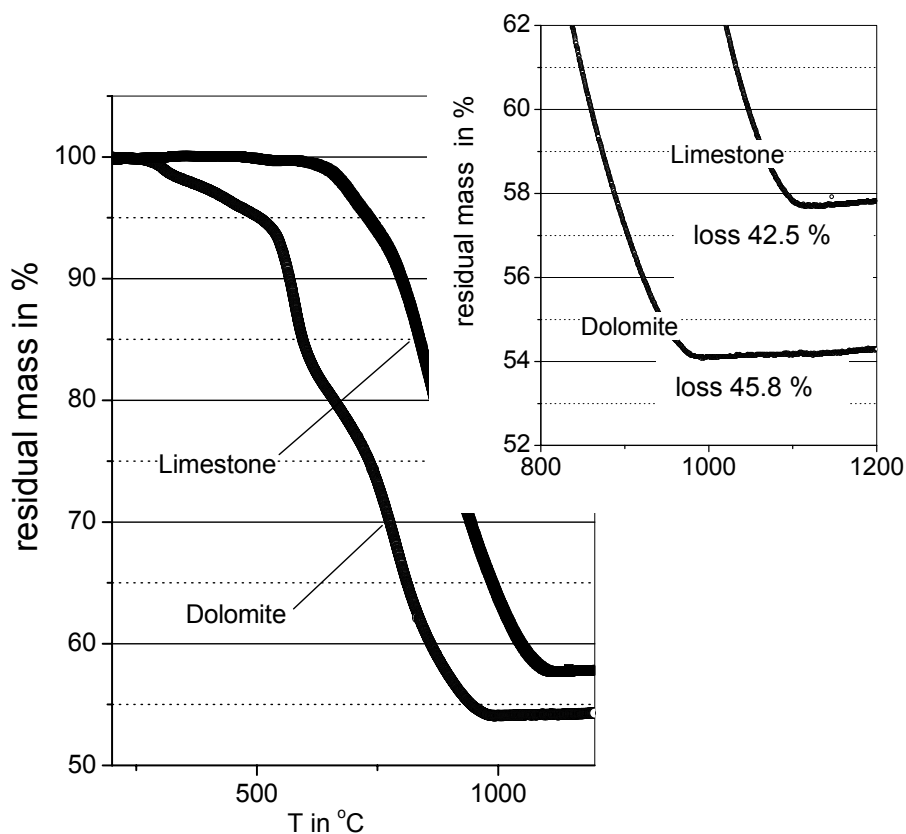


Fig. 70. Mass loss calibration by limestone and dolomite showing a good match with theoretical mass loss

Figure 71 shows the mass loss of the commercial grade limestone detected from the vertical tube furnace compared with the loss accurately measured by TGA. The tube furnace gives a more realistic account of the decomposition rate of a commercial grade material: the decomposition starts earlier and terminates later than in the TGA experiment. Beyond this, the mass loss in the tube furnace is a little bit higher, probably due to a certain amount of particulate loss.

Figure 72 also shows the comparison of the measurement between the two systems by using dolomite. Similar behaviors were observed.

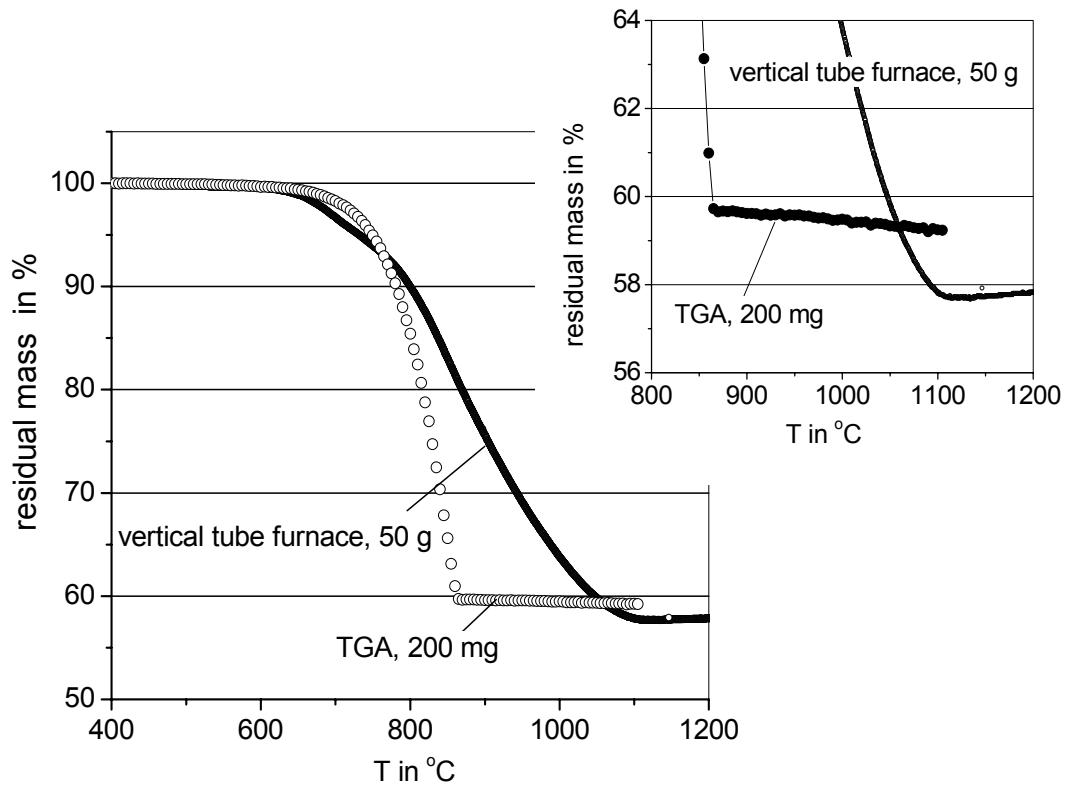


Fig. 71. Mass loss of limestone, a comparison between TGA and the vertical tube furnace 200 g balance

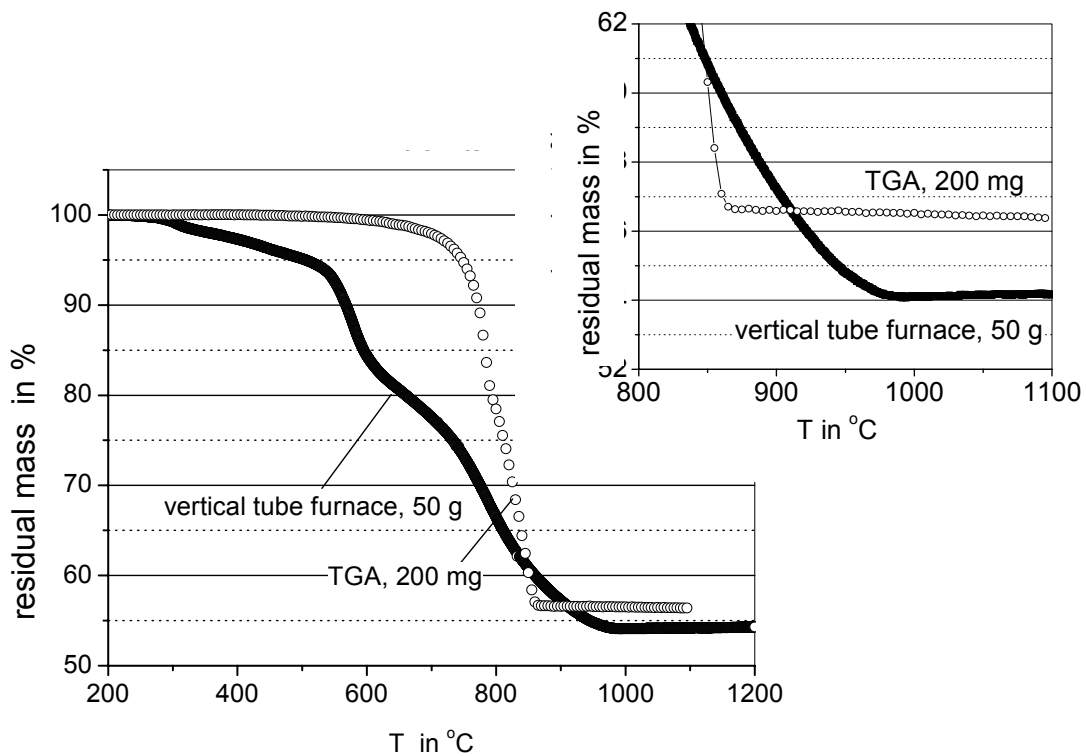


Fig. 72. Mass loss of dolomite, a comparison between TGA and the vertical tube furnace 200 g balance

### 4.5.2 Measurement of 50 g batches

After calibration, mass loss of sodium silicate (S3) and container flint 1 (S2) batches (50 g) were measured as shown in figures 73 and 74. Mass loss detected from TGA of both tests began faster and completed earlier than mass loss from vertical tube furnace, however, at a similar amount of total weight loss. The newly designed measuring system suitable for batches up to 200 g gives the possibility to measure mass loss of industrial grade batches in a way more realistic for practical application than conventional TGA.

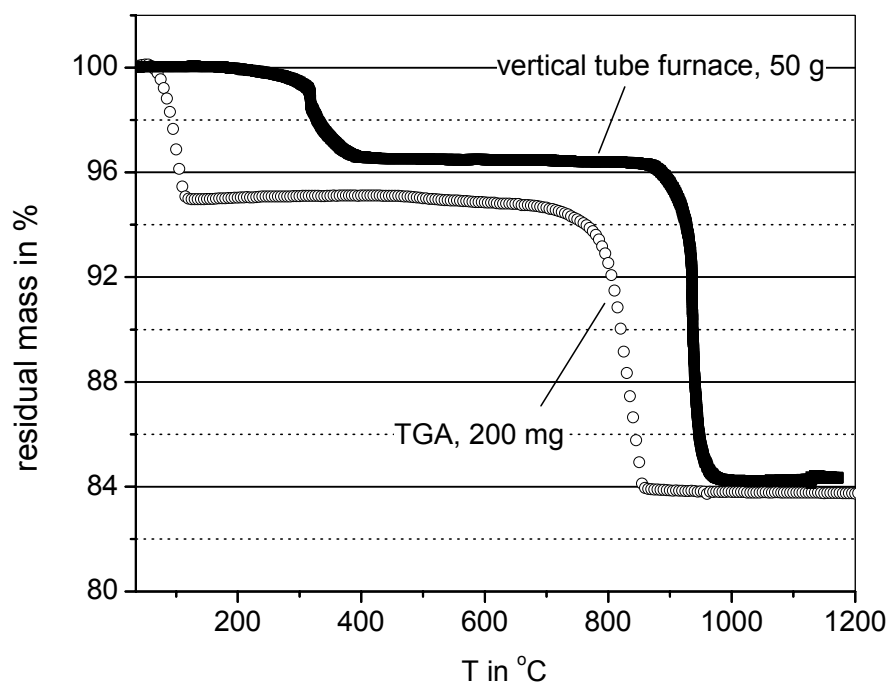


Fig. 73. Mass loss of soda sand batch (S3) measured from 50 g batch compared to mass loss detected from TGA (25 mg)

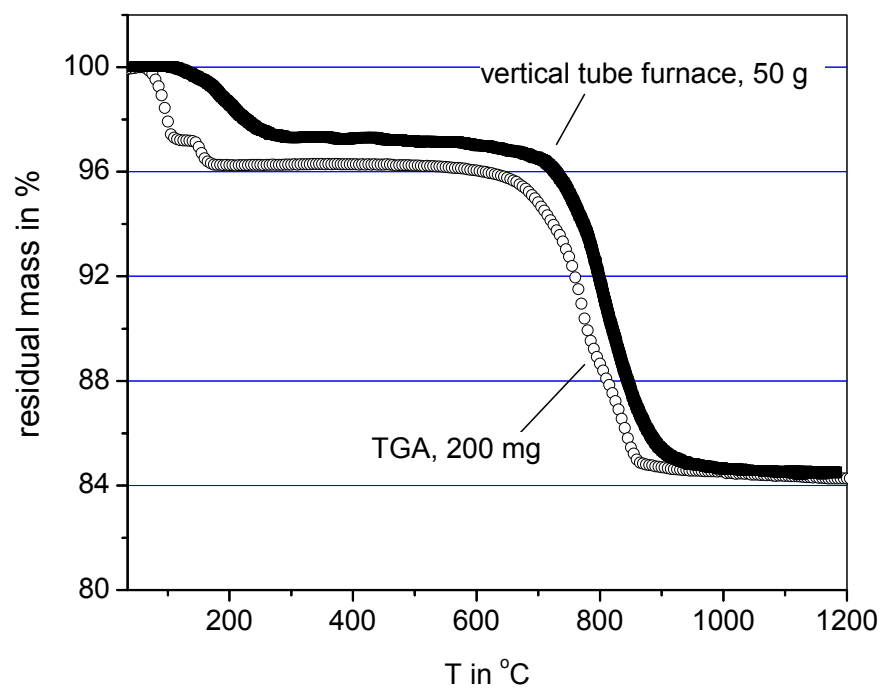


Fig. 74. Mass loss of container flint 1 batch (S2, 50 g) compared to mass loss detected from TGA (25 mg)

## Chapter 5

### Conclusions

A number of unconventional methods suitable for the characterization of industrial grade glass batches was developed, contributed, and tested against a number of different batches, and sub-systems of batches. The development of such methods was necessary as the conventional methods like DTA, TGA, DSC, XRD, etc, all refer to small and finely ground samples. The small sample sizes involved in all of these methods (typically 250 mg) are a severe limitation. These conventional methods work best with well-mixed fine powders. But this is a very unusual situation for industrial glass batches. In such batches, large mass fractions of grains bigger than 0.5 mm are found. Samples of 250 mg taken from such batches have very little chance of being representative. Even worse, the strong influence of grain-to-wall contact in the tiny sample compartments yields effects which never occur in a large scale situation.

In view of this situation, a major part of research efforts was devoted to the development of new experimental methods suitable for the investigation of batch melting, which are; 1) conductometry, 2) thermal diffusivity, 3) heating microscope, 4) batch free time (BFT), and 5) mass loss. Those newly established methods were applied to batches typical of industrial mass glasses, and to one- two- and three-component sub-systems of such batches, in order to identify the key mechanisms of batch melting. In doing this, the effects of heating rate, particle size, cullet additions and melt accelerants were investigated. The methods supplemented by conventional DTA, TGA, and DSC. Introducing these methods does not mean to reject conventional methods. The latter ones are rather used to accurately determine the role of local chemistry.

## 5.1 Conductometry

For development of a melting onset measurement, an electrical box furnace was constructed by a light weight alumina brick using silicon carbide as heating elements. A digital temperature controller was used to control the furnace temperature to maximum temperature of 1200 °C. The signals from sensors and thermocouple were recorded on-line. The resistivity of the material was determined by the voltage drop across the sensor by a voltage divider circuit. The local conductivity  $\kappa$  in  $(\text{ohm}\cdot\text{cm})^{-1}$  was derived from the voltage drop. The samples (200 g) were loaded into a crucible and exposed to the furnace. The conductivity and temperature probe was placed in the middle of the crucible. The immersion depth was approximately 4 cm in the batch. The probe was connected to a computer which recorded both voltage drop and temperature of the batch, and the temperature of the furnace, in intervals time of 1 s.

Soda ash was firstly used to determine the accuracy of the system. A good accuracy of crystal water release of soda ash monohydrate at  $104 \pm 1$  °C and the melting peak at 855 °C from soda ash was found. Furthermore the quartz inversion temperature was observed precisely at 573 °C. After that, binary, ternary, and multi-components mixtures were investigated.

In order to continue measurement beyond the conductivity, the circuit was modified and the test was continued at constant temperature by increasing time 30 minutes compare to that of previous work. In this region, the batch became liquid and showed a strong reaction with Ni-Cr-Ni sensor. So, Pt sensors were used instead.

With the help of this sensor, the melting progress can be characterized in terms of the ways: The first one is a “DTA” signal. It is the plot of batch temperature as x-axis and the signal calculated from batch temperature minus furnace temperature as y-axis. The second one is the “voltage drop” signal. The signal detected from the conductivity probe is plotted with batch temperature. The last one is the electrical conductivity signal. In this case, the calculation of  $\log \kappa$  ( $\kappa$  = electrical conductivity in  $(\text{ohm}\cdot\text{cm})^{-1}$ ) is plotted with  $1/T$

( $T$  = temperature in K). By doing the electrical conductivity plot, the foaming reaction region is detected, too.

For the binary system, four systems with two components; soda-sand, soda-limestone, soda-dolomite, and soda-phonolite were tested.

Mixed soda-sand shows a well clearly strong reaction detected between 800-1000 °C, which represent the meta- or di-silicate formations. Further studies of mixed sand and soda at different ratios of 50:50, 60:40, 70:30, 80:20 and 90:10 were also performed. The voltage drop began at high temperature for less soda content and decrease dramatically with increasing of soda content. At above 30 wt. % soda ash, a grain to grain contact reaction occurred. The plot of electrical conductivity with  $1/T$  of mixed sand-soda at different ratios of 10:90 to 90:10 shows a similar effect as voltage drop signals. Another aspect of the mixture between sand and soda was focused on variation of sand grains of 335-500  $\mu\text{m}$ , 185-200  $\mu\text{m}$ , and <40  $\mu\text{m}$ . For the coarse fractions, electrical conductivity exhibits a more or less steady decrease between 300 and 800 °C, which is due to the increasing solid state mobility of the  $\text{Na}^+$  ion. For increasingly finer fractions, this tendency is superimposed by a reaction immobilizing the  $\text{Na}^+$  again. The reaction is strongest between 600 and 750 °C.

For the mixture of soda ash and limestone, the cross-over temperature (increasing of electrical conductivity) began at 358 °C. This reaction also found to have an effect by slowing down weight loss found in DTGA experiments [6-7]. It has, however, lower first melt formation detected at 720 °C compare to the eutectic point of  $\text{Na}_2\text{CO}_3$ - $\text{Na}_2\text{Ca}(\text{CO}_3)_2$  at 785 °C. After first melt formation was reached, a fluctuation of the foam formation signal was quite high in the temperature range of 700-1050 °C due to the high amount of gas release from both soda ash and limestone.

Electrical conductivity of the mixture between soda ash and dolomite shows strong reaction peak (DTA signal) between 550-1000 °C (figure 44) and low primary melt formation temperature at 681 °C, which is closed to the decomposition peak detected by [45] at 680 °C.

For the mixture of soda-phonolite, it shows only a little lower first liquid formation, slightly lower electrical conductivity, and longer time consume for foam formation. One interesting thing was observed here: The crucible was



empty after the test. The soda-phonolite reaction is very violent. The melt literally jump out of the crucible.

For ternary mixtures, two significant effects can be seen in this experiment. Firstly, foam formation of the mixture between soda-sand-phonolite is less than soda-sand-lime and soda-sand-dolomite. These three systems have relatively similar electrical conductivity values. However, a slightly higher value could be detected in soda-sand-dolomite system. Secondly, the signals of three-component systems appear in between that of the two binary systems containing sand. For example, in soda-sand-dolomite, the first melt formation, electrical conductivity, and DTA signals appear between the signals of soda-sand and soda-dolomite.

In multi components tests, six different glass batches were investigated and found that their electrical conductivity signals are more complex than the former results. This is because they have more complex reactions than two or three components systems. Due to higher fluxing content, crystal glass shows the lowest primary melt formation with a slightly higher electrical conductivity than container flint<sup>1</sup>. Second test of multi components mixtures was focus on an effect of coal in 74-10-16 glass batches. Additions of 0.5 and 2 wt. % coal into glass batches were performed. They show a lower electrical conductivity at higher coal content and took longer time in order to bring temperature of the system equal to the batch containing 0.5 wt. % coal. Electrical conductivity of glass batch 74-10-16 was also performed under flowing of CO<sub>2</sub> at 10 l/h, and H<sub>2</sub>O:N<sub>2</sub> (50:50) at 56 l/h. Both tests have similar electrical conductivity, however, tested under flowing of H<sub>2</sub>O can accelerate the cross over reaction time and slightly lower primary melt formation.

The following two pictures summarize and present the power of the new tool. The graph was established by [70], a colleague using the methods developed here for his own investigations on melting complex industrial batches.

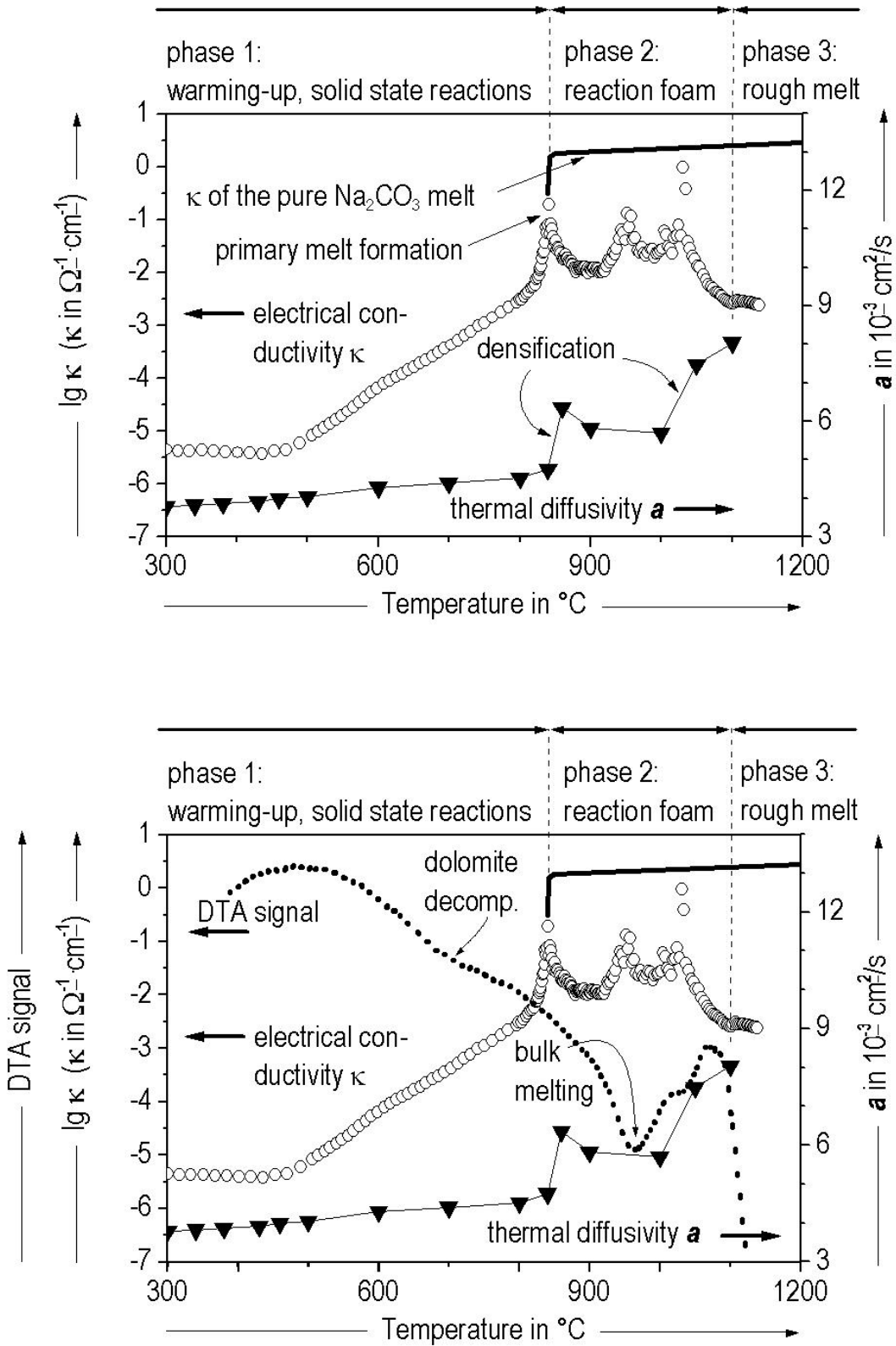


Fig. 75. Plot of electrical conductivity and thermal diffusivity of white glass [70]

## 5.2 Thermal diffusivity

Before the establishment of the new sensor, the thermal diffusivity of batches had to be determined from the temporal and local derivative of the measured temperature field in the batch using Fourier's law. This is a very imprecise method, because chemical reactions distort the temperature field during the whole melting process. To develop a new measuring concept of thermal diffusivity, a similar measuring system as melting onset was applied, but the new sensor need was equipped with a heat source. The heating coil was made by 0.2 mm thick Ni wire connected to a 1 mm thick Kanthal wire. The Kanthal wire was connected to a voltage source (10 V AC) triggered by a computer bus, generating a heat pulse every 150 seconds. The thermal diffusivity was determined by evaluating the run time of heat pulses (< 5 K temperature difference at the receptor thermocouple) across a distance of 1 cm. The precision reached is approximately  $\pm 5 \cdot 10^{-4} \text{ cm}^2/\text{s}$ . The way of application in the batch is the same as described in section 5.1.

A typical signal is obtained from the difference between the average batch temperature  $T^*$  and the instant batch temperature  $T_b$ . From the thermal diffusivity experiments, data were collected, and evaluated for 100 K ranges between 300 and 700 °C. The evaluation over the entire time scale of the succession of heat pulses is a statistically reliable analysis. A software program is then used to calculate the thermal diffusivity of the batch. The computer records values each second. Thus, for every range, an average value of the thermal diffusivity based on at least 3 measurements is obtained.

Before measuring the real glass batches, an accuracy of the system was firstly checked by silica sand. The tests were performed at different frequencies and interval times and found an optimum signals output at a frequency of 50 Hz and time interval of 150 sec. Further investigated focused on three different grain sizes of sand from Quarzwerke Frechen and some typical glass batches. For sand, the results show that at finer grain size distribution the thermal diffusivity is lower and has a correlation of thermal diffusivity value with temperature. For some typical glass batches, four glass types of soda lime silicate, green, white, and crystal glasses were investigated

and compared with calculated results. From this state of the measurement, the measuring results may be trusted. Vice versa, we may learn from this comparison that the grain to grain contact in the model should be taken into account by a dimensionless shape factor by [69] of 2.5 to 3.5 for glass batches (1.25 denotes hard spheres with point contact).

### 5.3 Heating microscope

Conventional evaluations of the results obtained from heating microscope are the observation of three characteristic temperatures referring to: the start of visible gas release (bubbling) (T1), round edge point (T2), and complete melting point (T3). Two groups of the tests, i.e., commercial glass batches and soda lime silicate glasses with small additions were investigated. In the first group, four commercial glass types; (74-10-16, container green, container flint 1, and crystal glasses) were investigated by heating microscope. The results of T1, T2, and T3 clearly depended on type of the batches. The start of visible gas release was found at 870 °C for soda lime type, at 857 °C for green, and at 791 °C for white, and at 715 °C for crystal glasses. The lowest temperature of the round edge point was observed at 731 °C for crystal glass, which contains lower liquidus raw materials such as KNO<sub>3</sub>, and borax. The complete melting point was observed at 1063 °C for silicate, at 1029 °C for green, at 1080 °C for white, and 921 °C for crystal glasses. In a second group, additions of NaCl, NaNO<sub>3</sub>, and NaOH (1 wt. %) in soda lime silicate batches were investigated by heating microscope. Two significant temperatures of T1 and T2 were observed. Additional NaCl shows the strongest effect to lower the sintering temperature of the batch.

A new way to investigate the effect of gas release from glass batches was used, which is calculated from the equation

$$\text{progress of gas release} = \frac{\Delta m_1 (\text{gas, real})}{\Delta m_2 (\text{gas, total})} \times 100 ,$$

where  $\Delta m_1$  (gas, real) is the weight loss of gas determined from heating microscope (manually weight before and after tested), and  $\Delta m_2$  (gas, total) is

the theoretical weight loss determined from batch calculation. By using this method, soda lime silicate glass with a small additions (1 wt. %) of NaCl, NaNO<sub>3</sub>, and NaOH was investigated. Batch without any additions shows large sand grains compared to the batches with NaCl, NaOH, or NaNO<sub>3</sub>. The best effect was again reached with 1 wt. % NaNO<sub>3</sub>. It has the highest gas release, while NaOH shows the lowest one. The highest retention of bubbles was found in the batch containing 1 wt. % NaOH and the lowest remaining of bubbles was detected in the batch containing 1 wt. % NaNO<sub>3</sub>.

Another experimental design was used to investigate grain-to-grain contact reactions in both air and CO<sub>2</sub>. The following raw materials combinations were used: soda-lime, soda-dolomite, soda-phonolite, and soda-cullet (container flint 2, container green, and amber). They were investigated in air and CO<sub>2</sub> atmospheres at a flow rate of 10 l/h and a heating rate of 10 K/min.

A combination denotes two individual grains being put into physical contact and observed in the heating microscope. As can be seen from figures 61 and 62, soda ash started to visibly react with silica sand at 866 °C, combined into one grain at 868 °C, formed a new phase at 954 °C and reached a complete melt at 1085 °C. Soda and lime started to react at 797 °C, formed a single array at 822 °C (soda and limestone attract each other), and completely melted at 827 °C. The reaction between soda ash and dolomite started at 867 °C. Dolomite repels soda as not to form a physical contact. Dolomite (after its decomposition) sucks the soda ash to it side to form a new phase. Melting is not completed even at 1300 °C. Phonolite pulls the soda ash to form a liquid phase; it started to reacts at 869 °C and reached the final state (no longer spreading) at 1173 °C. Likewise, the cullet tended to pull the soda ash as soon as it melts. Their physical contacts began at 866 °C and reached a final stage at around 930-960 °C. Figure 63 illustrates the reaction between Na<sub>2</sub>O and Na<sub>2</sub>CO<sub>3</sub>. They show a completely melted of soda ash at 859 °C, while pure Na<sub>2</sub>O melt at 1130 °C. From these investigations, it could be concluded that the reaction between two components of soda ash and limestone would occurred at the lowest temperature and followed by soda-phonolite, soda-cullet, and soda- dolomite. Anyways, all reaction systems

began in between 800-870 °C due to the liquid film from soda ash occurred around 870 °C, in CO<sub>2</sub> atmosphere.

## 5.4 Batch free time (BFT)

Two different types of furnace; one from GHI and another one from Schott Glass GmbH were used. In evaluating the batch free time experiments, the crucibles were firstly loaded with 150 g of cullet and heated to  $1400 \pm 10$  °C. Then, 86 g of batch was quickly charged on top of the established cullet melt in the crucible. Five different batches of crystal, container flint 1, and sodium silicate glasses at Si:Na = 2.05, 3.3, and 3.4 were used to perform the testes at GHI furnace. Different tests were performed with different interval times depending on glass types. The melting of the batch was recorded by a video camera. After tested, the samples were vertically cut and visually evaluated. The residual crystalline phases were inspected by light microscope from the sample of 1.5 mm thick. For the tests at Schott Co. with silica tube furnace, only 74-10-16 glass batch was performed. The cullet were firstly heated up slowly at 10 K/min to 1500 °C for 30 min in silica tube. After that glass batch was charged on top of the melt and an on-line VDO recorder was record the batch melting reaction.

The use of a high pass filter for short wavelengths between 250-400 nm combined with a 70 W halogen lamp was mandatory for a successful observation. From the tests, time at which all solid islands disappeared was found to be: 132 s for crystal glass, 309 s for container flint 1 glass, and 223, 267, and 244 s for sodium silicate glasses at Si:Na ratios of 2.05, 3.3, and 3.4 respectively. It was also found that the reaction behavior of container flint 1 was rather slower than crystal glass. The reactions began within a few seconds after the glass batch was charged on top of the molten cullet melt and the reactions started from the edge to the middle of the crucible. However, this is still not enough to determine whether > 99 % of batch had disappeared under the glass melt.

An observation from the light microscope images of batch sodium silicate glass at Si:Na ratio of 3.3 indicated a bulky of remaining crystalline

phases still remains at the melted surface after 10 min. Many bubbles and seeds were observed both in a rough melted batch layer and in the lower part of the melt. After 20 min, less crystalline grains, bubbles, and seeds were remained, and not disappear even after 50 min. After 80 min, all remaining grains were dissolved into glass melt, but some tiny bubble still remained.

Visually observed of molten glasses in crucibles show different colors, which depending on their characteristic compositions. A white color at the surface of rough molten glass batch was clearly seen, which indicated a residual crystalline phases with rigid foam reactions. They show a degree from low to high of crystal, container flint 1, and sodium silicate glasses, respectively. High residual crystalline phases were found to locate at the edge of the crucible. A rough melted batch layer was also measured. Thinner layer of crystal and container flint 1 glasses than sodium silicate glasses was observed.

At Schott Glass GmbH, the melting reaction of 74-10-16 glass batch was observed through the silica tube furnace. It is clearly seen that after charging the batch blanket onto cullet melt, the reaction starts at the contact zone and progresses deeply into the batch blanket. The batch sank under the clear zone of the cullet level; foaming began. Some large bubbles were formed and trapped under the melt. After 2 min, most of raw materials were lifted up by foam that formed during melt. It took around 4 min to dissolve all raw materials (black spots). At this state, the diameter of foam bubbles decreased. The height of the foam forming was around 150 % higher than the thickness of the original batch blanket. After 10 min, the foam level decreased dramatically and remained constant after 25 min. At this state, small bubbles were still released from the bottom of the melt to the top. After 54 min, the sample was taken from the furnace and visually inspected. No batch residues were found.

## 5.5 Mass loss

The mass loss of materials is conventionally measured by thermogravimetric analysis (TGA), however, within the limit of typically only 250 mg. This amount of sample has very little chance of being representative

for the batches, all the more as the samples must be mixtures of finely ground powders. Therefore the new concept of weight loss determination by a tube furnace integrated with on-line mass loss signal detection from a balance ( $\pm 0.001$  mg) was constructed. By this method, it was possible to measure batches up to 200 g.

The system was calibrated by measuring the mass loss of limestone and dolomite. An accuracy of total mass loss in  $\pm 4$  % could be measured. Limestone showed a mass loss of 42.5 wt. % compared to a theoretical loss of 43.97 wt. %, while commercial grade dolomite showed a mass loss of 45.8 wt. % compared to theoretical loss of 47.73 wt. %. A comparison with conventional TGA measurement indicates that the tube furnace gives a more realistic account of the decomposition rate of a commercial grade material: the decomposition starts earlier and terminates later than in the TGA experiment. Beyond this, the mass loss in the tube furnace is a little bit higher, probably due to a certain amount of particulate loss. After calibration, mass loss of soda sand (S1) and container flint 1 (S3) batches at a batch size of 50 g were measured. Mass loss detected from TGA of both tests began faster and completed earlier than mass loss from vertical tube furnace, however, at a similar amount of total weight loss. The newly designed measuring system suitable for batches up to 200 g gives the possibility to measure mass loss of industrial grade batches in a way superior to conventional TGA.

## 5.6 Summary

To summarize, five unconventional methods suitable for the characterization of industrial grade glass batches was successfully developed and tested against several number of different batches, and sub-systems of batches. They were 1) conductometry, 2) thermal diffusivity, 3) heating microscope, 4) batch free time (BFT), and 5) mass loss. Each of the development was carefully calibrated with a known characteristic values. These new characterization methods not only open up a useful interpretation concepts for batch heap reactions, but also lower the window between conventional lab scale characterization results and the results occurs in actual industrial production.



## Chapter 6

### References

- [1] Sheckler, C.A.; Dinger, D.R.: *Effect of particle size distribution on the melting of soda-lime-silica glass*. J. Am. Ceram. Soc. 73 (1990) no. 1, p.24-30.
- [2] Tomasson, C.V; Wilburn, F.W.: *The application of differential thermal analysis and thermogravimetric analysis to the study of reactions between glass-making materials. Part II. The sodium carbonate-silica systems with minor batch additions*. Phys. Chem. Glasses, 1 (1960), no. 2. , p. 52-69.
- [3] Kroeger, C.: *Gemengereaktionen und Glasschmelze*. Glastechn. Ber. 25 (1952) no. 10, p. 307-324. Considered part I of [5].
- [4] Kroeger, C. et al.: *Ueber die Geschwindigkeit der zur Glasschmelze fuerenden Reaktionen*. Glastechn. Ber. 26 (1953) no.11, p.346-353.
- (i) Kroeger, C. et al.: *Die Umsetzung von Natriumdisilikat mit Soda und von Quarz mit Kalkstein*. Glastechn. Ber. 27 (1954) no.6, p.199-212.
- (ii) Kroeger, C. et al.: *Reaktionsgeschwindigkeiten im quaternaeren System  $\text{Na}_2\text{O}-\text{CaO}-\text{SiO}_2-\text{CO}_2$* . Glastechn. Ber. 28 (1955) no.2, p.51-57.
- (iii) Kroeger, C. et al.: *Die Druckabhaengigkeit der Umsetzungsgeschwindigkeiten im quaternaeren System  $\text{Na}_2\text{O}-\text{CaO}-\text{SiO}_2-\text{CO}_2$* . Glastechn. Ber. 28 (1955) no.3, p.89-98.
- (iv) Kroeger, C. et al.: *Die Umsetzung von Natriumdisilikat und Disilikat Quarz-Gemischen*. Glastechn. Ber. 29 (1956) no.7, p.275-289.

- (v) Kroeger, C. et al.: *Der Einfluss von Zusaetzen auf die Reaktionsgeschwindigkeit eines Soda-Kalkstein-Quarz-Grund-gemenges*. Glastechn. Ber. 30 (1957) no.6, p.222-229.
- (vi) Kroeger, C. et al.: *Die Abhaengigkeit der Einschmelzzeit des Glas gemenges von Art und Menge der durch die Gemengereaktionen gebildeten Produkte*. Glastechn. Ber. 34 (1961) no. 8, p.408-412.
- [5] Kroeger, C.: *Ueber die Geschwindigkeit, den Mechanismus und die Phasenneubildung bei den unter Schmelzbildung ablaufenden Festkoerperreaktionen*. Glastechn. Ber. 30 (1957) no. 2, p. 42-52.
- [6] Speyer, R. F. and Hong K. S.: *Thermal analysis of reactions in soda-lime silicate glass batches containing melting accelerants. I. one- and two-component system*. J. Am. Ceram. Soc. 76 (1993), no. 3, p. 598-604.
- [7] Speyer, R. F., Lee, S. W. and Hong K. S.: *Thermal analysis of reaction in soda- lime silicate glass batches containing melting accelerants. II. Multicomponent systems*. J. Am. Ceram. Soc. 76 (1993), no. 3, p. 605-608.
- [8] Speyer, R. F. and Savard, M. E.: *Effects of particles size on the fusion of soda-lime silicate glass containing NaCl*. J. Am. Ceram. Soc. 76 (1993), no. 3, p. 671-677.
- [9] Speyer, R. F.: *Thermal analysis of materials*. School of Materials Science and Engineering, Georgia Institute of Technology, Atlanta, Georgia, 1994, p. 125-140.
- [10] Buss, W.: *Erhitzungsmikroskopischen Untesuchung von Vorgaengen in Glasschemlzen mit und ohne Sulfat*. Glastechn. Ber. 35 (1962) no. 4 p. 167-176.
- [11] Wilburn, E. W.; Metcalf, S. A. and Warburton, R. S.: *Differential thermal analysis, and high temperature microscopy of reactions between major components of a sheet glass batch*. Glass Technol. 6 (1965) 4, p.407-411.
- [12] Riedel, L.: *Wetting of limestone, quartz, and melting soda ash. A phenomenological study*. Glastechn. Ber. 35(1962) no. 1, p. 53-56.

- [13] Conroy, A.R. et al.: *Controlled atmosphere Hot-stage*. Glass Ind., 44(1963) no. 3, p. 139-143 and 175-177.
- [14] Manring, W. H. and Bauer, W. C.: *Influence of batch preparation process on the melting and fining of glass*. Glass Ind., 45(1964) no.6, p. 354-357.
- [15] Abou-El-Azm, A. et al.: *A study on the reaction rates between silica and other oxides at varied temperatures*.
- I. Reaction rates in binary mixtures.
  - II. Reaction rates in ternary mixtures. Reaction rates in binary and ternary mixtures additional to those described in parts I and II.
  - III. Influence of the form in which the non-silica constituents are introduced upon their rates of reaction with silica.
  - IV. Theory of reactions rates in binary and ternary mixtures. J. Soc. Glass Technol. 37 (1953), p.129-154; p.155-164; p.168-169; p. 182-189; p. 190-212.
- [16] de Kever, K. and Frischat, G.H.: *Influence of batch moisture and atmosphere on the melting behavior of  $As_2O_3$ - and  $Sb_2O_3$ - containing glasses*. Glastech. Ber. 65 (1992) no.2, p. 64-66.
- [17] Joydeb, M.; Asis, K. N. and Kapil, D. S.: *Reactions in container glass batch*. Am. Ceram. Bull. 59 (1980), o. 8, p. 790-793.
- [18] Hrma, P.: *Reaction between sodium carbonate and silica sand at  $874^\circ C < T < 1022^\circ C$* . J. Am. Ceram. Soc. 68 (1985), no.6, p. 337-341.
- [19] Hrma, P.: *Batch melting reactions*. In: Paul, A.: *Chemistry of Glasses*. Chapman and Hall, London, 1990, p. 157-177.
- [20] Conradt, R., Suwannathada, P., and Pimkhaokham, P.: *Local temperature distribution and primary melt formation in a melting batch heap*. Glastech. Ber. Glass Sci. Technol. 67 (1994) , no. 5, p.103-113.
- [21] Buntig, J. A. and Bieler, B. H.: *Batch-free time versus crucible volume in glass melting*. Am. Ceram. Soc. Bull. 48 (1969) no. 8, p. 781-785.
- [22] Buntig, J. A. and Bieler, B. H.: *Batch-free time versus crucible volume and soda type in glass melting*. Am. Ceram. Soc. Bull. 63 (1984) no. 11, p. 1405- 1407.

- [23] Bieler, B. H.: Melting *characteristics of four types of soda lime glass batch*. Am. Ceram. Soc. Bull. 64 (1985) no.11, p. 1481-1484.
- [24] Lyle, A. K.: *Method for measuring fining time of glass*. J. Am. Cem. Soc. 28 (1945), no.10, p. 282-287.
- [25] Bauer, W.C.; Manring, W.H.: *Influence of Batch preparation process on the melting and fining of glass*. The glass industry. July (1964). p. 354-357.
- [26] Bieler, H.B.: *A Furnace for Photography of Melting Glass Batch*. Am. Ceram. Soc. Bull., 64 (1985) no. 11. p.1476-1478.
- [27] Hrma, P.; Kim, D.K.: *Volume Changes During Batch to Glass Conversion*. Am. Ceram. Soc. Bull. 69 (1985) no.6. p. 1039-1043.
- [28] Cable, M.; Bhuiyan.M.M.: *The refining of two soda-lime-silica glasses with sodium sulphate*. Glass Technology. 6 (1965) no.6. p. 206-212.
- [29] Cable, M.; Bower, C.: *The homogeneity of small-scale laboratory glass melts*. Glass Technology. 6 (1965) no.6. p. 197-204.
- [30] Cable, M.: *Kinetics and Mechanisms of Fining Glasses*. J. Am. Cem. Soc. 49 (1966), no.8, p. 436-441.
- [31] Cable, M.; Clarke, A.R.; Haroon, M.A.: *The influence of size of melt on the refining of a glass*. Glass Technology. 9 (1968) no. 4. p.101-104.
- [32] Cable, M.; Siddiqui, M.Q.: *The replacement of soda ash by caustic soda in laboratory glass melting trails*. Glass Technology. 21 (1980) no. 4. p.193-198.
- [33] Hrma, P.: *Thermodynamics of batch melting*. Glastech. Ber. 55 (1982) no.7, p. 138-150.
- [34] Fuhrmann, H.: *Contribution to the approximate calculation of glass batch melting. I. Theoretical derivation. II. Numeric results*. Glastech. Ber. 46 (1973) no. 10, p. 201- 208; no. 11, p. 209-218.
- [35] Mase, H. and Oda, K.: *Mathematical model of glass tank furnace with batch melting process*. J. Non-Cryst. Solids 38&39 (1980), p. 807-812.
- [36] Hilbig, G. and Kirmsse, H.: *The temperature distribution in the batch wedge in fuel fired glass tanks*. Glastech. Ber. 59 (1986) no. 6, p. 169-173.

- [37] Urgan, A. and Viskanta, R.: *Melting of continuously charge loose batch blankets in glass melting furnaces*. Glastech. Ber. 63 (1986) no. 10, p. 279-291.
- [38] Hrma, P.: *Melting of foaming batches: Nuclear waste glass*. Glastech. Ber. 63K (1990) p. 360-369.
- [39] Phase equilibria diagrams; CD-ROM database, the American Ceramic Society, Westerville, Ohio, (1998).
- [40] Conradt, R.: *Analysis methods and solution strategies for energy utilization problems in glass industry*. In: Proceedings of the 5<sup>th</sup> ASEAN Conference on Energy Technology. Vol. 1, Bangkok, 1994, p. 93-100.
- [41] Conradt, R.: *Melting behavior of batches containing ground cullets*. Fundamentals of Glass Science and Technology, p. 290-296. Växjö, Sweden, 1997.
- [42] Conradt, R.: *On thermodynamics of glass melt and solid glass*. Thesis. Aachen 1996.
- [43] Conradt, R.; Pimkhaokham, P.: An easy-to-apply method to estimate the heat demand for melting technical silicate glasses. Glastech. Ber. 63K (1990), p.134-143.
- [44] Madivate, C.; Müller, F.; Wilsmann, W.: Thermochemistry of the glass melting process – energy requirement in melting soda-lime-silica glasses from cullet-containing batches. Glastech. Ber. Glass Sci. Technol. 69 (1996), 167-178.
- [45] Phase diagrams for ceramists.
- Vol. I.: Oxides and salts.  
Levin, E.M.; Robin, C.R.; McMurdie, H.F.; eds.
- Vol. II.: Oxides and salts.  
Levin, E.M.; Robin, C.R.; McMurdie, H.F.; eds.
- Vol. III.: Oxides and salts.  
Levin, E.M.; McMurdie, H.F.; eds.
- Vol. IV.: Oxides.  
Roth, R.S.; Negas, T.; Cook, L.P.; eds.

- Vol. V.: salts.  
Roth, R.S.; Negas, T.; Cook, L.P.; eds.
- Vol. VI.: Oxides.  
Roth, R.S.; Dannis, J.R.; McMurdie, H.F.; eds.
- Vol. VII.: salts.  
Cook, L.P.; McMurdie, H.F.; eds.
- [46] Lakatos, T.: *Viscosity-temperature relations in glass composed of SiO<sub>2</sub>-Al<sub>2</sub>O<sub>3</sub>-Na<sub>2</sub>O-K<sub>2</sub>O-Li<sub>2</sub>O-CaO-MgO-BaO-ZnO-PbO-B<sub>2</sub>O<sub>3</sub>*. *Glastek. Tidskrift* **31** (1976) no. 3, p. 51-56.
- [47] Janz, G.J.: *Molten salts handbook*. Academic Press, London, 1967.
- [48] Janz, G.J.; Dampier, F.W.; Lakshminarayanan, G.R.; Lorenz, P.K. and Tompkins, R.P.T.: *Molten salts: Volume 1. Electrical conductance, density, and viscosity data*. NSRDS-NBS 15, Washington D.C., 1968.
- [49] Young, D.A.: *Decomposition of solids*. In: *The international encyclopedia of physical chemistry and chemical physics. Topic 21. Solid and surface kinetics*. Guggenheim, E.A., Mayer, J.E., Tompkins, F.C., eds. Pergamon Press, Oxford 1966.
- [50] Babushkin, V. I.; Matveyev, G. M. and Mchedlov-Petrosyan, O. P.: *Thermodynamics of silicates*. Springer Verlag, Berlin 1985.
- [51] Kubaschewski, O.; Alcock, C. B and Spencer, P. J.: *Materials Thermochemistry*. Pergamon Press, Oxford 1993.
- [52] Kirk-Othmer: *Encyclopedia of chemical technology, Vol. 20*. Mark, H.F., Othmer, D.F., Overberger, C.G., Seaborg, G.T., eds. Wiley, New York 1982.
- [53] Forland, I T.: *An investigation of the activity of calcium carbonate in mixtures of fused salts*. *J. Phys. Chem.* **59** (1955), p. 152-156.
- [54] Kroeger, C.: *Die Oxidbildungswaermen der ternaeren Natron-Kalk-Silikate*. *Glastech. Ber.* **26** (1953), no. 6, p. 171-174.
- [55] R. Conradt: *Dolomit für die Glasschmelze – Verhalten und Alternativen*. Proc. 78. DGG Conf., Nürnberg 2004, 233-238.
- [56] R. Conradt: *Thermodynamics of glass melts and thermo-chemistry of glass forming batches*. *Glass Sci. Technol.* **77C** (2004), 74-84.

- [57] Trier W.: *Glasschmelzöfen. Chapter 6.4.* Springer-Verlag, Berlin 1984.
- [58] Kingery W. D., and Ulmann D. R.: *Introduction to ceramics.* John Wiley & Sons (SEA) Pte. 1991 p.234-238
- [59] Gistling, A. M. and Frandkina, T.P, J. Appl. Chem. USSR, 25 (1952) p.1325.
- [60] Krozoska, J.; Samkham, N., and Conradt, R. : *Bestimmung der lokalen Temperaturleitfähigkeit in aufschmelzendem Gemenge.* Proc. 73. Glastechnische Tagung, Halle (1999) p. 214-217.
- [61] DIN 51730,: *Bestimmung des Asche-Schmelzverhaltens.* Deutsche Norm April 1998.
- [62] Koepsel, D. and Seuwen, R.: *Methoden zur Messung der Blasenveränderung in Glasschmelzen.* Proc. 77. Glastechnische Tagung, Leipzig (2003) p. 23-28.
- [63] Pimkhaokham, P., Eiumnoh, C., Samkham, N., and Conradt, R.: *Study on the local and temporal distribution of temperature, oxygen activity, and liquid phase formation in a melting glass batch blanket.* Rep. Asahi Glass Found., 1995, 743-747.
- [64] Becker, E.: *Korrelation von Wärme- und Temperaturleitfähigkeit in heißen Schüttungen,* Bachelor thesis, RWTH Aachen, Institut fuer Gesteinshuettenkunde, Germany, 2004.
- [65] Samkham, N.: *Thermodynamics and kinetics of glass batch melting.* Chulalongkorn University, report. 1995.
- [66] Suwannathada, P.: *Study on the processes controlling the rate of batch melting.* Thesis, Chulalongkorn Univesity, Bangkok, 1993.
- [67] Eiumnoh, C.: *Investigation of the melting of glass batch blankets.* Thesis, Chulalongkorn Univesity, Bangkok, 1995.
- [68] Samkham, N.; Riesner, G.; Laaouina, A.; Kalda, M.; Conradt, R.: *The influence of sand quality kinetics.* Poster presentation, ESG international conference, Edingburg (2001).
- [69] Zehner, P. and Schluender, U.: *Waemeleitfaehigkeit von Schuettungen bei maessigen Temperaturen.* Chemie-Ing.-Techn. 42 (1970) p. 933-941.

- [70] Dubios, O.; Conradt, R.: *Experimental study on the effect of cullet and batch water content on the melting behavior of flint and amber container glass batches*. Glass Sci. Technol. 77 (2004), p.137-148.



# LEBENS LAUF

## PERSÖNLICHE ANGABE

---

Name	Nang Sam Kham
Geburtsdatum	31.08.65
Geburtsort	Taunggyi, Shanstate, Myanmar
Familie	Pisit Geasee und Pakkamon Geasee
Eltern	Sai Kenneth Hsam und Nang Ngwe Pwint

## AUSBILDUNG

---

Seit 11/98	Anfertigung einer Dissertation an der Rheinisch-Westfaellischen Technischen Hochschule Aachen
7.11.1995	Abschluss des Hochschulstudiums (TH-Chulalongkorn) mit dem Titel Master Degree of Science (M.Sc.: Ceramic Technology), Gesamtnote 3.68 (4 ist das Maximum.)  Master Thesis bei Prof. Dr. Reinhard Conradt, Thema: Thermodynamics and kinetics of glass batch melting
Jan. 1988	Abschluss des Hochschulstudiums, (TH-Rangoon) mit dem Titel Bachelor Degree of Science (B.Sc.)
1978-1984	Abschluss des Studiums am Mayangone No.4 High School, Yangon, Myanmar (secondary)
1970-1978	Abschluss des Studiums am Taunggyi No.2 High School, Taunggyi, Shanstate, Myanmar (Primary and secondary)

## BERUFSERFAHRUNG

---

11/98-06/04	wissenschaftliche Mitarbeiterin am Institut für Gesteinshuettenkunde der RWTH Aachen, Deutschland
01/97-04/98	Exportgeschäft & technisches Support, Clays & Minerals (Thailand) Ltd., (Sibelco) Bangkok
04-12/96	wissenschaftliche Mitarbeiterin, Clays & Minerals (Thailand) Ltd.
09/90-12/95	wissenschaftliche Hilfskraft am Institut für Werkstofftechnik (Glas und Keramik), Technische Universität Chulalongkorn, Bangkok, Thailand
1987-1989	Finanzbuchhalterin, Ministerium für Kultur, kulturelles Institut, Yangon, Myanmar
1985-1987	Beamtin, Ministerium für Kultur, kulturelles Institut, Yangon, Myanmar
1984-1985	Bibliotheksverwaltung, Nationale Bibliothek, Yangon, Myanmar